MAX PLANCK INSTITUTE
OF QUANTUM OPTICS

Erbium dopants in silicon nanophotonic waveguides

Lorenz Weiß

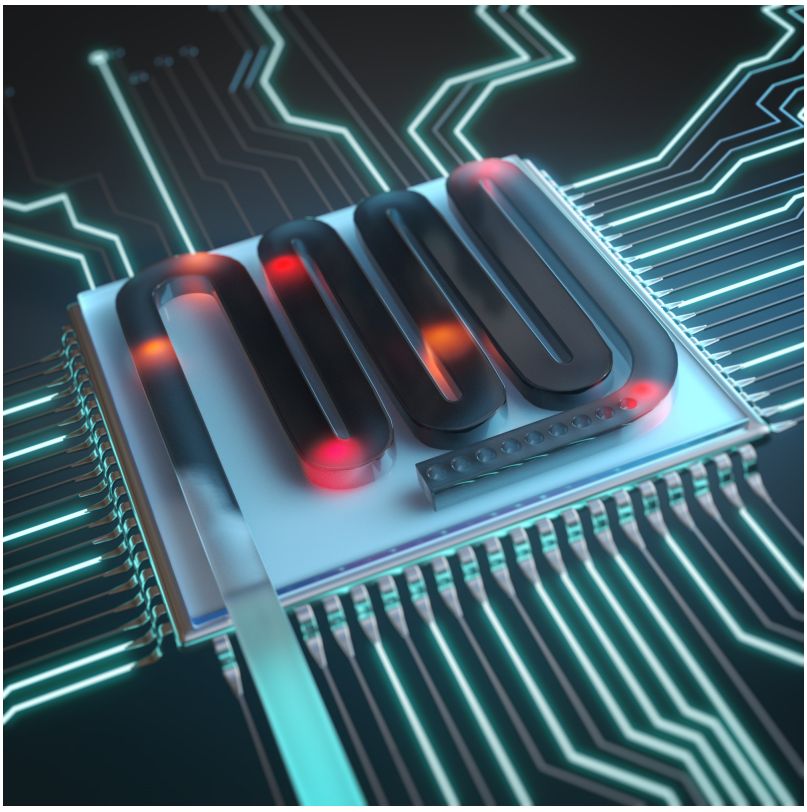

Dissertation

Physik-Department, Technische Universität München und
Max-Planck-Institut für Quantenoptik

Cover: Artist's view of a future quantum network node using an erbium-doped waveguide as a quantum memory.

Technische Universität München

Fakultät für Physik

Erbium dopants in silicon nanophotonic waveguides

Lorenz Karl Wilhelm Weiß

Vollständiger Abdruck der von der Fakultät für Physik der Technischen Universität München zur Erlangung des akademischen Grades eines

Doktors der Naturwissenschaften (Dr. rer. nat.)

genehmigten Dissertation.

Vorsitzender:	Prof. Dr. Michael Knap
Prüfer der Dissertation:	
	1. Hon.-Prof. Dr. Gerhard Rempe
	2. Prof. Dr. Menno Poot

Die Dissertation wurde am 13.06.2022 bei der Technischen Universität München eingereicht und durch die Fakultät für Physik am 19.07.2022 angenommen.

Abstract

The development of a quantum memory is of great importance for the operation of future quantum networks since they rely on storing entanglement in order to work over long distances. Erbium dopants are promising candidates for the implementation of such memories since they combine second-long ground state coherence with coherent optical transitions at telecommunication wavelengths. In this work, the unique optical properties of erbium are combined with the advanced platform of silicon photonics by embedding the ions into silicon nanophotonic waveguides. Several modifications of the erbium-doped silicon system and the measurement techniques were explored. In a first approach, silicon ridge waveguides were fabricated from erbium-doped, Czochralski-grown silicon-on-insulator wafers. Resonant spectroscopy reveals individual erbium-related narrow fluorescence lines with an inhomogeneous broadening on the order of a few gigahertz. In addition, via transient spectral holeburning, we extract a homogeneous linewidth on the order of few tens of megahertz. In the second generation of samples, pure CVD-grown silicon was implanted and used as substrate material for subsequent nanofabrication. The improved silicon quality and the optimized implantation procedure yield a small number of well-defined erbium sites with an inhomogeneous linewidth of a few hundred megahertz. Advances in the fabrication process and upgrades of the experimental setup resulted in an increased signal-to-noise ratio, enabling measurements of the crystal field splitting and further improving the homogeneous linewidth. Furthermore, the spin-lattice relaxation mechanism and Zeeman splitting were investigated and the achieved results were used for the demonstration of spin pumping and measurements of the spin lifetime. The third generation of samples used float-zone silicon-on-insulator as substrate material and a rib waveguide geometry. The high-purity silicon substrate and the post-implantation annealing process yield the same erbium sites as in the second generation of samples, establishing the presented fabrication processes as a feasible tool for the deterministic generation of erbium sites in different silicon platforms. Thus, the findings presented in this thesis contribute to paving the way for future Er:Si-based quantum memories.

Publications

- *Narrow optical transitions in erbium-implanted silicon waveguides*
  A. Gritsch*, L.Weiss*, J.Früh, S.Rinner, A.Reiserer
  arXiv:2108.05120 (preprint, 2021), submitted to Physical Review X

- *Erbium dopants in nanophotonic silicon waveguides*
  L.Weiss*, A. Gritsch*, B.Merkel, A.Reiserer
  Optica **8**, 40-41 (2021)

Contents

Chapter 1

Introduction

In light of recent progress towards the implementation of quantum computing [1, 2] many ideas for harnessing the unique properties of quantum mechanics in a broad range of possible applications have emerged. Of particular interest is the implementation of a quantum network [3, 4] which would enable new applications ranging from quantum cryptography [5] and modular quantum computation [6] to distributed quantum sensing [7, 8] to facilitate high-precision measurements [9]. A central research goal is the installation of a quantum network spanning distances of hundreds of kilometers e.g. over countries and continents. Analogous to classical network architecture the information is encoded in a light field and distributed via a photonic channel. Using photons as the information carrier is a natural choice due to their propagation at the highest speed possible, the speed of light. In pioneering experiments, the distribution of encoded information via free-space channels has been tested and pushed to its limits [10, 11, 12]. Ultimately, the transmission losses in free space strongly depend on a large number of factors like the local atmospheric environment, weather conditions, and the relative alignment of sender and receiver An alternative channel is optical glass fibers which are already used in today's internet technology. Pioneering experiments with NV^- centers in diamond [13] and single trapped atoms [14] have been done to demonstrated the entanglement between two network nodes connected via a glass fiber. These fibers have a minimum loss at a wavelength of around 1.55 µm, centered in the "telecom C-band" ranging from 1.53 µm-1.56 µm. This wavelength range belongs to one of the "telecom windows" corresponding to regions where typical fiber communication is operating. In the C-band, the propagation loss in glass fibers is around 0.2 dB/km which translates into a transmission efficiency of 1 % across a distance of 100 km [15]. It should be noted here that there has been great effort to reduce the absorption loss even further for several decades now but which until today has not led to the desired success [16]. In classical fiber-optic communications, this loss can easily be compensated by using amplifiers, which measure and resend the signal at regular intervals along the fiber link. This allows to distribute the signal further along the network nodes. Quantum networks are based on entanglement distribution. In general, simply amplifying, i.e. measuring and resending the entanglement signal is impossible due to the non-cloning theorem [17]. Photon loss during transmission prevents the distribution

of entanglement over arbitrary large distances. In addition, due to detector noise or decoherence, the purity of the distributed entanglement decreases exponentially with the length of the quantum channel [18]. A possible solution is a so-called quantum repeater, a device whose purpose is to increase the distance over which entanglement can be generated at practical rates [19]. A central component of many quantum repeater protocols is a quantum memory, which is needed to store the entanglement until all links in the network have been subject to an entanglement swapping protocol [20, 21]. Assume two separated, entangled pairs A,B and C,D where the systems within each pair are entangled as illustrated in Fig. 1.1. It is then possible to entangle subsystems A and D by performing a joint measurement of systems B and C in a basis of entangled states such that now systems A and D are entangled. While continuing entanglement swapping of all nodes the information of a successful swapping is stored in a quantum memory [22, 23]. The entanglement swapping is repeated until all the elementary links are entangled. The minimal required memory time of a quantum memory corresponds to the time needed to entangle systems A and Z as indicated by the timeline on the left-hand side in Fig. 1.1.

So far a number of quantum memory architectures have emerged and have already been experimentally realized in a number of systems, e.g. rubidium atoms [25], cesium atoms [26] and rare-earth-doped crystals [27, 28].

In this thesis, I investigate erbium-doped silicon (Er:Si) as a new platform for quantum memories that combines the unique optical properties of erbium and with the mature and highly developed silicon nanotechnology.

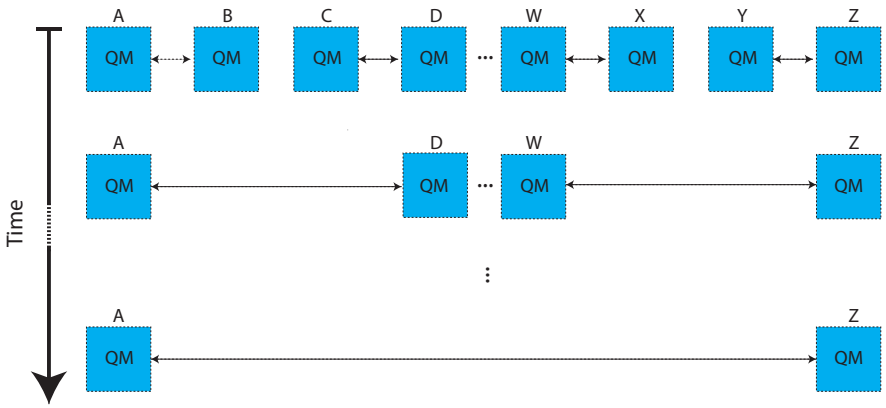

FIGURE 1.1: **Entanglement distribution scheme.** The blue boxes represent quantum memories and the arrows indicate entanglement. The systems A and B, C and D, etc. are entangled pairs which are subsequently subject to swapping operations which in the end leads to the entanglement of A and Z. The operation takes a certain amount of time which needs to be equal or smaller than the storage time of the used quantum memory. Figure modified from [24].

Er^{3+}:Si - A potential candidate for quantum memories?

Compared to other investigated systems for optical memory applications, erbium-embedded systems have several advantages.
Erbiums' coherent optical transition in the telecom C-band around 1536 nm is to date the only coherent emitter in the low-loss fiber transmission window [29]. So far many other potential candidates for quantum memories have been investigated, like nitrogen-vacancy centers in diamond (NV^-) [30], silicon-vacancy centers in diamond (SiV^-) [31] or quantum dots [32] which all suffer from high transmission losses in optical glass fiber. In Fig. 1.2 a) the absorption in standard, commercially available germanium-doped silica optical fibers is shown as a function of the wavelength. The

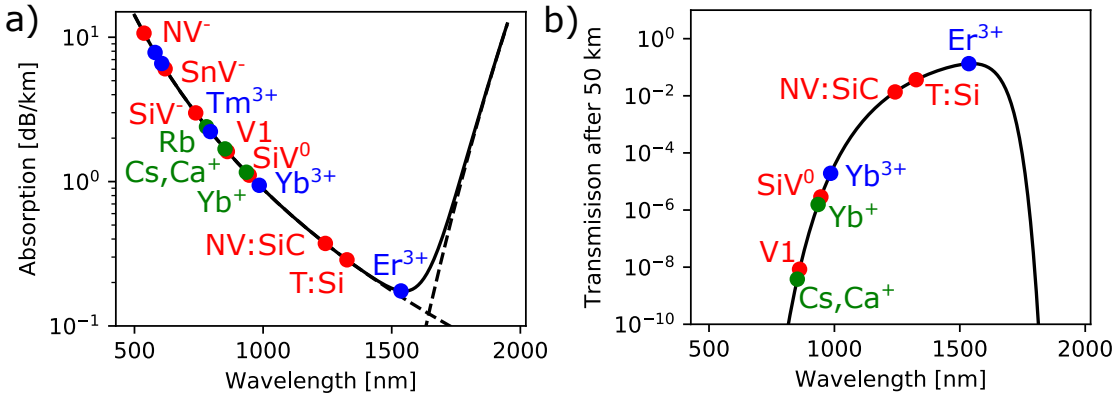

FIGURE 1.2: **Losses and transmission in optical glass fibers.** a) Absorption coefficient in optical glass fibers as a function of the wavelength indicated by the black solid line. The dashed lines correspond to Rayleigh-scattering and absorption-induced losses. Some prominent emitters with their transition wavelength are shown. b) Transmission after 50 km of optical glass fiber. Er^{3+} is the emitter with the highest transmission coefficient in optical fibers. Figure adapted from [33].

black solid line indicates the absorption in glass fiber. The overall loss is composed of the losses due to Rayleigh scattering and infrared absorption as indicated by the two black dashed lines. Additionally, several potential candidates for quantum memories are shown. The color coding corresponds to the most prominent classes of investigated systems to date: Defect centers in diamond, silicon carbide, and silicon are shown in red, single atoms in vacuum in green and rare-earth dopants in blue. The NV^- center, for example, emits light at 637 nm i.e., at a wavelength at which the loss in a glass fiber is about 10 dB/km [13]. So after 50 km of fiber length, the light is attenuated by a factor of 10^{-40}. For SiV^0 defects the transmission losses are smaller, around 1 dB/km [34] which translates into a transmission of 10^{-5} as indicated in Fig. 1.2 b) which is still too low for practical applications. Thus, solid-state systems as well as single atoms in vacuum platforms operating outside the before mentioned "telecom window" require frequency conversion in a large-scale quantum network.

This technique is used for converting visible light to telecom wavelengths and has already been demonstrated in different experiments [35, 36], however, the need for frequency conversion becomes obsolete when using an emitter at a suitable frequency avoiding loss due to finite conversion efficiencies and additional fiber links. The only currently known system with a transition within the "third telecom window" is erbium (Er). At this wavelength, the losses in standard glass fibers are about 0.2 dB/km and thus the transmission after 50 km is on the order of 10%, highlighting the potential of the Er^{3+}:Si platform.

In addition to the high transmission in optical fibers, the erbium emission frequency also allows for the use of low-loss silicon nanophotonic waveguides [37]. Silicon has a refractive index of approximately 3.5 at 1550 nm and is therefore highly suited for guiding near-infrared (NIR) light. This quality can be utilized in the silicon-on-insulator (SOI) technology where the silicon resides on an insulating layer (often SiO_2) which exhibits a lower refractive index and thus confines the light within the silicon due to total internal reflection.

The mature nanofabrication technology opens unique prospects for scalability of Er^{3+}:Si based devices. The typical length scale of an on-chip nanophotonic device is on the order of ten to hundred micrometers. A waveguide in our experiments occupies an area of roughly 500 μm^2. Thus, on a standard 8 inch wafer over 60 million nanophotonic devices can be fabricated. Using so many devices in parallel requires robust and scalable control techniques that can be integrated on the same chip [38]. Compared to technologies based on trapped single atoms in vacuum the technical overhead is trimmed down dramatically when using defects or dopants in solid-state hosts. As the latter devices can be integrated into one cryostat, one does not need precise, high-power lasers for the control since trapping is done by the crystal and cooling is done by a cryocooler. In my experiments I use cryocoolers reaching temperatures below 2 K which can in principle be housed in a 19-inch rack thus allowing for a very compact experiment design. This is also crucial for a cost-effective future quantum network both in terms of size and maintenance.

Another important figure of merit is the optical coherence as it will finally limit quantum memories' storage time. The memories' working principle is based on the mapping of the photons' quantum state onto the quantum transition of the material system and vice versa. For practical applications in a global scale quantum network, the coherence time must be long compared to the network transmission times. Coherence times ranging from less than a few milliseconds [39] up to several hours [40] in different rare-earth-doped crystals have been reported. For Er:YSO a second-long nuclear spin coherence time [41] and most recently a 23 ms electron spin coherence time in Er:$CaWO_4$ [42] have been reported.

Thesis outline

In this work, the optical properties of erbium-doped silicon waveguides are investigated. The thesis is organized as follows:
Chapter 2 gives an introduction to the physics of rare-earth ions with a focus on erbium. I will discuss the general properties of rare-earth dopants in solid-state hosts and summarize the current state of Er^{3+}:Si research in the literature. To that end, I will review the spectroscopic properties, measurement techniques, and discuss the experimental approach developed in this thesis.
Chapter 3 introduces the field of nanophotonics where I start by recapitulating Maxwell's equations in solids. I will explain the workflow for designing nanophotonic waveguides by performing several numerical simulations. These simulations allow one to choose a design for the devices and also enable later optimization of the light-matter interface. Two approaches to a fiber-to-chip interface will be introduced including simulations and the subsequent experimental realization. I conclude this chapter by outlining the fabrication procedure of the samples.
The experimental setup is presented in chapter 4. I discuss the laser system and will briefly review the experiment control. Finally, the heart of the experiment is described - the cryogenic setup. I will review the requirements and describe the challenges of performing measurements at low temperatures.
Chapter 5 introduces the spectroscopy experiments where I demonstrate that by implanting erbium into silicon and subsequent annealing I can generate a plethora of narrow individual Er-related fluorescence lines with inhomogeneous broadening on the order of a few GHz. I conduct a detailed analysis of the optical lifetime and introduce a novel technique for estimating the homogeneous linewidth. The chapter is concluded by investigating the magnetic field dependence of the found sites, drawing conclusions on the symmetry of dopants within the silicon matrix. The results presented in this chapter are published in [43].
In chapter 6 I report on the improvement of the quality of the Er:Si chips as well as some of the measurement techniques. As a starting material, I use CVD-grown silicon and perform isotope selective implantation at elevated temperatures. This yields a reduced number of well-defined sites with an inhomogeneous linewidth of a few hundred MHz which I attribute to pure Er-sites. By modifying the sample fabrication process, I am also able to minimize waveguide losses, increasing the signal-to-noise ratio by a factor of 100. Further improving the experimental setup allows to accurately determine the crystal field splitting of the found Er-complexes and enables the investigation of the waveguide geometry on the emission of the embedded dopants. To examine the homogeneous linewidth further I adapted the laser system such that I can probe large parts of the Er^{3+} ensemble using multiple light fields at the same time. This enables the extraction of a value for the homogeneous linewidth close to the lifetime limit. Finally, I investigate the Zeeman splitting and use the results obtained to demonstrate spin pumping and for measurements of the spin lifetime.

The results of this chapter are published in [44].
In chapter 7, I use high-purity float-zone silicon as host material combined with a rib waveguide geometry. This calls for a different fiber-to-chip interface which enables measurements in a transmission setup. In addition, a second technique for measuring the homogeneous linewidth is implemented yielding values that are in accordance with our method of choice in the previous chapters. Finally, I present information on how implantation dose, post-implantation annealing, and spectroscopic properties are related.
The conclusion and outlook are presented in chapter 8 where I highlight the main findings of this thesis and give an outlook for future experiments.

Chapter 2

Er^{3+} ions in solids

This chapter introduces the main theoretical aspects of the Er^{3+}:Si platform. It includes the basic electronic properties of erbium and how these are modified for Er^{3+} ions hosted in a solid-state matrix. I review the work so far done on Er^{3+}:Si and describe my approach to using this material platform for future quantum memories.

2.1 Rare-earth ions

Rare-earth elements belong to the lanthanoid series. These elements feature a set of unique electronic properties. When incorporated in a solid-state host these elements typically become triply-ionized ions such that their electronic configuration takes the form [Xe]$4f^N$. Erbium has the electronic configuration [Xe]$4f^{12}6s^2$ [45, 46]. It thus can be found in the Er^{3+} oxidation state which is formed by the loss of one $4f$ and both of the $6s$ electrons. In this state the fully occupied $5s$ and $5p$ orbitals shield the partially filled $4f$ shell leading a "Faraday cage" like shielding effect of the inner $4f$ level. The $4f$ electrons, therefore do not play an active role in chemical bonding leaving the optical transitions unperturbed from the environment [47]. The *4f–4f* intra-shell transitions are parity-forbidden in free space, but become weakly allowed when embedded in a dielectric material due to the crystal field. The resulting sharp optical transitions resemble the ones of single trapped atoms in vacuum. Also, rare-earth ions share similar long optical lifetimes ranging up to milliseconds for various erbium-doped crystals.

Fig. 2.1 shows the corresponding energy levels of erbium in silicon, Er^{3+}:Si . The energy levels of the free Er^{3+} ion are labeled according to their angular (J), spin (S) and orbital (L) quantum numbers using the Russel-Saunders coupling scheme. This nomenclature assigns each level a label according to $^{2S+1}L_J$ using the quantum numbers from above. Whereas S and J are specified with numbers (0, 1/2, 1,...), L is traditionally specified with letters *S, P, D, E, F, G, H, ...* respectively for $L = [0, 1, 2, 3, 4, 5, ...]$. For erbium in its trivalent form, Er^{3+} , the ground state is thus $^4I_{15/2}$.

This at first glance complex definition is needed due to the lifting of the degeneracy by Coulomb and Spin-orbit repulsion terms. In addition there is a *(2J+1)*-fold degeneracy associated with each $^{2S+1}L_J$.

When embedding the ions in a crystal the electronic levels of the free atom split under the influence of the electric field produced by the crystalline environment. But recalling from the section above, the lattice only interacts weakly with the $4f$ electrons which means the Stark effect induced by the host material is rather small compared to the free ions Coulomb interaction. This effect can be witnessed in experiments by comparing the emission wavelength in photoluminescence experiments of Er^{3+} in various hosts: All dopants emitting at near-infrared (NIR) wavelengths are centered around 1540 nm with only a small spread at liquid helium temperatures [48]. The lifting of the degeneracy imposed by the surrounding lattice also depends on the symmetry of the ion within the matrix. In ionic crystals like Y_2SiO_5 or YVO_4 the rare-earth ion is typically placed on a Yttrium lattice site resulting in a few low-symmetry sites. For silicon, this is not necessarily the case due to the large size mismatch between silicon and erbium and their bonding types [47]. The degree to which the $2J+1$ -fold degeneracy of a free-ion state is removed in the crystal depends only on the point symmetry of the ion site [49]. For a high-symmetry cubic site, one expects five levels each, whereas a lower symmetry gives rise to an eight-fold splitting [50]. Assuming a priori low symmetry sites, e.g. given the atomic size mismatch of host and dopant in Er^{3+}:Si , I expect a total number of $2 \cdot 15/2 + 1 = 16$ crystal field levels. I will refer to these levels as crystal field (CF) levels throughout this thesis.

The crystal field levels occur in pairs due to Kramers' theorem. It states that for systems with an odd number of electrons, such as erbium, the energy levels are at least doubly-degenerate [51]. The Er^{3+} ion can then be treated as an effective spin-1/2 system where the spin-1/2 degeneracy in the ground and optically excited state can be lifted in a small magnetic field. This is a valid approximation because the splitting between the different CF levels within the ground and excited-state manifold is on the order of a few THz and therefore much larger than thermal energy at cryogenic temperature (around 40 GHz at 2 K) or inhomogeneous broadening (few megahertz up to several gigahertz).
A general expression for the Zeeman Hamiltonian describing an effective spin 1/2 system is given in Eq. (2.1).

$$H_Z = \frac{\mu_B}{\hbar} \mathbf{B} \cdot g \cdot \mathbf{S} \tag{2.1}$$

where μ_B is the Bohr magneton, $\mathbf{B}$ the magnetic field, g the Landé factor and $\mathbf{S}$ the spin vector. For a single atom, g is a scalar value. However, in erbium-doped materials the crystal field levels are superposition states of different angular momentum $\mathbf{J}$. This anisotropy, i.e. the low symmetry of the crystal fields, must be taken into account by expressing g as a three-dimensional, symmetric tensor. It can be shown that an anisotropic g-tensor leads to an effective precession that is not aligned to the external magnetic field. So the g-factor depends on the magnetic field orientation in

this material system and is hence denoted g_{eff} in the following. By using spherical coordinates and decomposing the vectors in Eq. (2.1) into their components along the eigenaxes of the g-tensor, the Zeeman Hamiltonian H_Z can be diagonalized. The resulting Zeeman eigenstates are $|\uparrow\rangle$ and $|\downarrow\rangle$ with Zeeman eigenenergies $E_Z = \pm\frac{1}{2}\mu_B g_{\text{eff}} B$. Details on the derivation of the effective g-tensor and the diagonalization of H_z are i.e. discussed in [52].

Both ground and excited Zeeman eigenstates are denoted as $|\uparrow\rangle_g$, $|\downarrow\rangle_g$ and $|\uparrow\rangle_e$, $|\downarrow\rangle_e$, respectively. I refer to $|\uparrow\rangle_g \leftrightarrow |\uparrow\rangle_e$ and $|\downarrow\rangle_g \leftrightarrow |\downarrow\rangle_e$ as "spin-preserving" and $|\uparrow\rangle_g \leftrightarrow |\downarrow\rangle_e$ and $|\downarrow\rangle_g \leftrightarrow |\uparrow\rangle_e$ to "spin-flip" transition in this thesis. The energy splitting is directly proportional to the applied magnetic field, the Bohr magneton μ_B and g_{eff} the effective Landé-factor as described by the Zeeman eigenenergies E_Z above.

Detailed visualization of the above-described mechanism is given in Fig 2.1. The $4f^{11}$ energy level is split into multiple sub-levels due to the Coulomb interaction giving rise to the levels ${}^4I$, ${}^4F$,${}^4S$ and ${}^2H$. These levels are again split due to spin-orbit coupling and I restrict the discussion here to the ground state level ${}^4I$. Spin-orbit interaction splits the latter into four levels labeled by the total angular momentum quantum numbers, 15/2, 13/2, 11/2, and 9/2. Here, I focus on the ground state ${}^4I_{15/2}$ and the first optically excited state ${}^4I_{13/2}$. When incorporated into a crystal these levels are again split due to the CF of the host material allowing emission at a wavelength of around 1.5 µm. In the classical spectroscopy notation, this corresponds to a wavenumber of

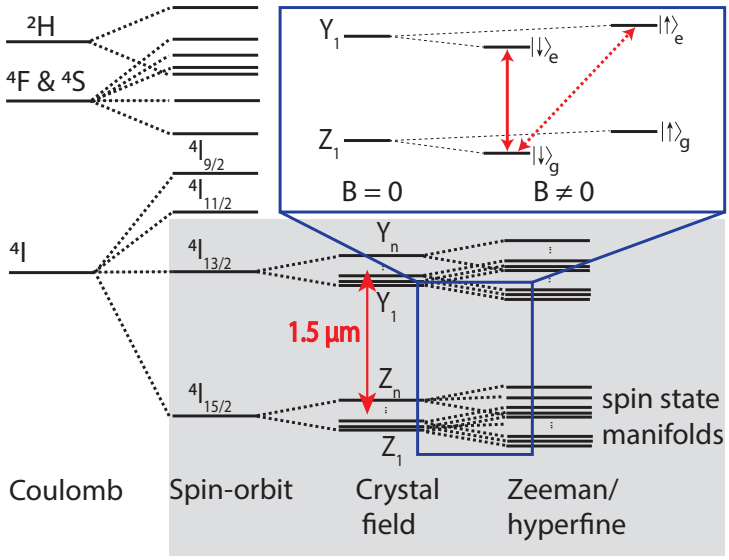

FIGURE 2.1: **Energy levels of Er^{3+} in a dielectric host material.** The level structure of Er^{3+} in a crystal is illustrated schematically. The grey box frames energy levels relevant in this thesis. Energy splitting is not to scale and the number of levels in the spin state manifold depends on the erbium isotope. The levels Z_i and Y_i correspond to the CF levels in the ground and excited state, respectively. In the blue box the effective spin 1/2 system is shown exemplarily for the $Z_1 \leftrightarrow Y_1$ transition. The red dashed and red solid line corresponds to a spin-flip and spin-preserving transition, respectively. The level separation is not to scale.

approximately 6500 cm^{-1}. The crystal field energy levels are two-fold degenerate and by applying a magnetic field, the degeneracy is lifted as illustrated in the blue box in Fig. 2.1. For erbium isotopes with a non-zero nuclear spin, i.e. ^{167}Er, an additional splitting of the levels is expected. The generated spin-state manifold then allows for spin-dependent optical transitions and the creation of a Λ-level scheme which is common in quantum memory architectures [47, 53]. It should be noted that also transitions from the ground state to the higher states e.g. $^4I_{11/2}$ or states in the ^4S manifold are accessible. However, they have larger energies and thus absorption bands at smaller wavelengths.

2.2 Spectroscopy of rare-earth dopants

The optical linewidths of rare-earth ions in solid-state materials vary over a wide range depending on the concentration, temperature, and local environment. Transition line shapes in pure crystals with low dopant concentration are typically governed by a Lorentzian-shaped, inhomogeneous distribution of transition frequencies. These frequencies together form the inhomogeneous linewidth Γ_{inh}. Here, and throughout this thesis, I use the full width at half maximum (FWHM) when describing spectral lineshapes. Within this inhomogeneously broadened ensemble each ion exhibits a homogeneous linewidth Γ_h (FHWM). At cryogenic temperatures, Γ_{inh} is typically on the order of a few hundred MHz up to several GHz depending on the type of ion, concentration and host material [54]. Homogeneous linewidths as low as 50 Hz have been experimentally measured [55, 56] which are close to the transform-limited linewidth of $\Gamma_h = 1/2\pi\tau$ where τ is the optical lifetime. At room temperature, the broadening mechanism drastically enlarging Γ_h is thermal broadening by phonons. This contribution is suppressed at low temperatures. Thus, the experiments presented in this thesis are all performed at liquid helium temperatures in a cryostat. In addition, coupling of the ions to fluctuating magnetic fields in the environment originating from impurities in the crystals or the crystals' constituents themselves can have an impact on the homogeneous linewidth. Also due to the typically large electric dipole moment of rare-earth ions, Γ_h is highly susceptible to ion-ion interaction, contributing to an additional line broadening. The homogeneous linewidth Γ_h is thus an important measure in characterizing rare-earth doped materials since it is correlated with its spin coherences which in turn are important in quantum memory applications. The bottom plot in Fig. 2.2 illustrates the relationship of Γ_h and Γ_{inh}. As the ensemble consists of many, slightly detuned resonances it is possible to excite a subset of ions using a narrowband laser as indicated in the upper plot of Fig. 2.2. Typically the FWHM of Γ_{inh} is on the order of GHz whereas a frequency-stabilized laser has a linewidth of a few kHz. By applying a narrowband light field some ions can be temporarily or permanently removed from the population and the inhomogeneous broadening is left with a spectral hole. The holes can be categorized into persistent holes existing much longer than the lifetime of the optically excited

state and transient holes which have lifetimes on the order of tens of milliseconds [57]. I will encounter both types of holes in this work and use them to measure Γ_h from which I extract the optical coherence time. The latter is important in quantum memory applications since this effectively limits the storage time.

The inhomogeneous broadening is a double-edged sword. On one hand a large Γ_{inh} allows for frequency multiplexing which is important for the performance of future quantum memories. On the other hand, the the optical depth decreases for increasing Γ_{inh}. Up to now the mentioned properties of Er^{3+} in crystals sound very promising concerning their suitability for quantum memories. A major drawback, however, is the low photon emission rate.

The reason is that the emission at 1.5 µm has a low dipole matrix element. For an erbium atom in vacuum the electric dipole transition between the intra-*4f* levels is prohibited by parity. This condition is weakened when erbium is incorporated into a solid. Due to crystal field coupling, mixing of the *4f* and opposite parity orbitals takes place, partially allowing a $4f \leftrightarrow 4f$ transition via a so-called forced electric dipole moment. This, however, still results in long optically excited state lifetimes on the order of ms and thus very low photon emission rates on the order of a few hundred Hz. Regarding possible applications in quantum communications such low photon emission rates of single ions are detrimental. The key goal is thus to improve this rate by increasing the interaction strength between the long-lived dopants and the

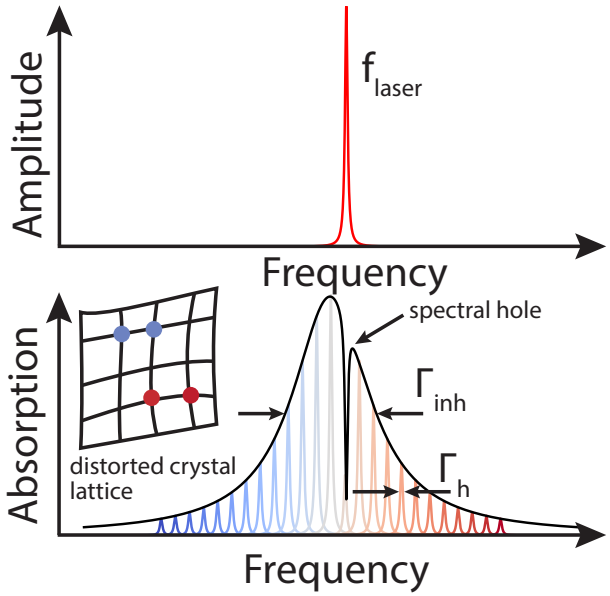

FIGURE 2.2: **Γ_{inh} and Γ_h in rare-earth doped crystals.** All ions in the ensemble exhibit an homogeneous linewidth Γ_h. Due to the crystalline environment the dopants (red and blue dots in inset) experience a inhomogeneous broadening Γ_{inh} due to locally varying electrical fields (black envelope). Applying a narrowband laser at a frequency f_{laser} (upper plot) excites a subset of the ions, removing them from the inhomogeneously broadened ensemble. The lifetimes of these spectral holes can vary from a few microseconds to days or even weeks. Figure modified from [57].

photons encoding the information which is then sent along the transmitting channel. Working towards increasing the photon emission rate, it is helpful recalling the size mismatch between an ion and a photon [14]. Assuming a faint, focused light beam with area A and an atom cross-section σ in a free-space geometry defined by:

$$A = \frac{\pi}{4}\omega_0^2 \text{ and } \sigma = \frac{3\lambda^2}{2\pi}$$

where ω_0 is the beam waist and λ is the optical wavelength. A deterministic atom-photon interaction requires $\sigma \gg A$, which is not possible in a free-space configuration even when using a diffraction-limited light beam [58]. A solution pursued by several groups in recent years is placing the solid-state embedded emitter in a cavity. This effectively increases the interaction cross-section by a factor proportional to the finesse of the resonator. There has been a number of different approaches so far where Er^{3+} ions have been placed in nanophotonic [59, 60, 61, 62], Fabry-Pérot [29] and fiber-based Fabry-Pérot resonators [63]. The use of nanophotonic cavities was also successfully employed for other rare-earth emitters in ionic hosts [64, 65]. Even though our group works towards the implementation of a Er^{3+}:Si based nanophotonic cavity this work uses a different approach, namely enhancing the absorption by using ensembles of Er^{3+} ions. The relevant figure of merit is the optical depth which is a measure of the number of ions within a certain length. Consequently, a large optical depth yields a large signal-to-noise ratio. Coping strategies so far involved the use of long crystals and high doping concentrations when working with ion ensembles.

2.3 Erbium in silicon

Silicon is the most used semiconductor material in modern information technology. It crystallizes in a face-centered cubic (fcc) lattice with a basis of two silicon atoms [66]. The atomic radius is 0.232 nm and the lattice parameter is 0.543 nm. The radius of an Er^{3+} ion is on the order of 0.272 nm yielding a size mismatch of around 15% [67]. This mismatch in addition to the differences in bonding types (ionic versus covalent) plays a major role in the symmetry of Er-related sites in Er^{3+}:Si . In general, the Er^{3+} ion can occupy a variety of positions within the silicon lattice, resulting to low symmetry complexes. The energy difference of the $^4I_{13/2} \leftrightarrow {}^4I_{15/2}$ transition is on the order of 0.9 eV such that the energy separation of the Er^{3+} ion levels is comparable to the silicon bandgap energy of 1.12 eV. Thus, partial overlapping of erbium energy levels with valence and conduction band is expected. There has been much work on the understanding of electronic excitation of various Er^{3+}-complexes in Er^{3+}:Si . However, all these mechanisms rely on above-bandgap excitation [47].
A major problem when incorporating erbium in crystalline silicon is its low solubility due to charge- and ionic-radius mismatch. The use of non-equilibrium techniques

like molecular beam epitaxy (MBE), chemical vapor deposition (CVD), and ion implantation can overcome this problem, at least partially. The first two techniques have been widely used in the past for the growing of thin films since these methods avoid damaging the crystal and are capable of growing sophisticated structures like superlattices or multilayer stacks [68, 69, 70]. However, still, the most common technique is ion implantation since it allows for an accurate dose control of the ions within the silicon and enables the shaping of the implantation profile. The use of ion implantation yields Er^{3+}:Si samples with shallow profiles depending on the used implantation energy. In this work, the erbium concentration is kept low, $\sim 10^{17} - 10^{18}$ cm^{-3}, to avoid unnecessary large inhomogeneous broadening [71]. Therefore, only a few erbium ions are present in the focal spot of an objective, for example in a confocal spectroscopy setup. In addition, the high refractive index of silicon leads to a small critical angle for total internal reflection, such that only a tiny fraction of erbium fluorescence can be collected in free space when using a vertical oriented, planar sample with randomly placed dipoles [33]. The major drawback of using ion implantation is the crystal damage induced by the high kinetic energy of the ions. This implantation damage can be repaired by post-implantation annealing at high temperatures ($\geq 500\,^{\circ}C$). However, the annealing conditions must be carefully engineered due to several reasons: Erbium tends to form precipitates when present in large concentrations, which leads to unwanted spectroscopic behavior like excessive inhomogeneous broadening and optical in-activity [72]. In addition, erbium does not only show the tendency of clustering with ions of the same kind but also with other impurities present in the host material, like oxygen or nitrogen. While previous work showed that for example, co-doping with oxygen enhances the luminescence of Er^{3+}:Si [73], my experimental finding indicate, that additional elements degrade the optical properties prohibiting the use in a quantum memory. These contaminating elements yield more sites as they can cluster together with erbium ions, each of which will emit at a different frequency, increasing the inhomogeneous broadening. Many of these elements or defects in silicon become mobile at elevated temperatures such that both the temperature [74], as well as the duration of the annealing process [75] must be chosen carefully. A detailed overview of defects in silicon and their annealing stages can be found in Refs. [76, 77]. Also, the annealing atmosphere is important with regard to surface contamination and passivation [73]. It is worth noting, that a large number of erbium-impurity defect centers in silicon have already been investigated [50], however, in most of the early work, the development of an Er^{3+}:Si based laser system was in the focus [78]. But till today reports on a net gain in Er^{3+}:Si remain controversial due to the large inhomogeneous broadening and small absorption cross-sections [37, 70]. As a rare-earth ion, erbium susceptible to coulombic dipole-dipole interactions which scale as $1/r^6$ where r is the ion-ion separation [47]. To isolate the intra-4f transition as well as possible from ions in close vicinity I keep the concentration of the erbium ions at a low level which stands out compared to previous work. Dealing with such few ions is a trade-off, since low concentration

gives low inhomogeneous broadening. This in turn yields low dipolar interactions which might allow for the use of single erbium ions. But on the other hand, for the initial spectroscopy experiments, a large ion concentration is beneficial as it yields an increased fluorescence signal. Previous work used off-resonant excitation, where the erbium dopants are coupled to the conduction band. This approach gives a sufficiently large fluorescence signal which can be collected from a thin layer using a microscope lens [79] or measured using electronic detection schemes [80]. Instead, my approach is targeting erbium ions that are decoupled from the conduction band as these dopants possess good coherence. For measuring these sites, I employ resonant spectroscopy techniques which are sensitive to these isolated dopants. However, this only yields a small fluorescence signal at the maximally possible ion concentration. Thus, I fabricated waveguides in the erbium-doped silicon to investigate the optical properties "in-plane", where I have created a setup that is comparable to typical resonant rare-earth ion spectroscopy that uses thick crystals.
Additionally, I find that the selection of the silicon host material is of great importance. The use of pure and almost defect-free silicon strongly improves the optical properties of the embedded Er^{3+} ions.

Chapter 3

Nanophotonic waveguides

In this chapter, I first review the theoretical basics of electromagnetism and discuss the main aspects of the numerical simulations employed. In addition to that, two different waveguide designs are presented and I derive a local density of states formalism describing the emission rates of the embedded Er^{3+} ions in these waveguides. Finally, the fabrication process of Er^{3+} doped silicon waveguides is briefly reviewed.

3.1 Maxwell's equations in solids

Maxwell's equations form the foundation of many physical disciplines like electrodynamics and (classical) optics. These equations completely describe the generation of electromagnetic fields by charges, currents, and changes in these fields and thus fully describe the propagation in nanophotonic structures as well. The following section follows the derivation given in [81]. In SI units and using bold symbols for vectors, Maxwell's equations are:

$$\begin{aligned} \nabla \cdot \mathbf{B} = 0 \qquad & \nabla \times \mathbf{E} + \frac{\partial \mathbf{B}}{\partial t} = 0 \\ \nabla \cdot \mathbf{D} = \rho \qquad & \nabla \times \mathbf{H} - \frac{\partial \mathbf{D}}{\partial t} = \mathbf{J} \end{aligned} \tag{3.1}$$

Here $\mathbf{E}$ and $\mathbf{H}$ denote the electric and magnetic fields, $\mathbf{D}$ and $\mathbf{B}$ are the displacement and magnetic induction fields. $\mathbf{J}$ is the current density and ρ the free charge density [82]. I will not derive the following equations here but give a short description of the assumptions and calculations to be made. The interested reader is referred to [81] for details. The fields $\mathbf{D}$ and $\mathbf{B}$ can be related to $\mathbf{E}$ and $\mathbf{H}$ using a power series expansion. There the higher-order terms can be neglected assuming macroscopic and isotropic materials, ignoring material dispersion, and restricting the analysis to transparent materials. With these assumptions the Maxwell equations (3.1) can be expressed in terms of $\mathbf{E}$ and $\mathbf{H}$. Solving them is done by applying a complex-values plane-wave-ansatz resulting in two equations relating $\mathbf{E}$ and $\mathbf{H}$. Solving this system

of equations yields the master equation:

$$\nabla \times \left(\frac{1}{\epsilon(\mathbf{r})} \nabla \times \mathbf{H}(\mathbf{r}) \right) = \left(\frac{\omega}{c} \right)^2 \mathbf{H}(\mathbf{r}) \tag{3.2}$$

Upon inspection of Eq. (3.2) it becomes clear that this is an eigenvalue problem. For a given $\epsilon(\mathbf{r})$, the modes $\mathbf{H}(\mathbf{r})$ and their corresponding (eigen-) frequencies need to be found, to solve the equation. After obtaining $\mathbf{H}(\mathbf{r})$ it is straightforward to recover the corresponding $\mathbf{E}(\mathbf{r})$ using Maxwell's equations.
In principle it is also possible to define the master equation in terms of the electric field $\mathbf{E}(\mathbf{r})$ and from then deduce the magnetic field. However in that case one runs into a set of mathematically subtleties which need to be taken care of. The main issue is to preserve the Hermitian operator in the master equation which is important since this ensures, among other things, that the eigenfrequencies (and thus the physical ones) are real and orthogonal [81]. By pursuing this alternate approach, one finds

$$\frac{1}{\epsilon(\mathbf{r})} \nabla \times \frac{1}{\mu(\mathbf{r})} \nabla \times \mathbf{E}(\mathbf{r}) = \left(\frac{\omega}{c} \right)^2 \mathbf{E}(\mathbf{r}) \tag{3.3}$$

where both operators are again Hermitian and positive semi-definite [83]. I will come back to Eq. (3.3) in chapter 3.3 when deriving an expression for the local density of states.

3.2 Tools for numerical simulations

The exact solutions of Maxwell's equations in combination with the knowledge of $\epsilon(\mathbf{r})$ enable quantitative numerical simulations. There is a wide variety of algorithms and techniques for solving partial differential equations, however, I will restrict myself here to reviewing two main categories of simulation types: Frequency-domain eigenproblems and finite-difference time-domain simulations.
First I discuss the **frequency-domain eigenproblem**. The task is to solve the Maxwell eigenproblem for the eigenvalues $\omega_{\mathbf{k}}$, where $\mathbf{k}$ is the wave vector. These eigenvalues are referred to as modes in the following. Details on the mathematical tools solving Eq. (3.3) are provided in [81]. On a computer, the eigenproblem is discretized into a basis of N functions which result in a generalized eigenproblem consisting of $N \times N$ matrices. After ensuring Hermiticity and transversality by choosing a suitable discretization and basis one can apply standard linear algebra techniques to solve the eigenvalue problem. Unfortunately, in that case the memory needed scales $\sim N^2$ and the computation time scales $\sim N^3$. Thus, for large N, solving the eigenvalue problem might be an impossible task. Details on various discretization methods are, for example, discussed in [84]. But typically one is only interested in the few smallest eigenvalues $\omega_n(\mathbf{k})$ at each $\mathbf{k}$, called fundamental modes. This allows for iterative methods where e.g. only the p smallest eigenvalues are calculated. This method is saving computation resources since it only needs $O(N)$ operations and the required

storage is $O(N \cdot p)$ due to the sparsity of the matrices in finite-element methods [85]. In addition, the computation time is on the order of $O(N \cdot p^2)$ which for $p \ll N$ is much faster compared to the linear algebra method which scales with $O(N^3)$. These properties allow us to investigate the mode profiles of our waveguides using a standard laptop in a reasonable time [86]. Explicit results for the waveguide structures designed for this work are provided in the chapter 3.4. The software package used in this work to calculate the band structures is MPB [87].
The second type of simulation method used in this work are **finite-difference time-domain (FDTD) simulations**. In this kind of simulations, time and space are discretized on a lattice and the derivatives in Maxwell's equations ($\nabla\times$ and $\partial/\partial t$) are approximated by finite differences. Then both **E** and **H** are propagated in time using a leap-frog scheme where the **E** fields at time t are calculated from the field at $t - \Delta t$ along with $\mathbf{H}(t + \Delta t/2)$ which is calculated from $\mathbf{H}(t - \Delta t/2)$. Therefore both **E** and **H** are calculated time-step by time-step. Details on the discretization and the grid cells can be found in [86]. The main advantage of the FDTD simulation is its capability of extracting the linear response of a system at many frequencies by performing a single calculation. This is done by injecting a short pulse (having a large bandwidth) into the system and monitoring **H**(t) and **E**(t) at a measurement plane. These fields are then Fourier transformed to yield $\mathbf{E}(\omega)$ and $\mathbf{H}(\omega)$. Since this technique is especially useful for computing transmission spectra I employ it to simulate the coupling efficiency of the fiber-to-chip interface and the calculation of the local density of states (LDOS). The major drawback of the FDTD simulation is the long calculation time needed for typical nanostructures. This has several reasons: The spacing Δt must be small enough to ensure numerical stability which calls for a high-resolution setting where at each point in time Maxwell's equations, usually involving large matrices, must be solved. Then for 3D FDTD the time scales with the fourth power as a function of the resolution. The latter must be significantly large in order to accurately describe small features, like photonic crystal mirrors containing nanometer sized holes. Additionally, due to the uncertainty principle of the Fourier transformation, sharp features like cavity resonances rely on long simulating times to be completely recovered [81]. In this work, the runtime for 3D FDTD simulations ranges from hours to weeks and the used software packages are Lumerical [88] and MEEP [89].

3.3 Local density of states, Purcell- and β-factor

In contrast to many other studies on rare-earth-doped materials, in this work, the Er^{3+} ions are embedded into silicon nanophotonic waveguides. The integration of quantum emitters into waveguides has been demonstrated, for example, with quantum dots [90], NV^- centers [91] but also with rare-earth ions [92]. The question arises how the surrounding geometric structure of the waveguide affects the emission properties of the ions in the waveguide. In other words: How does the emitters'

geometric surroundings affect its emission properties?
The transition rate Γ between two states $\psi_{f,i}$ is given by Fermi's golden rule. It is defined via

$$\Gamma = \frac{2\pi}{\hbar} \left| \langle \psi_f | \, \mathbf{d} \, | \psi_i \rangle \right|^2 \mathrm{DOS}(\omega_{f,i}) \tag{3.4}$$

where $\langle \psi_f | \, \mathbf{d} \, | \psi_i \rangle$ is the dipole matrix element and $\omega_{f,i}$ the transition frequency between intial and final state [51]. Thus, by calculating the density of states, conclusions regarding the transition rate Γ can be drawn.
In quantum optics, the relevant quantity describing the geometric influence of the amount of power radiated by the same current is the photonic local density of states (LDOS) [93]. From chapter 3.1 Maxwell's eigenproblem is already known. The master equation eigenvalue problem can be expressed in terms of the electric field $\mathbf{E}(\mathbf{r})$:

$$\underbrace{\frac{1}{\epsilon(\boldsymbol{r})} \boldsymbol{\nabla} \times \frac{1}{\mu(\boldsymbol{r})} \boldsymbol{\nabla} \times}_{\boldsymbol{\Theta}} \boldsymbol{E}(\boldsymbol{r}) \quad \widehat{=} \quad \boldsymbol{\Theta} \boldsymbol{E}(\boldsymbol{r}) = \left(\frac{\omega}{c} \right)^2 \boldsymbol{E}(\boldsymbol{r}) \tag{3.5}$$

As before, $\boldsymbol{\Theta}$ must be Hermitian and semidefinite ensuring that the solutions of Eq. (3.5) have real eigenfrequencies $\omega^{(n)}$ and orthogonal eigenfields $\boldsymbol{E}^{(n)}$ [81]. One can think of eigenfrequencies forming a discrete set, ω_n, where $n = 1, 2, 3, ...$ which can be adapted later for infinite systems by placing the limit on a certain n. For sake of simplicity, $c = 1$ in the following. The density of states (DOS) is defined as:

$$\mathrm{DOS}(\omega) = \sum_n \delta \left(\omega - \omega^{(n)} \right) \tag{3.6}$$

where δ is the Kronecker delta. The integral over the DOS is then the number of modes present in the integration interval. Normalizing the eigenfields such that $\left\langle \boldsymbol{E}^{(n)}, \boldsymbol{E}^{(n)} \right\rangle = 1$ allows for the definition of a local density of states per-polarization:

$$\mathrm{LDOS}_l(\boldsymbol{r}, \omega) = \sum_n \delta \left(\omega - \omega^{(n)} \right) \epsilon(\boldsymbol{r}) \left| \boldsymbol{E}_l^{(n)}(\boldsymbol{r}) \right|^2 \tag{3.7}$$

which is related to the density of states via:

$$\mathrm{DOS}(\omega) = \sum_{l=1}^{3} \int \mathrm{LDOS}_l(\boldsymbol{r}, \omega) d^3\boldsymbol{r} \tag{3.8}$$

In this work, the DOS is unraveled into a polarization-dependent LDOS since I am interested in the different light polarization components in the waveguide. So the LDOS is a measure of the energy density of the electric field of each mode in the direction l at position $\boldsymbol{r}$. Here l is the polarization of the electric field pointing along the three space coordinates; the sum is running over $l = 1, 2, 3$ [94]. It is then possible

to derive an expression for the power as a function of a dipole current source using (3.1) and Poynting's Theorem [82]. The interested reader is referred to [95] for a detailed derivation. I restrict myself here to the final expression for the radiated power P, which is given by:

$$P = \frac{\pi}{4} \sum_n \left| \left\langle \boldsymbol{E}^{(n)}, \epsilon^{-1} \boldsymbol{J} \right\rangle \right|^2 \delta \left(\omega - \omega^{(n)} \right) \tag{3.9}$$

If a dipole current source $\mathbf{J}(\mathbf{r})\mathbf{e}_l \delta(\mathbf{r} - \mathbf{r}_0)$ is placed at position $\mathbf{r}_0$ with unit vector $\mathbf{e}_l$ in direction $l \in \{1, 2, 3\}$ the inner product in Eq. (3.9) simplifies to $\left| \left\langle \boldsymbol{E}^{(n)}, \epsilon^{-1} \boldsymbol{J} \right\rangle \right|^2 = \left| E_l^{(n)}(\mathbf{r}_0) \right|^2$. By comparing Eq. (3.7) and Eq. (3.9) the LDOS can be expressed as a function of the total radiated power:

$$\mathrm{LDOS}_l(\mathbf{r}_0, \omega) = \frac{4}{\pi} \epsilon(\mathbf{r}_0) P_l(\mathbf{r}_0, \omega) \tag{3.10}$$

Here $P_l(\mathbf{r}_0, \omega)$ accounts for the radiated power by the current $\mathbf{J} = \mathbf{e}_l \delta(\mathbf{r} - \mathbf{r}_0) e^{-i\omega t}$ and from Eq. (3.10) it is clear that the local density of states is directly proportional to the total radiated power P_l. The LDOS can be computed in a FDTD simulation by placing a pulsed point-dipole source with power $p(t)$ of the form $\mathbf{e}_l \delta(\mathbf{r} - \mathbf{r}_0) p(t)$ in the waveguide and the Fourier transforms $\hat{\mathbf{E}}_l(\mathbf{r}_0, \omega)$ of the fields at $\mathbf{r}_0$ are summed up. A single calculation then yields the complete LDOS spectrum at position $\mathbf{r}_0$, given by [96]:

$$\mathrm{LDOS}_l(\mathbf{r}_0, \omega) = -\frac{2}{\pi} \epsilon(\mathbf{r}_0) \frac{\mathrm{Re}\left[\hat{\mathbf{E}}_l(\mathbf{r}_0, \omega) \hat{p}(\omega)^* \right]}{|\hat{p}(\omega)|^2} \tag{3.11}$$

Here $\hat{\mathbf{E}}$ and $\hat{p}$ denote the Fourier transforms of the electric field and the power, respectively. The normalization $|\hat{p}(\omega)|^2$ is needed, in order to obtain the radiated power by a unit-amplitude dipole similar to computing the radiation resistance in electrical antennas. The central question here is: How does the emission of the Er^{3+} ions in a waveguide compare to the same emitter in bulk silicon?
From a simulating point of view, this is straightforward: The calculation of the LDOS is done twice for two separate geometries. In the first run, the geometric setting is the waveguide with the embedded emitter. In my case, this is an Er^{3+} ion in a silicon waveguide. The outcome of this first run is compared to the result of the second simulation run, where an emitter is embedded in a bulk, silicon block. By normalizing the waveguide simulation by the bulk simulation, the emission rate into a waveguide mode for a dipole emitter relative to the spontaneous emission rate of the same emitter in a homogeneous material can be quantified. This factor describing the enhanced spontaneous emission rate is called Purcell-factor F_P.

Another important measure is the β-factor which is a measure of the probability of a photon being emitted into the waveguide. The propagation mode factor is

defined as [97]:

$$\beta = \frac{\gamma_{\text{wvg}}}{\gamma_{\text{wvg}} + \gamma_{\text{rad}} + \gamma_{\text{non-rad}}} = \frac{\gamma_{\text{wvg}}}{\gamma_{\text{total}}} \tag{3.12}$$

which applies to a photon emitter within a waveguide. Here γ_{wvg} is the emission rate into a waveguide mode, γ_{rad} is the spontaneous emission rate into a continuum of radiation and $\gamma_{\text{non-rad}}$ is the non-radiative decay rate due to various relaxation processes associated with the emitter. In case $\beta = 1$, all radiated light would be emitted into the waveguide. The calculations of these figures of merit related to the waveguide geometries are discussed in detail in chapter 6.

3.4 Waveguide designs

In this section, I will briefly review the two types of optical waveguides used in this work highlighting the relevant geometric parameters and optical properties.

Ridge waveguide

A ridge waveguide is a strip of a high refractive index material n residing on a low index layer or vacuum as illustrated in Fig. 3.1 b): The refractive index contrast of the

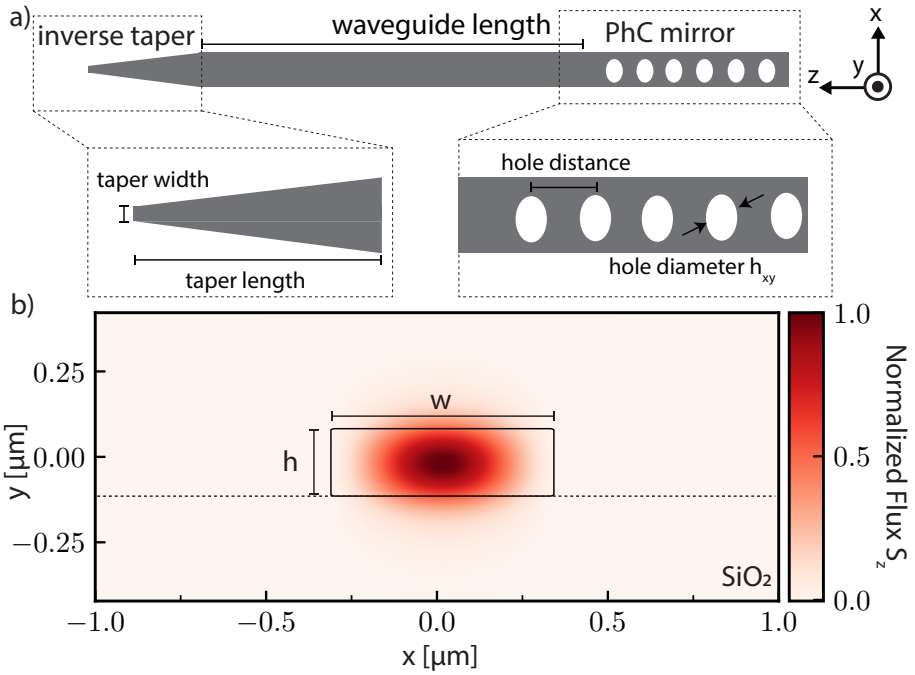

FIGURE 3.1: **Mode profile of a ridge waveguide.** a) Top view sketch of a waveguide of length L in the xz-plane featuring an inverted taper in front and a mirror at the end. b) Cross-sectional view. The silicon ridge waveguide centered at $y = 0\,\mu m$ resides on a $3\,\mu m$ buried oxide layer (SiO_2, below dashed line). The mode profile shows the energy flux S_z in z-direction for a waveguide of width w = 700 nm and a height of h = 220 nm.

silicon strip at $n_{Si} = 3.5$ is significantly higher than the one of the buried oxide layer at $n_{SiO_2} = 1.45$. Thus, the light is confined within the strip due to total internal reflection. The length of these waveguides can range from a few hundred micrometers up to a millimeter. By choosing a suitable set of geometric parameters the structure can be designed to guide single light modes only. The waveguide cross-section with the energy flux in z-direction S_z is shown in Fig. 3.1 b). The mode profile is calculated using the frequency-domain eigensolver introduced in chapter 3.2.
The antinode at the center of the waveguide indicates that this mode represents the fundamental mode of the device. I use a tapered fiber technique to evanescently couple to the waveguides, a technique pioneered using Si_3N_4 waveguides [98]. This method requires an inverse taper in front as shown in Fig. 3.1 a). In my design the

waveguide width is tapered down from 700 nm to 150 nm over a length of 30 µm. Details regarding the fiber coupling technique are presented in chapter 3.6.
The waveguide is terminated by a photonic crystal (PhC) mirror consisting of a set of sub-wavelength, periodic, and elliptical holes designed to reflect light back into the waveguide. Simulations on the hole design used in the mirrors in this work are presented in appendix B. The mirror reflectivity and the waveguide losses can be measured by comparing the reflectivity of waveguides of different lengths. However, discrimination between coupling loss and mirror loss is more subtle. This technique also allows for measuring in reflection which doubles the optical depth since light that travels towards the mirror, is reflected and travels back, increasing the probability of exciting a waveguide embedded ion. The ridge waveguides are used in the experiments presented in chapter 5 and 6.

Rib waveguide

In chapter 7 I use another type of waveguide geometry called rib waveguide. This geometry is similar to that of a ridge waveguide but this geometry features larger mode sizes which makes the need couplers and mode conversion for coupling obsolete. In addition, the experiments are conducted in a transmission setup geometry with two cleaved fibers, such that reflectors in the waveguide are not needed here. The drawing in Fig. 3.2 a) sketched the transmission setup and Fig. 3.2 b) shows the waveguide cross-section and the calculated fundamental mode.

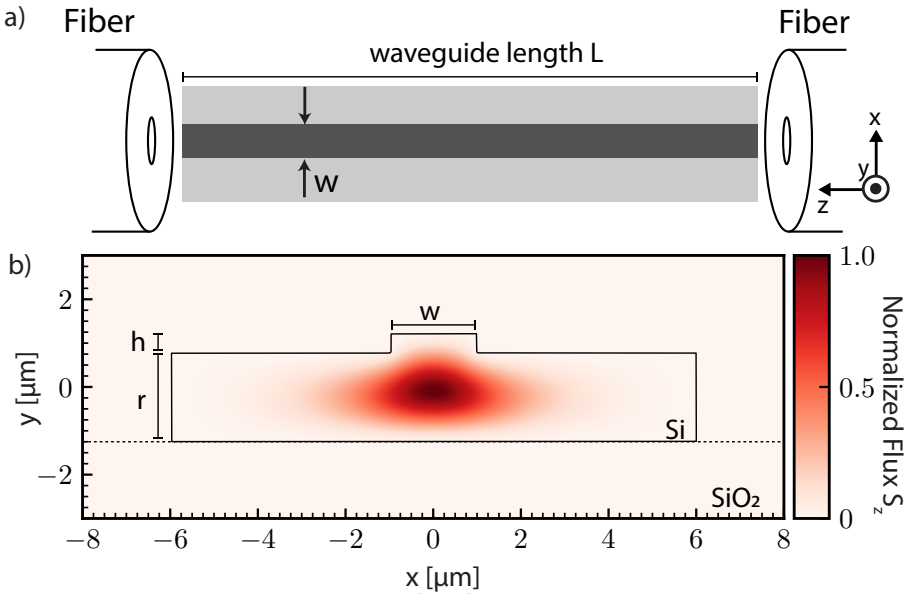

FIGURE 3.2: **Sketch and mode profile of a rib waveguide.** a) The rib waveguide in a transmission configuration. Light is coupled in on one side, travels along the waveguide and is collected at the end with a second fiber. b) The waveguides xy-cross-section and the energy flux S_z in a rib waveguide. The rib parameters are $h = 0.5\,\mu m$, $r = 2\,\mu m$ and $w = 2\,\mu m$.

The rib waveguide resembles the strip waveguide but the core part is expanded partially to a high index planar layer on top of a lower refractive index material. In general rib waveguides fulfill the single mode condition, when

$$\frac{w}{h+r} \leq \alpha \frac{\widetilde{r}}{\sqrt{1-\widetilde{r}^2}}, \qquad 0.5 \leq \widetilde{r} \leq 1 \tag{3.13}$$

where $\widetilde{r} = r/(h+r)$ and w, r and h are illustrated in Fig. 3.2 b) and $\alpha = 0.3$ is a constant [99]. By choosing a suitable set of geometric parameters $h = 0.5$ µm and $r = w = 2$ µm, a value of $\widetilde{r} = 0.8$ is obtained. Thus the waveguide design is single-mode which is confirmed when simulating the structure by solving the frequency-domain eigenproblem. The fundamental mode is centered in the waveguide as shown in Fig. 3.2 b).
The mode is to a large extent confined in the device layer and only has minimal contact with the etched parts which yields very low transmission losses compared to ridge waveguides if the material absorption is negligible. Therefore the waveguides can be several millimeters up to centimeters long and still exhibit low transmission loss increasing the optical depth. Coupling to the waveguide is achieved from both sides of the chip using cleaved optical fibers. This yields reasonable coupling efficiencies due to comparable mode diameters of high-NA fibers and the rib waveguide mode. Details on the coupling technique are presented in chapter 3.6.

3.5 Fabrication process

In Fig. 3.3 the general fabrication steps are summarized. A detailed description of all nanofabrication processes is given in appendix A.2.
The starting material is a commercially available silicon-on-insulator (SOI) wafer with a thin silicon top layer, referred to as the device layer. The device layer has a thickness of either 220 nm or 2.5 µm, defining the waveguide thickness later on. The device layer resides on top of an insulating layer of SiO_2 with a thickness on the order of a few microns as indicated in Fig. 3.3 a). The wafers (or the already diced chips) are first sent for ion implantation to commercial suppliers (see appendix and Fig. 3.3 b)). The targeted implantation profile was either a homogeneous distribution along the sample z-direction or a Gaussian distribution with a maximum at the center of the device layer depending on the respective waveguide geometry. The parameters of the different implantation runs are provided in the appendix.
For patterning the samples, first a diced $10x10$ mm chip is spin-coated with ZEP520A, a high-resolution, positive electron beam resist. The covered chip is then exposed to a scanning electron beam inside an electron beam lithography machine (Ebeam) which defines the waveguide structure. The electron beam causes chain scission of the polymers of the resist at the exposed areas. After the removal of the exposed areas by a developer, a resist mask on top of the device layer is left behind (see c) - e)). The Ebeam-defined pattern is then transferred onto the chip using reactive

ion etching (RIE) as illustrated in Fig. 3.3 f). The exact parameters of this process are of great importance since the waveguide loss strongly depends on the sidewall roughness and steepness. These two parameters thus have a direct impact on the spectroscopic experiments later on. After the etching, the resist residues are removed,

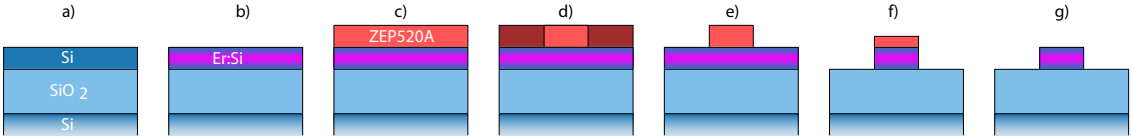

FIGURE 3.3: **Nanostructuring process.** A SOI chip (a) is first implanted with erbium (b) and then processed using electron beam lithography and reactive ion etching (c) -g)). Details in the main text. Adapted from [100].

revealing the silicon waveguides, shown in Fig. 3.3 g). Due to the fiber side-coupling techniques and limited space in the cryostat, the nanophotonic structures must be in close vicinity of the chip edge, typically a few hundred micrometers. Positioning the waveguides at the edge already during the lithography step is not possible because the resist forms edge beads at the chip edges. Therefore the chips containing the waveguides must undergo a final fabrication step where the chip edge is removed close to the waveguide and waveguide tapers. This is done using a diamond cleaver with which the chip is scratched and subsequently broken forming a cleaved edge close to the waveguide edge. However, this technique is inaccurate due to the limited positioning accuracy on a micrometer scale. Alternatively, the fabricated chips can be mechanically polished. To this end, the chip is covered with a protective resist and then polished from the side using very fine polishing sheets until the waveguide tapers or tips are exposed. Using this technique the distance from the chip edge to the waveguide can be precisely controlled. The polishing technique is also used for the rib waveguides where the goal is to couple from the side to the waveguide which therefore needs a facet at the chip edge.

3.6 Fiber-to-chip coupling

In this section, I present two approaches for coupling light into nanophotonic waveguides using glass fibers. Another approach would be a free-space cryogenic setup, however, the need for special components like high numerical aperture objectives withstanding low temperatures makes this approach more cost demanding and creates a significant technical overhead through the use of free-space optics. In Fig. 3.4 I illustrate the fiber-coupling techniques used in this work. Fig. 3.4 a) shows the coupling of light from a tapered fiber (yellow) into a nanophotonic ridge waveguide which is terminated by a photonic crystal mirror. Due to the small size of both fibers and waveguides, many structures on the same chip can be tested and eventually used for experiments. In contrast to that, the butt-coupling technique is used for the rib waveguides due to the larger diameter of its fundamental eigenmode shown in Fig. 3.4 b). The cleaved fiber (yellow) is aligned with the rib waveguide and subsequently glued to the chip. This approach reduces the experimental overhead since positioning within the cryostat is not required. I review these two approaches in more detail in the following. Details regarding the fabrication of the tapered fibers are documented in appendix A.

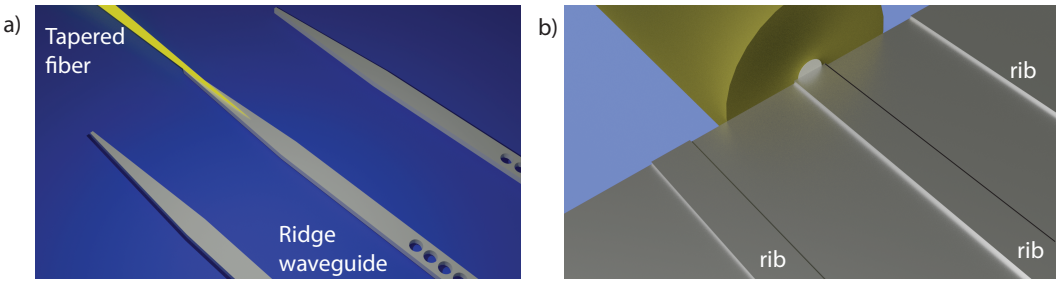

FIGURE 3.4: **Fiber-coupling techniques**. Image a) shows a tapered-fiber coupled to a mirror-terminated ridge waveguide. Picture b) illustrates the side coupling to a rib waveguide using a cleaved fiber. Both drawings are not to scale.

Tapered-fiber coupling

I use a single-sided, conical tapered fiber to evanescently couple light into and out of the ridge waveguides as illustrated above. This technique has already been successfully used for coupling to another dielectric-, nanophotonic structures [98, 101]. The working principle is based on an adiabatic transfer of the fundamental mode of the tapered fiber to the fundamental mode of the nanophotonic waveguide. For that to work the tapered fiber needs to be in physical contact with the waveguide taper such that the mode transfer is possible.
In Fig. 3.5 a) a scanning electron microscope (SEM) image of a tapered fiber is shown. It is fabricated using a single-mode glass fiber (SMF-28) which is stripped off its acrylate cladding, cleaved, and then dipped into hydrofluoric acid (HF 50%) [102, 103].

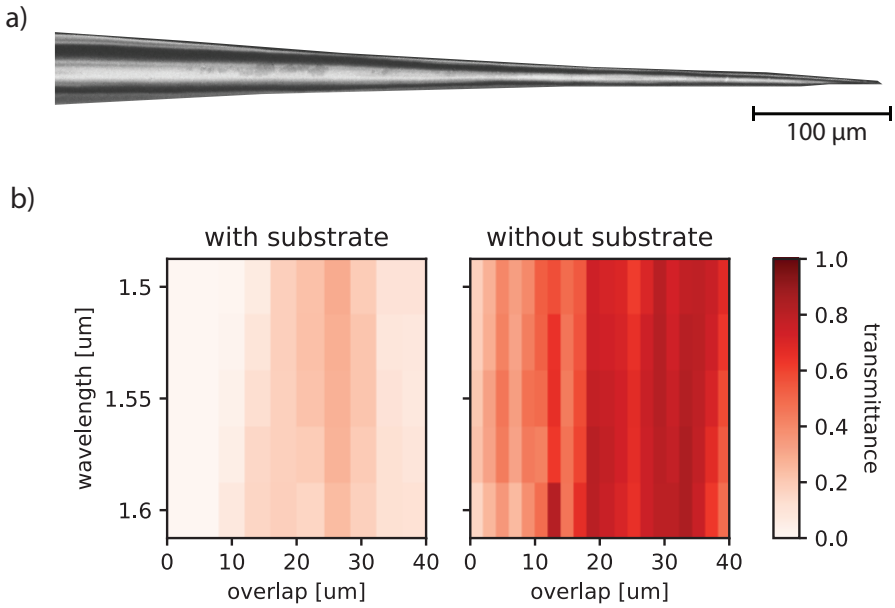

FIGURE 3.5: **Tapered-fiber coupling.** a) SEM image of a tapered fiber. The foremost part is used for coupling into the waveguide. b) FDTD simulations for a tapered-fiber coupling to a waveguide on SiO_2 (left) and suspended in vacuum (right).

Then the acid is slowly pumped from the etching vessel such that its level decreases at a constant rate and a conical tip is formed [104]. The fabrication procedure is described in detail in appendix A.1. The tapered fiber is characterized by the angle of its tip α and the length of the fibers' subwavelength part. The angle typically varies between 3° and 5° due to fabrication imperfections. To ensure adiabatic coupling the waveguide cross-section is slowly reduced along the propagation direction of the light such that all the optical power remains in a single eigenmode of the composite waveguide, while the coupling to other modes is suppressed. This holds for both the waveguide and the tapered fiber. In general, the overlapping length z_t must be large compared to the length scale z_b along which the waveguide and fiber cross-section is reduced where $z_b = \lambda/n_\nu - n_\mu$. Here λ is the vacuum wavelength and $n_{\nu,\mu}$ the effective refractive indices of the first two waveguide eigenmodes [105]. In my case, both fiber and waveguide are tapered over several tens of micrometers ensuring $z_b < z_t$. In Fig. 3.5 b) the results of FDTD simulations are shown. Here, an eigenmode dipole source of known energy is placed into the tapered fiber and then the fields are propagated in the direction of the tapered cone towards the waveguide. Since the tapered fiber is coupled to the waveguide taper, the light mode adiabatically transfers from the tapered fiber into the waveguide. There the flux is measured and the overall transmission from the fiber into the waveguide is determined. What is important here is the overlap length between the fiber and the waveguide. This length is plotted on the x-axis. Furthermore, the wavelength dependence of the transmission is extracted which is plotted on the y-axis, highlighting the broadband capabilities of this coupling technique. The color of the pixels corresponds to the respective

transmission value. The tapered fiber angle was fixed at 3° and the waveguide was tapered from 700 nm down to 150 nm. In the left-hand side image the waveguide is placed on SiO_2: For an overlap length of 20 to 40 µm the transmission is no more than 20%. This is not in agreement with previous values found e.g. in free-standing diamond structures [101] where the transmission efficiency was close to 100%. The reason for the smaller transmission is the layer of SiO_2 beneath the silicon waveguide. There a significant fraction of the light also couples from the tapered fiber into the SiO_2 layer since both share the same refractive index. Adapting the simulation and removing the SiO_2 below the waveguide nicely recovers the very large transmittance from the tapered fiber to the silicon waveguide in agreement with previous work. This means that a free-standing waveguide would lead to very large coupling efficiencies. However, removing the buried oxide layer strongly affects the stability of the suspended waveguide making it highly susceptible to mechanical vibrations and possible damage. Due to the large fabrication overhead and an unsuitable cryogenic setup the oxide removal was not addressed in this project. In the experiment, one-way coupling efficiencies of 10- 15% are routinely achieved. The deviation from the simulated ~ 20% coupling efficiency can be attributed to fabrication imperfections of both tapered fiber and nanophotonic waveguide as well as the lack of precision in moving the chip inside the cryostat.

Fiber-butt coupling

The butt-coupling technique is used in combination with the rib waveguides presented earlier in this chapter and schematically shown in Fig. 3.4 b). The waveguide fundamental mode is ~ 2 µm in diameter which is on the same order of magnitude as the mode field diameter of a high-NA optical fiber. The key idea is to use a cleaved fiber, directly connect it to the waveguides' end facet and use glue to fix the coupling at room. When cooling the glued sample to 2 K, the fiber coupling persists. Also, no additional mode conversion in necessary. As a coarse estimate of the coupling efficiency I can calculate the overlap integral between the fiber mode and the rib waveguides' fundamental eigenmode. This overlap integral can be used as a rough measure for the transmission η. For two Gaussian beam profiles, η can be estimated using

$$\eta = \frac{4(w_1^2 w_2^2)}{\left(w_1^2 + w_2^2\right)^2} \exp\left(-\frac{2(\Delta x)^2}{w_1^2 + w_2^2}\right) \tag{3.14}$$

where $w_{1,2}$ corresponds to the mode diameters of the fibers' and the waveguides' fundamental mode. Here, Δx is the relative transverse displacement between fiber and waveguide [106]. The major limitation is the size mismatch between waveguide and fiber mode. Additionally, the position of the cleaved fiber facet must be precisely aligned to the waveguide minimizing Δx. The details on the setup used for alignment

are discussed in chapter 7. As mentioned before, spectroscopy is performed in transmission as well as in reflection. Therefore, both end facets of the rib waveguide need to be connected to fiber. This is achieved by gluing the cleaved fiber to the edge of the waveguide and then mounting the glued sample into a cryostat. This approach was already successfully employed to glue angle-polished fiber to grating couplers in a planar geometry and cleaved fibers to Er:YSO crystals with subsequent cooling of the device to ~ mK temperatures [107, 108]. I adapt this technique to glue the cleaved fibers to the silicon chip in a side-coupling geometry. The difficulties are the smaller surface of the fiber-to-chip interface compared to geometries used in previous work, the small tolerance of the transverse displacement Δx as well the glues' temperature-dependent expansion coefficient. During cooldown the latter affects the relative alignment of fiber and waveguide, thus altering the coupling efficiency η. At base temperature, the one-way coupling efficiency typically is between 1% and 2% for the all-glued approach where both fibers at each end of the waveguide are glued to the chip. Another possible loss source is the roughness of the waveguides end facet. Since I use mechanical polishing for coupling to the rib waveguide, its end facets are not perfectly planar and exhibit some finite roughness. However, the loss due to the end facet roughness is negligible compared to the major loss contribution: The mode mismatch between fiber and waveguide as well as the relative displacement of both.

Chapter 4

Experimental setup

In this section, I review the experimental setup. The setup underwent several modifications over the course of this work so I will refer here to the latest version. The setup is downwards compatible meaning that in the existing version all the presented experiments in this work can be performed. I will provide the reader only with the general version of the setup. Additional and relevant parameters are provided in the respective experimental chapters.

4.1 Measurement configuration and laser setup

A sketch of the fluorescence spectroscopy measurement setup is shown in Fig. 4.1:

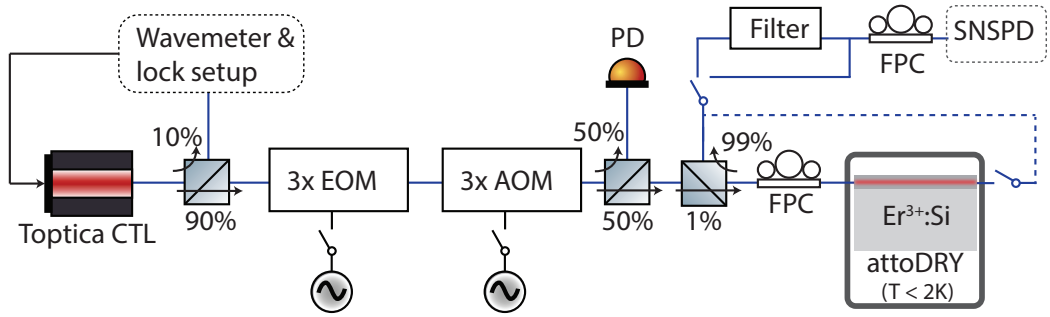

FIGURE 4.1: **Optical measurement setup.** Schematic sketch of the experimental setup. Details and abbreviations are given in the text.

A fiber-coupled laser (Toptica CTL1500) is used which features a large wavelength tuning range from 1460 nm to 1570 nm. The laser is connected to a wavemeter (Bristol 771A-NIR) which is specified with an absolute accuracy of around 100 MHz. In addition, the laser can be frequency-stabilized using a phase-lock to a frequency comb (Menlo Systems FC1500-250-ULN) which in turn is referenced to an external cavity (Menlo Systems ORS1500) with sub-hertz stability. Three concatenated electro-optic phase modulators (EOM; iXblue MPZ-LN-10/20) are used for sideband generation which are needed when measuring the homogeneous linewidth. Afterwards, three acousto-optic modulators (AOM; Gooch&Housego) are used for pulse generation. Together these acousto-optic modulators exhibit suppression of 150 dB. The rise/fall time depends on the models' frequency (110, 200 or 300 MHz) and ranges from 6 ns to 25 ns. However, due to the used pulse sequence electronics, the minimum pulse

length is limited to 50 ns. For large parts of the work in this thesis, both electro-optic and acousto-optic modulators were driven by a homebuilt direct digital synthesis (DDS) radio-frequency (rf) source. In the most recent experiments, however, the rf signal is generated by an arbitrary waveform generator (AWG; Zurich Instruments HDAWG). The pulses are then monitored using an InGaAs photodiode (PD; Thorlabs PDA05CF2) and a power meter (Thorlabs PM101A) is used for calibrating the power. Up to now all beam splitters (Thorlabs PN1550) and other optical components are polarization-maintaining (PM) devices. After the 99:1 beamsplitter (Evanescent Optics Inc.) a bend-insensitive single-mode (SM) fiber (Corning ClearCurve) is used in combination with a fiber polarization controller (FPC, Thorlabs MPC220) to align the input polarization with the preferred direction of the waveguides' fundamental mode. It is worth noting that from this point on low loss-fiber connectors (Diamond E-2000 series) are used. The fibers are then passed into the cryostat using Teflon feedthroughs. The coupling to the waveguides is either performed using tapered or cleaved single-mode fibers, where the details are discussed in chapter 3.6. After excitation with a light pulse, the implanted ions emit a fluorescence signal which can leave the waveguide in the cryostat either in reflection or in transmission as indicated by the switch and the dashed line in Fig. 4.1. The cryogenic part of the setup is presented in section 4.2. The fluorescence light is passed onto a superconducting single-photon detector (SNSPD; PhotonSpot or ID Quantique) housed in another cryostat at a temperature below 1 K. Since the quantum efficiency of these detectors is polarization-dependent I again optimize the signal using a fiber polarization controller. For most of the experiments, the detector is operated at a quantum efficiency of $\eta_{\mathrm{QE}} = 80 - 90\%$ with associated dark counts rates of $10 - 30$ Hz. The overall detection efficiency η_{det} of photons emitted in the waveguide was around $\eta_{\mathrm{det}} = 6\%$, mainly limited by transmission-induced losses of the optical components from the cryostat to the superconducting single-photon detector and the respective fiber-to-chip interface. The fluorescence can optionally be filtered using a tunable band-pass filter (WL Photonics) in front of the detector and a fast electro-optic modulator switch (Agiltron UltraFast Switch) is used for gating during excitation to prevent the detectors from latching (not shown in Fig. 4.1).
For generating the TTL pulse sequences for gating the rf sources a field-programmable gate array (FPGA, National Instruments cRIO-9035) is used which has a minimum timing resolution of 50 ns. The counts on the detectors are registered using a time-bin digitizer (Swabian Instruments TimeTagger Series 20) and streamed to a computer for processing.

4.2 Cryogenic setup

To suppress the interaction of erbium dopants with phonons and resolve the transition between the lowest CF levels, the experiment is operated at liquid helium

temperatures. I employ a closed-cycle cryostat (Attodry2100) with a base temperature below 2 K equipped with a 9 T superconducting magnet. The cryostat is a top-loading system meaning that the sample is mounted at the end of a $\sim$ 1 m long stick which is then immersed into the sample space which has a 50 mm diameter. A drawing of the cryogenic sample mount is shown in Fig. 4.2. The sample is residing in Helium exchange gas which ensures proper thermalization with the vertical temperature inset. The titanium sample mount is fixed to the sample stick using four rods. For imaging both, tapered fiber and chip, an aspheric lens (Thorlabs AL1512) is used. The tapered fiber is fixed in a fiber mount with its tip protruding 0.1 - 0.5 mm from the edge of the mount. This length depends on the distance of the waveguides from the chip edge which varies due to the mechanical polishing of the chips after fabrication. The Er^{3+}:Si chip is mounted on a 3-axis stack of piezo steppers (Attocube ANPx312 & ANPz102) which allows for traveling several millimeters at base temperature. A resistive thermal sensor (Cernox 1030) is sandwiched between the sample mount and the piezo stack enabling accurate temperature measurements close to the sample. Temperature readout is done via a cryogenic temperature controller (SRS CTC100) which can be also used for sample heating if required. The tapered fiber is fixed to a mount using spring-loaded clamps. The springs protect the fiber from being squashed by too much pressure applied to the clamps during assembly or caused by thermal expansion during cooldown. The sharp tip of the tapered fiber exits the mount under a 3° angle relative to the horizontal plane such that the tapered end lies flat on the chip surface. The not tapered end is spliced to a single-mode fiber exiting the cryostat at the top via a drilled Teflon feedthrough. When measuring in reflection, the same fiber is used for guiding the excitation pulse as well as the resulting fluorescence. On top of the cryostat, a recessed window is used for monitoring the sample position inside the sealed vertical temperature inset. A blue LED (Thorlabs M490L4) is used in combination with a pellicle (Thorlabs BP145B1) for illumination and a CCD camera (Thorlabs CS165MU) is used for imaging. To ensure a good view of the sample a 1:1 telescope is mounted on the sample stick and another lens in front of the CCD camera is used for focusing. Cables used for operating the piezo steppers are fed into the cryostat using vacuum feedthroughs (Fischer 105 series) from the top of the sample stick. Coupling to a waveguide at base temperature works as follows. First, the fibers' reflectivity is calibrated using a single-mode retroreflector (Thorlabs P5-SMF28ER-P01-1). A value of more than 1% reflectivity of the tapered fiber indicates that it is broken e.g. the tip is cut off or there is some damage along with the fiber which calls for replacement. Otherwise, the sample is slowly driven towards the tip of the tapered fiber in upwards direction using the piezo steppers. The moment the tapered fiber touches the silicon device layer next to a waveguide the reflection signal drops since the light is forwarded into the silicon device layer. Then the fiber is carefully dragged on the silicon surface until it comes in contact with the waveguide and its taper. The signal then increases and can be optimized by tuning the overlap between fiber and waveguide. I routinely

achieve one-way coupling efficiencies of 10% depending on the quality of both the fabricated nanostructures and the tapered fiber as well as the proper alignment of fiber and sample during assembly of the sample mount.
In the case of transmission measurements using the fiber butt-coupling technique all fibers are glued at room temperature and mounted on the sample stick. This approach makes the piezo steppers and imaging optics obsolete, which reduces the experimental overhead.

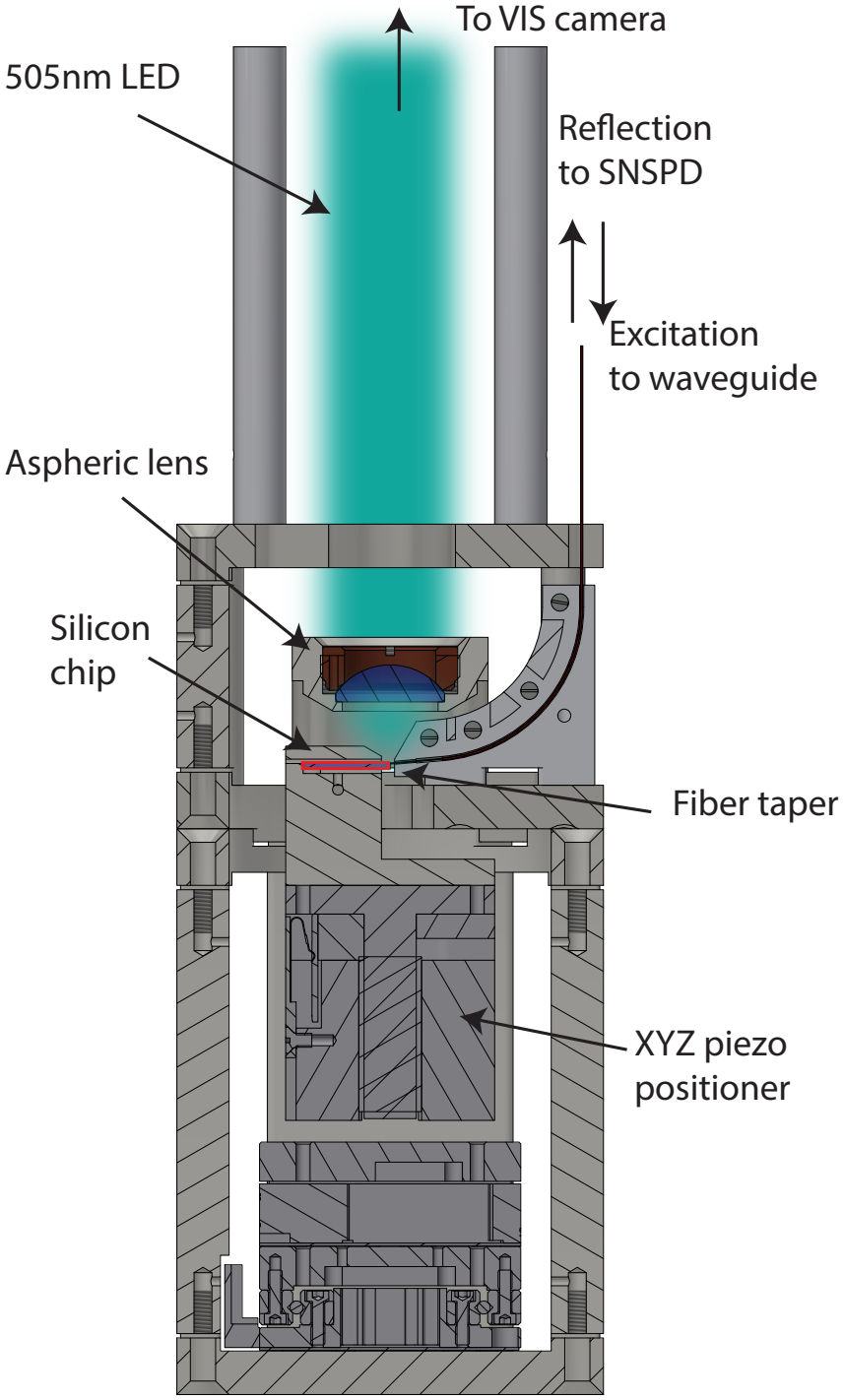

FIGURE 4.2: **Cryogenic setup.** Drawing of the cryogenic part of the setup. Details are discussed in the main text.

Chapter 5

Erbium dopants in silicon nanophotonic waveguides

In this chapter, the experiments on the first generation of Er^{3+}:Si samples are described. I discuss the sample properties, spectroscopy data, and investigate the Zeeman effect of the fluorescence lines found. The work described in this chapter has been published in [109].

5.1 Sample specifications

As a starting material, a commercially available, Czochralski (CZ)-grown silicon-on-insulator wafer is used. The silicon device layer has a thickness of 220 ± 10 nm placed on top of a buried oxide layer of 3000 ± 50 nm thickness. The device layer is boron p-doped with a sheet resistance of R = 10±1.5 Ω·cm. The wafer is diced into 10x10 mm chips in <110> direction and sent for implantation. The implantation of erbium in natural isotope abundance was performed at room temperature using 198 keV acceleration voltage with a targeted dose of 1×10^{14} cm^{-2}. However, sparking of the source during implantation yielded a lower dose. By secondary ion mass spectrometry (SIMS), an actual dose $\lesssim 1 \times 10^{11}$ cm^{-2} was determined. The implantation profile follows an approximate Gaussian distribution along the z-axis of the device layer. SIMS measurements of implantation dose and profile together with data on impurities in the silicon substrate are provided in appendix B.3.
After implantation the Er^{3+}:Si chip is annealed at 700 °C for 10 min using the procedure described in appendix A.2. The high temperature repairs the implantation induced crystal damage. After annealing, the waveguides are fabricated in a clean room environment. They have a thickness of 220 nm, a width of 700 nm, a length of 0.4 mm and are terminated with a broadband reflector. At this stage of the experiment, the detection efficiency of a photon emitted in the waveguide was around 2%. The limiting factors were small coupling efficiencies and losses in the experimental setup induced by various optical components and the waveguide sidewall roughness.

5.2 Resonant spectroscopy

Fig. 5.1 shows a typical fluorescence spectrum using the setup described in chapter 4. The laser is scanned in steps of 1 pm where at each wavelength setpoint a fluorescence time trace is taken after the laser is switched off. During each excitation pulse, the laser frequency is modulated by a few hundred megahertz to avoid bleaching by persistent spectral hole burning to long-lived spin states, an effect which has also been observed in other rare-earth-doped crystals like YSO [61, 110] and $LiNbO_3$ [111]. Modulating the laser frequency is achieved using the laser built-in grating which is attached to an AC voltage modulated piezo. Excitation pulses of 1 ms duration are applied and the subsequent fluorescence decay is measured averaging over a few thousand fluorescence traces. The employed technique is sensitive to all dopants, that decay radiatively and not limited to impurities which are excited by above-band-gap excitation. I find a series of sharp peaks numbered from one to nine in the above plot. In the following, these lines will be referred to as "sites". The existence of these peaks is typical for rare-earth doped crystals with a low ion concentration [112] proving that the setup is capable of performing spectroscopy on few-ion ensembles. All observed peaks are well fit by Lorentzian curves with inhomogeneous linewidths ranging from 1 to 4 GHz. The major limitation in these measurements is the low photon count rate, where 0.15 clicks per excitation pulse are measured on the brightest line. This did ultimately prevent more detailed investigations since this would call for extremely long integration times. An effect I came across while performing these measurements was two-photon absorption (TPA) which is a non-linear effect encountered in silicon in general [113] and especially in waveguides [114, 115]. In TPA two photons of the same energy are absorbed simultaneously, exciting an atom from the valence band to the conduction band with the energy increase being equal

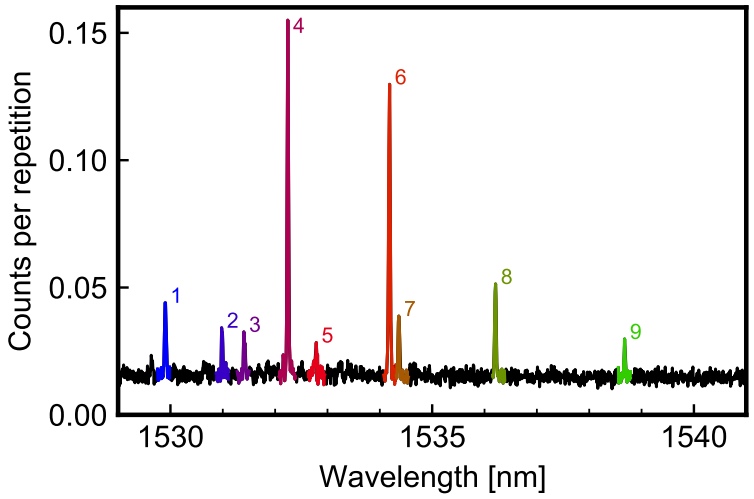

FIGURE 5.1: **Resonant fluorescence spectrum.** The laser is scanned from 1530-1540 nm while monitoring the fluorescence decay at each respective wavelength. The found peaks are numbered and color coded to which I will refer to throughout this chapter.

to the sum of the photon energies leaving a free exciton behind. This is a nonlinear absorption process at high optical intensities, where the absorption coefficient is proportional to the optical intensity. Here, I did observe an increase in the background signal when using high optical pulse powers (~ 1 mW). This effect can be attributed to TPA forming excitons, which can then recombine via an erbium-related defect directly or being bound to a trap-state featuring a time-lagged recombination [116]. Typically, these defects are located close to the conduction band, which makes them susceptible to this kind of relaxation process [47]. In the next generation of samples, some of these optically active sites are discovered and investigated in more detail. The observation at high excitation pulse powers made here, thus resembles a carrier-mediated excitation causing very broad emission spectra. To avoid such broadening the optical pulse power is decreased until the maximum signal-to-noise ratio, i.e. the maximum difference between background signal and amplitude on peak 4 is achieved. The typical excitation pulses power was then ~ 10 µW measured in the fiber towards the sample.

A recent experiment of another group showed several lines that were identical to the ones found here [117]. However, in their experiment, many more resonances appeared which might be due to the heavy oxygen co-doping in their samples. This is known to facilitate the formation of a plethora of different, low symmetry Er-O complexes [47]. A closer investigation of the associated crystal field levels to the sites found was not possible here due to the small fluorescence signal and the lack of experimental equipment at that time.

Fig. 5.2 shows a high-resolution scan of the two strongest peaks from the overview scan in Fig. 5.1. Single Lorentzian curves fit the data very well and inhomogeneous linewidths of Γ_{inh} = 1.72(3) GHz for peak 4 and Γ_{inh} = 2.39(4) GHz for peak 6 are extracted.

These values are three orders of magnitude smaller than in previous measurements

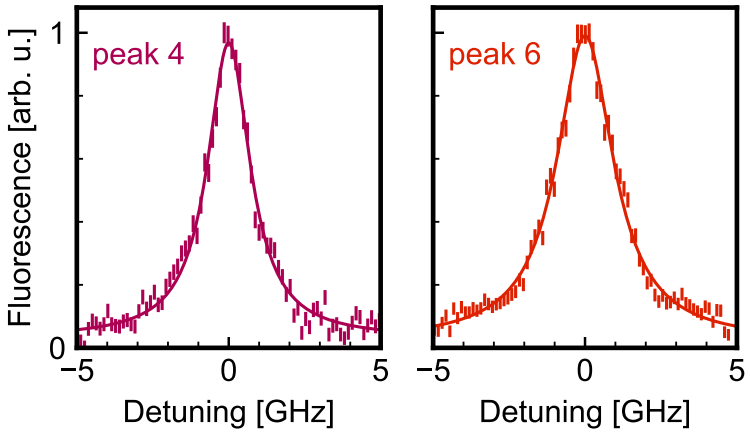

FIGURE 5.2: **Inhomogeneous linewidth.** Two high-resolution scans of peaks 4 and 6 are shown. Inhomogeneous linewidths of Γ_{inh} = 1.72(3) GHz and Γ_{inh} = 2.39(4) GHz are extracted using Lorentzian functions for fitting.

on erbium-implanted silicon [50]. But the values are comparable to MBE grown Er^{3+}:Si were optical linewidths of 1.9 to 2.4 GHz have been reported [79, 70]. Such narrow resonances indicate that the used implantation and fabrication procedure generates dopant integration at well-defined lattice sites and shows that the implantation and annealing procedure does not substantially damage the crystal structure, which would lead to a larger inhomogeneous broadening. Similar to other host crystals, the remaining inhomogeneous broadening is attributed to random strain fields in the waveguide caused by the different thermal expansion coefficients of Si and SiO_2. Additionally the considerable amount of oxygen, carbon, boron, and other impurities in commercial silicon-on-insulator wafers as well as the mixed isotopic composition of both crystal and dopants contribute to Γ_{inh}. It is expected that similar to other dopants and emitters in silicon, these sources of inhomogeneity can be reduced in optimized samples as I will show for the following sample generations. The inhomogeneous linewidths of all found fluorescence lines are documented in appendix B.2 and in Fig. 5.7 at the end of this chapter.

5.3 Optical lifetime

In Fig. 5.3 the optical lifetime decay of the two prominent peaks 4 and 6 is shown. This data is taken by recording the temporal decay of the fluorescence after the excitation laser is switched off. The data is fit using a single exponential function which allows one to determine a decay time of ~ 1 ms for the two brightest peaks shown in Fig. 5.1. Compared to other established host materials for erbium the excited state lifetime is reduced by about an order of magnitude [49]. The nonetheless long lifetimes are due to transitions between the 4f shells of rare-earth ions in sites of high symmetry, which are forbidden by parity. The lifetimes reported on similar sites in [117] are roughly by a factor of two smaller. The actual reason for that is unclear and might be connected to the large differences in sample preparation involving the mentioned

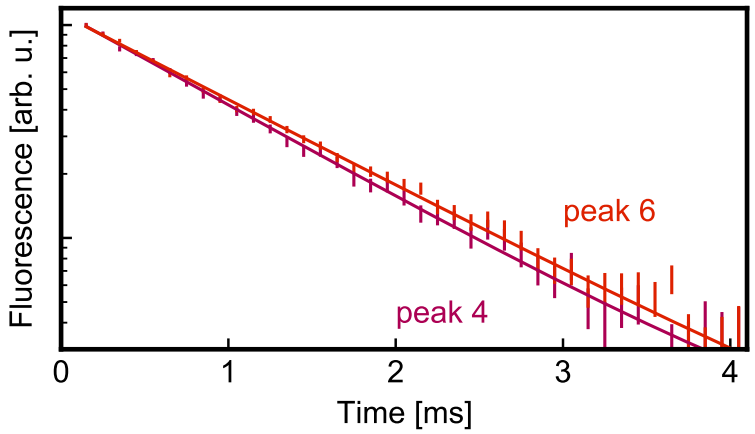

FIGURE 5.3: **Optical lifetime.** The optical lifetime of peaks 4 and 6 is plotted. A single exponential fit yields lifetimes of 0.936(2) and 0.978(3) ms, respectively.

co-implantation with oxygen. In general, the optical lifetime is small compared to the ones in other rare-earth doped crystals where lifetimes on the order of tens of milliseconds are common. This points towards potentially enhanced light-matter interaction strength. It is unclear if magnetic dipole interactions are responsible for the major part of this decay as their expected lifetime in silicon is around 2.5 ms[118]. Since a smaller optical lifetime is observed here, it seems likely that the lifetime is determined by electric dipole transitions. The extracted decays of all lines found are summarized in table B.2 in appendix B.2 and in Fig. 5.7 at the end of this chapter.

5.4 Homogeneous linewidth

The standard tool for measuring Γ_h is the 2-pulse photon echo technique. A $\pi/2$-pulse, followed by a π-pulse causes the dephased atomic superposition to be flipped, and then rephased, resulting in a strong emission peak called photon echo. This technique has been used to investigate various rare-earth doped crystals [55, 56] and waveguides [119].
However, I did not manage to measure a photon echo with this sample in this setup. There seem to be several obstacles preventing successful measurements using this technique: First, a transmission setup geometry is needed due to wave vector conservation [120] where the photon echo is emitted with the same **k**-vector as the π- and $\pi/2$-pulse. But since the waveguides are terminated with a broadband reflector still some echo should be reflected back into the tapered fiber. Second, I do only have a very dilute ion ensemble in the 400 µm long waveguide with considerable losses and thus only a small number of ions contributing to the coherent signal. An emitted echo might disappear in the noise due to the waveguides' sidewall roughness. However, these two possibilities are excluded in the upcoming sample generations where despite using low-loss waveguides in a transmission geometry no photon echo is detected. A third possibility, are the strong optical excitation pulses which are creating charges that spoil the coherence preventing the emission of a photon echo. However, despite efforts in finding a suitable set of pulse parameters and reducing the pulse power no photon echo was measured in Er^{3+}:Si here.

Instead a new method for measuring Γ_h is presented here based on transient spectral hole burning [49, 121]. A sketch illustrating the working principle is shown in Fig. 5.4.

The measurement technique is based on the observation that the fluorescence signal S increases non-linearly with the laser intensity I applied at a single frequency, because of saturation effects. Therefore, three laser fields of about the same intensity I are applied, generated with equidistant frequency separation within the inhomogeneous linewidth. This is achieved by modulating the input laser field with a single electro-optical modulator (EOM) which is illustrated in Fig. 5.4 a). The power-broadened, homogeneous linewidth Γ_h resides within the inhomogeneously

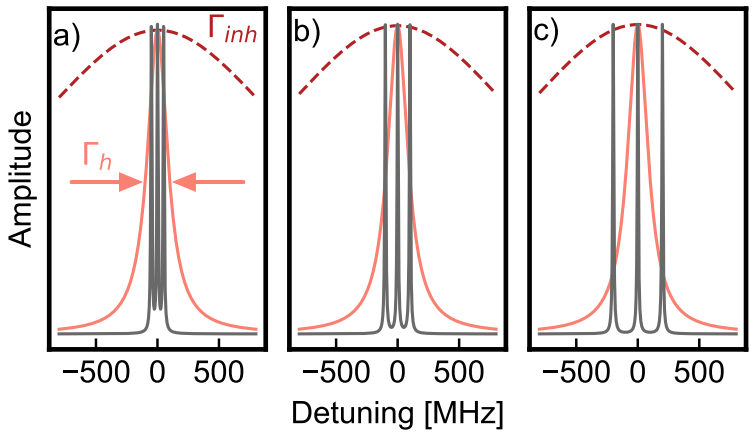

FIGURE 5.4: **EOM measurement scheme.** In a) three laser fields (grey) with equal amplitudes are generated and centered within the inhomogeneous lines (red dashed). By scanning the laser line separation, as illustrated in b) and c), an upper bound on the power-broadened homogeneous linewidth Γ_h (orange solid line) is extracted by monitoring the fluorescence signal as a function of the sideband detuning.

broadened ensemble Γ_{inh} and three slightly detuned laser fields are applied at almost zero detuning i.e. the center of the homogeneous line. The laser linewidth must be small compared to Γ_h, which is here ~ 1 MHz. As a next step, the separation of the three laser fields is scanned as shown in b) and c). This is done by modulating the rf frequency driving the EOM. Here, the separation of the first-order lines is equal to the rf driving frequency of the EOM. If the detuning of the three laser lines is small, or zero, the fluorescence will only increase by a factor of about $\sqrt{3}$ as only the ions centered in the homogeneous line contribute to the fluorescence signal and are saturated. If, however, the separation of the three laser lines is large compared to the homogeneous linewidth of the ions, irradiating the ions will increase the fluorescence threefold compared to that of a single field as indicated in c). Thus, by scanning the modulation frequency, I can measure an upper bound to the homogeneous linewidth of the excited erbium dopants on the timescale of their radiative lifetime when using excitation pulses of 1 ms duration. Again, to preclude detrimental effects of persistent spectral hole burning, the laser frequency is changed by a few megahertz between repetitions of the experiment. Additionally, as the measured value for Γ_h depends on the laser linewidth, the latter must be smaller compared to the scanned separation. In Fig. 5.5 I show the measurement traces for the two brightest peaks 4 and 6.
Here, the fluorescence signal on the y-axis as a function of the EOM modulation frequency on the x-axis is shown. For small detuning the laser is saturating the ions within the homogeneous line. For increasing modulation frequencies also the fluorescence signal is increasing non-linearly as less ions are saturated. For a modulation frequency of around 150 MHz the saturation is minimal and fluorescence signal exhibits the largest amplitude. Inverted Lorentzian functions are used to fit the data revealing spectral hole linewidths between 45 and 110 MHz for the individual sites.

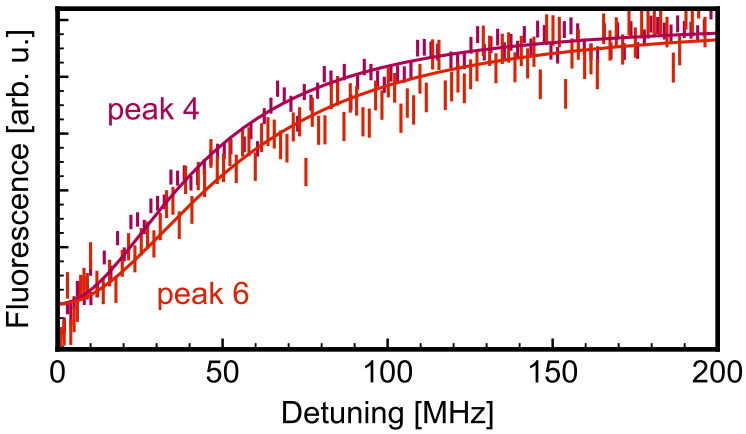

FIGURE 5.5: **Transient spectral hole linewidth.** The fluorescence dependence of peaks 4 and 6 as a function of the EOM detuning is shown. The data is normalized for better visibility. For small detunings only a small increase in signal is visible. For larger detunings, the fluorescence amplitude increases significantly. An inverse Lorentzian fit is used for extracting the linewidth of the spectral hole.

Typically, the measured upper bound to the homogeneous linewidth is given by half the width of the transient holes [122] which yields $\Gamma_h = 22.5\,\text{MHz}$ and $\Gamma_h = 55\,\text{MHz}$, respectively. The observed values here are much larger compared to other hosts [49]. This is mainly due to the power-broadening of the homogeneous line, inherently given by the measurement technique. When increasing the pulse power the linewidth broadens. Therefore when reducing the pulse intensity I expect also the measured homogeneous linewidth to decrease. However, in this setup, power reduction leads to very low count rates and large error bars. The small signal-to-noise ratio and the partly large uncertainties in the measured linewidth prompted me to discontinue measurements in this configuration. Apart from power broadening I also expect several more contributions to the broadening of the homogeneous linewidth. This includes dipolar interactions with neighboring magnetic moments in the crystal, crystalline defects, the proximity to interfaces, and TPA induced free carriers in the waveguide during excitation [123]. In this experiment the laser linewidth was $\sim 1\,\text{MHz}$, i.e. significantly smaller than the tens of MHz measured for Γ_h. As I will see for the upcoming sample generations, power broadening is the dominant mechanism for the observed homogeneous linewidths. In table B.3 in appendix B.2 and in Fig. 5.7 the extracted values of Γ_h for all observed sites are summarized.

5.5 Zeeman splitting

To gain insight into the spin manifold and the crystallographic structures of the sites found a magnetic field of 200 mT is applied oriented out-of-plane of the sample and the Zeeman splitting is investigated. Since erbium is a Kramers ion its spin degeneracy is lifted, increasing the number of spin-dependent optical transitions.

Typically, the probability of a spin-preserving transition is larger than that of a spin-flip transition. For example, in Er:YSO, at most magnetic field orientations the spin-preserving transition is nine times stronger compared to the spin-flip transition [124], which manifests itself in larger fluorescence emission rates. For a single Er^{3+} dopant occupying a site with cubic symmetry, the optical transitions will split into at least four separate lines. For sites of lower symmetries or hyperfine levels of ^{167}Er even more lines are expected.

Fig. 5.6 shows the Zeeman splitting in the fluorescence signal for sites 4 and 6, respectively. For site 4 I count twelve and for site 6 six peaks. The symmetry of both datasets is quite different. For site 4, eight large amplitude peaks centered around zero detuning are identified and four smaller ones at ±20 and ±30 GHz. In contrast, for site 6 the two main peaks are centered and accompanied by two small peaks at ±10 GHz. I attribute the larger peaks to spin-preserving transitions and the smaller ones to spin-flipping transitions. The splitting of the outermost lines of both spin-flip and the spin-preserving transitions is on the order of 20 GHz indicating

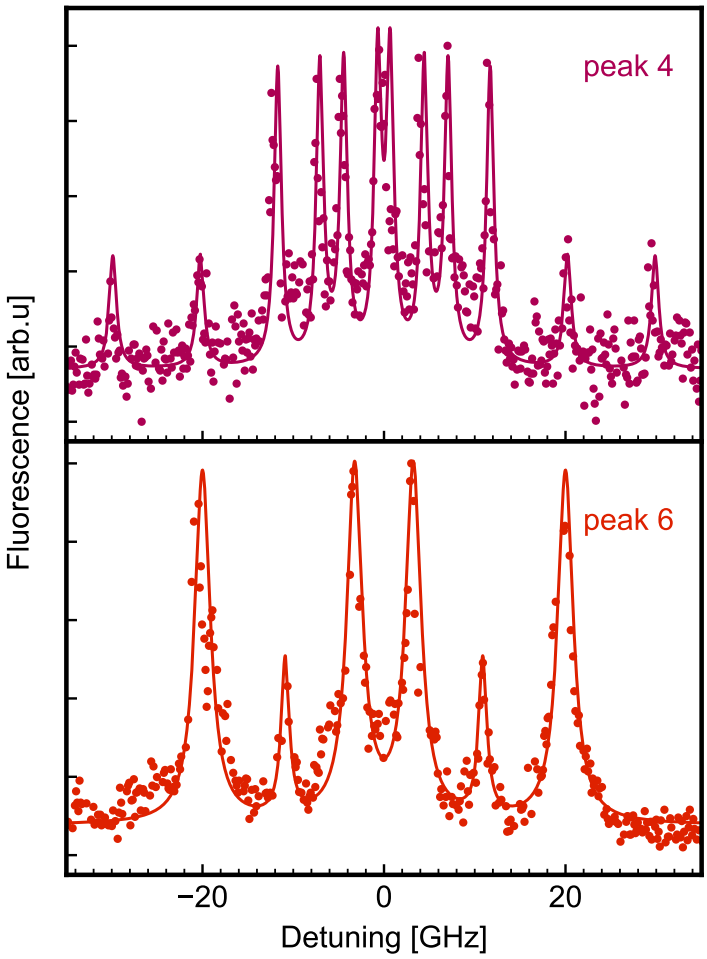

FIGURE 5.6: **Zeeman splitted peaks 4 and 6.** The data points are fitted using multi-peak Lorentzian functions (solid lines) extracting linewidths smaller 1 GHz.

a difference between the effective g-factors of the ground- and excited state, on the order of $g \approx 10$. The Zeeman split lines exhibit sub-gigahertz broadening determined using Lorentzian fits. The extracted values for all nine sites are summarized in Fig. 5.7. An additional observation I made was the decreased signal strength and the resulting decreased signal-to-noise ratio when performing these measurements. This observation indicates potentially long spin lifetimes on the order of several tens of milliseconds as the population is pumped into the different spin levels with long lifetimes.
The different overall shape of the Zeeman splitting indicates low site symmetries. From this I conclude that the sites found are not cubic sites but ones with lower symmetry due to the overall number of sharp lines. The same holds for the other peaks where I find different Zeeman-splitting patterns. A complete analysis of the site symmetry would require rotating the sample in a magnetic field allowing for extracting the complete g-tensor [125]. However, the current experimental setup is not capable of rotating the sample in the magnetic field thus this task is skipped here. The remaining sites are also investigated and I find a variety of patterns when applying a magnetic field which are documented in [43].

5.6 Summary

In summary, I have introduced a novel material system for quantum technology by integrating ensembles of erbium dopants into silicon nanophotonic waveguides. The low doping concentration in combination with an increased optical depth allows one to measure narrow fluorescence lines at telecom wavelengths. The resonant spectroscopy setup is sensitive to all erbium dopants, not only the ones connected to the conduction band, a key difference compared to all previous work on Er^{3+}:Si. I measure inhomogeneous linewidths of a few GHz. The observed optical lifetime is shorter compared to other erbium-doped crystals. This might be related to local field effects reducing the radiative lifetime of the erbium ions due to the large refractive index of silicon [126]. In addition, a new technique for estimating the homogeneous linewidth Γ_h is introduced. This technique allows for upper bounding the power-broadened Γ_h to a few tens of megahertz. Finally, the Zeeman splitting of the fluorescence lines is investigated where I find evidence of complex site geometries and potentially long spin lifetimes. All measured optical properties for the nine sites found are summarized in Fig. 5.7.

However, there are still many open questions and tasks to investigate in the next generation of Er^{3+}:Si samples. First of all, the fluorescence signal from the waveguide embedded erbium ions needs to be increased. This can be done by using longer waveguides and optimizing the etching recipe to minimize scattering loss due to the etched waveguide sidewalls or choosing another waveguide geometry. The annealing temperature seems to have a significant effect on the waveguide performance:

On the one hand, if no annealing step is performed, the waveguide losses are huge due to the implantation damage, and no fluorescence is detected. On the other hand, for an annealing temperature of 700 °C already a large number of sites come into existence. This points to already clustered erbium-related defects. A better understanding of the effect of post-implantation annealing on erbium sites in silicon is thus required. Related to the clustering issue is the choice of the silicon substrate. Czochralski grown wafers contain oxygen, and chemo-mechanical polishing and nano-fabrication can induce hydrogen and other elements that can form clusters with erbium. This can be avoided by using high-purity silicon. On the setup side, the EOM technique for estimating the homogeneous linewidth can be improved by probing several sub-ensembles at the same time increasing the signal-to-noise ratio and gain a better understanding of the power broadening and the temperature dependence of the homogeneous linewidth.
These questions are addressed in the upcoming chapters 6 and 7.

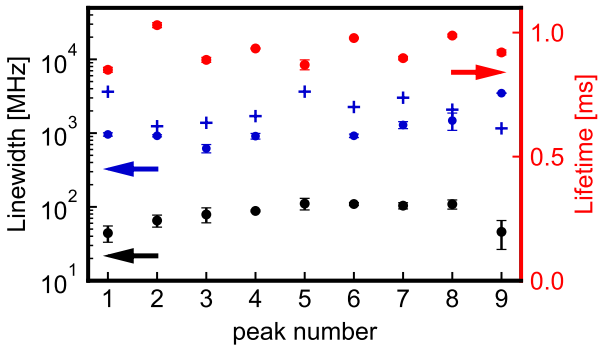

FIGURE 5.7: **Optical properties of the CZ sites.** The fluorescence lifetime (red), transient spectral hole linewidth (black), and inhomogeneous broadening (blue) with (dots) and without (crosses) magnetic field for all observed site is shown.

Chapter 6

Narrow optical transitions in erbium-implanted silicon waveguides

In this chapter, I present experiments performed on the second generation of Er^{3+}:Si samples. Again very narrow fluorescence lines appear in the experiment but at different wavelengths compared to the first sample generation. The 100-fold improved signal-to-noise ratio allows one to investigate the erbium sites' crystal field splitting and the optical lifetime modification due to the waveguide geometry. Furthermore, the EOM technique for estimating the homogeneous linewidth is improved reaching values close to the erbium lifetime limit. Additionally, tilted magnetic field measurements give some insights into the erbium sites g-tensors' anisotropy suggesting a low site symmetry. Finally, progress towards spin pumping in Er^{3+}:Si and quantifying the spin lifetime is discussed. This work has been published in parts in [44].

6.1 Sample specifications

For improved optical transitions with low inhomogeneous broadening, one needs to ensure a single-crystalline crystal with a low concentration of defects and impurities. Standard silicon-on-insulator (SOI) wafer fabrication involves detrimental techniques such as ion implantation and chemo-mechanical polishing which introduce impurities into the silicon [123]. For this reason, I present an approach for high-purity silicon-on-insulator.

CVD silicon on insulator

Here, a novel approach to obtaining high-purity crystalline silicon layers is implemented. The procedure starts with a commercial, slightly p-doped (R = 1-20 Ω·cm) SOI wafer which is thinned down to 0.05 µm. By heating the SOI chip to ~ 1100 °C for 1 min the top few nanometers of the device layer silicon are evaporated, providing a clean substrate surface. Afterwards, a layer of 0.14 µm thick epitaxial layer of silicon with natural isotope abundance is grown by chemical vapor deposition (CVD) at

Lawrence Semiconductor Research Laboratory, resulting in an overall device layer thickness of 0.19 µm. The CVD wafers are then implanted with both ^{167}Er and ^{170}Er in a two-step process using 0.1 MeV and 0.35 MeV acceleration voltage, respectively. The two implantation steps yield a homogeneous erbium dopant concentration profile of both erbium isotopes in the device layer. The dose was $2.9 \cdot 10^{12}$ cm^{-2} yielding a concentration of $\sim 10^{17}$cm^{-3}. Both concentration and implantation profiles are confirmed by SIMS measurements. The abundance of oxygen and carbon in the CVD grown silicon layer was also measured and is documented together with the erbium implantation profiles in appendix B.4. In addition to the isotope-selective implantation, the silicon substrates' temperature during the process was set to 500 °C. This temperature was chosen in order to directly anneal the implantation damage while preventing excess erbium segregation [127]. The wafers are then diced into 10x10 mm chips and ridge waveguides with lengths ranging from a few 10 µm up to several millimeters are fabricated. In the first sample generation, the waveguide lengths were limited to a few hundred micrometers due to the large waveguides' sidewall roughness induced by the reactive ion etching process. A newly developed cryogenic etching recipe reduces the etching-induced losses making the use of millimeter-long waveguides worthwhile. The key step of this recipe is cooling of the sample to −100 °C inside the RIE chamber before using SF_6 etching chemistry. The results are a significantly reduced sidewall roughness and high aspect ratios in the silicon samples [128] reducing the transmission losses and thus enhancing the optical depth.

Waveguide losses

As a result of the improved etching recipe, the waveguide propagation loss can now be estimated. To that end, several waveguides with different lengths are fabricated on a single chip. Then, the reflected fraction of laser intensity I is measured in a test setup at room temperature.
The ratio between in- and out-coupled light is related to the propagation loss constant α by:

$$\frac{I_{\text{out}}}{I_{\text{in}}} = R\eta^2 \mathrm{e}^{-2\alpha \mathrm{L}} \tag{6.1}$$

where η is the fiber-to-chip coupling efficiency, R is the reflectivity of the photonic-crystal mirror and L is the length of the waveguide. Both η and R are prone to fabrication imperfections, therefore the reflection of several waveguides of the same length is measured. Only the one with the highest reflectivity of each set is used for further analysis. Additionally, the reflectivity is averaged over the lasers' accessible frequency range. The obtained loss coefficients of both erbium-doped and undoped silicon waveguides are shown in Fig. 6.1. The figure shows the obtained waveguide reflectivities as a function of the optical travel length. The latter corresponds to twice the waveguide length taking into account the measurement setup geometry.

A fit yields $\alpha = 5.7 \pm 1.2\,\mathrm{dB/cm}$ for the Er^{3+}:Si sample. For comparison, using the same nanofabrication recipe, I also evaluated waveguides on an undoped SOI chip. There a lightly smaller decay constant of $\alpha = 3.5 \pm 1.2\,\mathrm{dB/cm}$ is found.
As a second loss characterization, ring-resonators on the Er^{3+}:Si chips are fabricated resulting in resonant modes with a Q-factor of $\sim 10^5$ for a round-trip length of 70 µm. From that, following [129], I can estimate an upper limit of 8(1) dB/cm, a result which agrees within experimental error with the previously obtained loss coefficients. The slight increase of the propagation loss in the implanted samples may be caused by residual crystal damage from the implantation process, and may thus be further reduced in samples with optimized implantation conditions.
In practical applications, ridge waveguide propagation losses of $\sim 1\,\mathrm{dB/cm}$ are common [130] which corresponds to a sidewall roughness on the order of $\sim 1\,\mathrm{nm}$ [123]. The loss might be further mitigated by cladding the waveguide in SiO_2 and fine tuning of the cryogenic etching recipe.

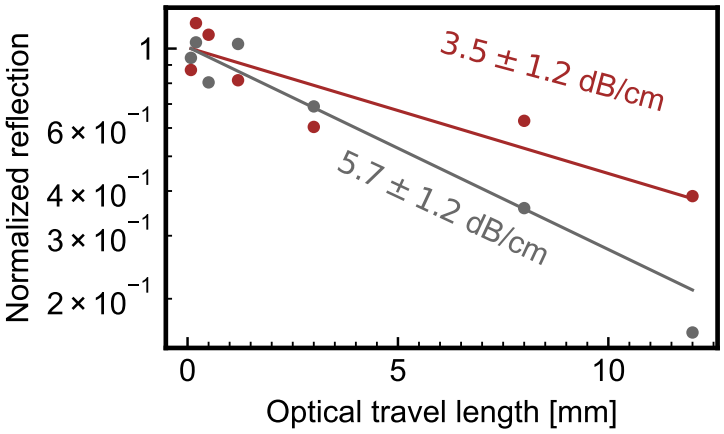

FIGURE 6.1: **Waveguide propagation loss.** Measurement of the reflectivity for different waveguides lengths in units of optical travel lengths in an undoped (red dots) and an erbium doped waveguide (gray dots). An exponential fit yields loss coefficients of $\alpha = 5.7 \pm 1.2\,\mathrm{dB/cm}$ (gray solid line) and $\alpha = 3.5 \pm 1.2\,\mathrm{dB/cm}$ (red solid line), respectively.

6.2 Resonant spectroscopy

I now turn to the spectroscopy part. Fig. 6.2 shows a typical fluorescence spectrum of a CVD Er^{3+}:Si sample revealing sharp optical fluorescence resonances. To achieve a strong signal, several millimeter-long waveguides, coupled to a tapered single-mode optical fiber with a one-way coupling efficiency of up to $\sim 20\%$ were used. The sample is cooled to cryogenic temperatures below 2 K. Excitation pulses of 500 µs duration and 2 µW power in the fiber towards the sample were applied here where both parameters are extracted from saturation measurements maximizing the signal-to-noise ratio on the largest peak in the spectrum.

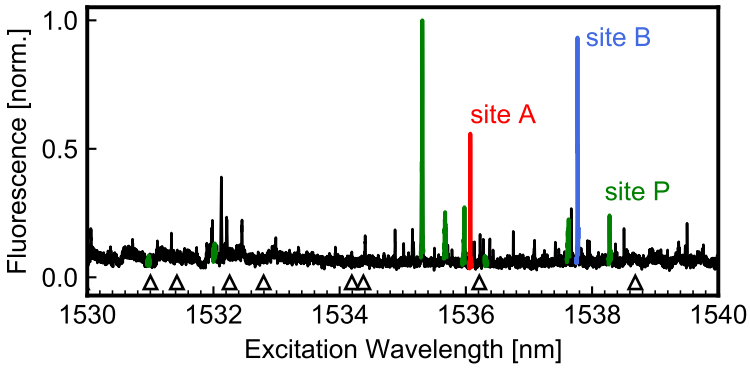

FIGURE 6.2: **Resonant spectrum CVD Er^{3+}:Si .** The laser wavelength is scanned while monitoring the erbium fluorescence after each laser pulse. Several narrow features appear whose wavelength does not coincide with the previously found ones, indicated by the black triangles. The color coding represents the two major prominent sites including some of the excited crystal fields levels of site *P*.

A large number of narrow fluorescence lines appear which are distributed in the wavelength range from 1530 – 1540 nm similar to the work presented in the previous chapter. However, their positions are different as indicated by the black markers positioned at the resonances found in the previous sample generation. Some minor peaks seem to be close to the previously identified sites but for other positions no match is visible. I can exclude strain effects, as this would have a smaller effect on the resonance position [131]. This suggests that owing to the changed sample preparation technique, erbium is integrated at different sites in the high-purity crystalline layer studied here. In particular, three major sites highlighted in Fig. 6.2 can be identified. They are located at 1536.07 nm (red), 1537.78 nm (blue) and 1538.27 nm (green). I restrict the further analysis to these three sites for most parts of this chapter. The 1536.07 nm fluorescence line is labeled as site *A* and the 1537.78 nm fluorescence line is labeled as site *B*. The line at 1538.27 nm will be referred to as site *P*. Fig. 6.2 shows an increased background level as the baseline of the spectrum does not concur with the expected dark count rate of the detectors. I attribute this slowly decaying background to a so-called "optically active site". These kinds of sites can be excited by electrons in the conduction band, potentially due to their close proximity to the conduction band edge. Therefore fluorescence of this site occurs independently of the excitation wavelength provided the power is large enough. The electrons can for example be transferred into the conduction band by a two-photon absorption mechanism. The optical background and its properties will be discussed later in this chapter.

6.3 Crystal field analysis

Due to the improved signal-to-noise ratio I am now able to measure the crystal field (CF) splitting of the three main sites *A*, *B* and *P*. To that end, a grating-based,

tunable filter is placed into the detection path. This filter has a bandwidth of 0.11 nm (FHWM) and a wavelength resolution of 0.01 nm. This allows for distinguishing the emission from different energy levels inside the ground and excited state crystal field manifolds.

Excited state crystal field

In the first experiment, the filter is kept resonant with the main sites in the above spectrum. Then the excitation laser is tuned to shorter wavelengths while monitoring the fluorescence passing through the filter on the respective fluorescence line. The upper and center plot in Fig. 6.3 thus reflect the crystal levels in the optically excited state manifold for the two main sites A and B with sharp resonances.

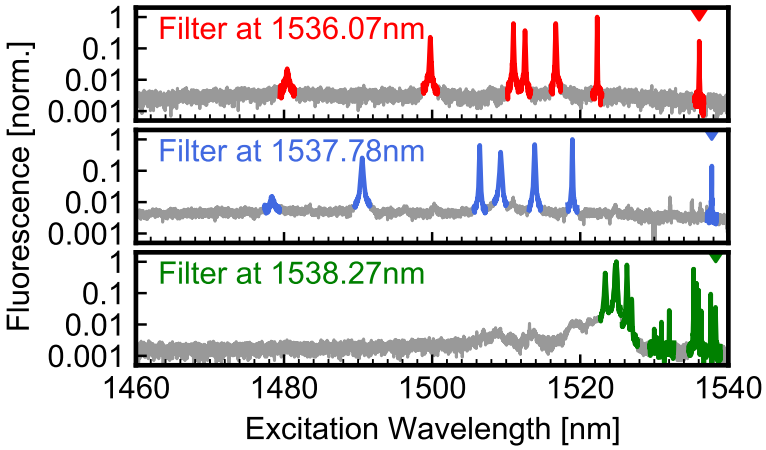

FIGURE 6.3: **Excited CF manifold.** The filter is placed at the wavelength given in the graphs. Seven levels can be identified in the excited crystal field manifold for sites A and B while site P shows 14 resonances indicating a pair site.

In these measurements, the filter is placed in resonance with the respective site as indicated by the markers in Fig. 6.3. The laser wavelength is then tuned while monitoring the fluorescence that is transmitted through the narrowband filter which allows for assigning the excited state crystal field levels Y_i.
The separation between the crystal fields is on the order of several nanometers, similar to other erbium-doped materials. I find a total number of seven excited state crystal field levels for sites A and B which is expected for single erbium dopants in low-symmetry sites without magnetic field [49]. The splitting between the lowest two crystal field levels in both ground and excited state is considerably larger than in other investigated erbium hosts which in combination with silicons' high Debye temperature can improve the optical coherence at higher temperature [132]. I will come back to this feature later in this chapter. For site P, however, the splitting is different: I can identify a total number of 14 fluorescence lines which is twice as much as for one of the main sites and the level separation is much smaller compared to sites A and B. I conclude that site P is comprised of at least two erbium atoms forming a pair- or precipitate site - hence its label: site P.

In addition to the crystal fields, the branching ratio, i.e. the fraction of photons emitted at the transition between the lowest crystal fields in the ground and excited state manifold can be measured. By splitting the fluorescence light into a filtered and an unfiltered optical path with the calibrated relative transmission, I can compare the fraction of light emitted at the $Y_1 \rightarrow Z_1$ transition to the overall number of emitted photons. This experiment uses a fiber-Fabry-Pérot based, tunable filter (MicronOptics FFP-TF). In contrast to the grating based filter, this tool is not polarization-dependent and thus insensitive to photons of different polarization. Upon comparing the fraction of light in the filtered path compared to the unfiltered one a branching ratio of 20(5)% is measured for the two main sites. This value is comparable to other erbium-doped materials [48, 133, 125]. The uncertainty reflects the estimated wavelength-dependent loss at the photonic crystal mirror and the fiber-to-chip coupling.

Ground state crystal field

For measuring the ground-state crystal field splitting the laser frequency is fixed and the filter is instead tuned towards larger wavelengths, as shown in Fig. 6.4. Here, the $Z_1 \rightarrow Y_2$ transition is excited to determine the ground state crystal field splitting. At cryogenic temperatures, fluorescence occurs primarily from $Y_1 \rightarrow Z_n$, regardless of which Y level is excited, because of rapid non-radiative relaxation to Y_1 inside the excited state crystal field manifold [70, 125]. We chose Y_2 because a better signal-to-noise ratio is observed in these experiments when monitoring the emission. The filter is scanned from 1530 nm to 1600 nm limited by its wavelength tuning range.

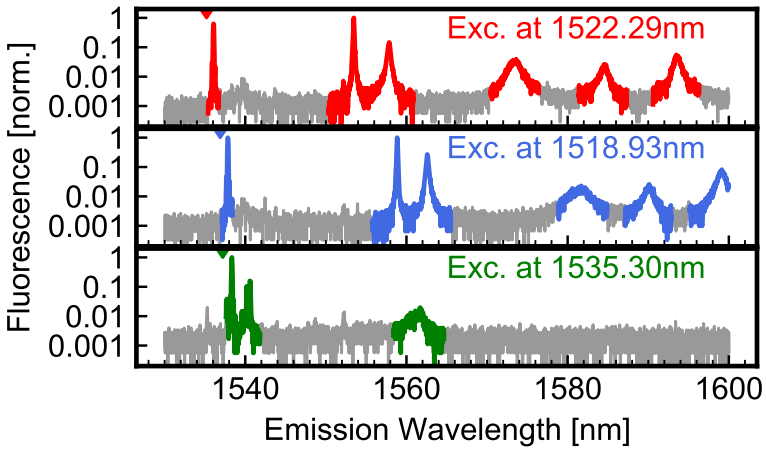

FIGURE 6.4: **Ground state CF manifold.** The ground state CF positions are extracted by fixing the laser frequency and scanning the filter. For sites A and B six levels can be identified. This suggests, that the seventh and eighth level are located beyond 1600 nm and not within reach of the current filter. For site P only a fraction of the expected 14 levels is found.

For sites A and B six levels can be identified where the one around 1600 nm of site B is cut off. Actually, two additional levels would be expected here. They might be

located beyond the tuning range of the filter or overlapping with another CF and thus can not be resolved here. For site P, only a few of the expected 14 levels are visible. In both ground and excited crystal field manifolds, the energy levels have a smaller spacing compared to sites A and B. This small energy spacing cannot be resolved with the current filter due to its finite wavelength resolution of 0.01 nm. In addition, some peaks might have potentially small amplitude which would be hidden in the noise. The broadening of the long-wavelength peaks can be attributed to fast phononic relaxation of the upper crystal field levels, as commonly observed with rare-earth doped crystals [49].

Crystal-field energy levels

The fluorescence line positions from both data sets of the ground and excited state crystal field manifolds of sites A and B are summarized in table 6.1. Their position is determined by fitting Lorentzian curves and extracting the respective fit position. Their energies are expressed using the standard spectroscopy notation of inverse centimeters.

Term	CF level	site A	site B
$^4I_{13/2}$	Y_7	6754.7 cm^{-1}	6764.1 cm^{-1}
	Y_6	6667.6 cm^{-1}	6708.8 cm^{-1}
	Y_5	6618.1 cm^{-1}	6638.1 cm^{-1}
	Y_4	6611.3 cm^{-1}	6625.7 cm^{-1}
	Y_3	6593.2 cm^{-1}	6605.6 cm^{-1}
	Y_2	6568.9 cm^{-1}	6583.5 cm^{-1}
	Y_1	6510.0 cm^{-1}	6502.8 cm^{-1}
$^4I_{15/2}$	Z_8	*not resolved*	*not resolved*
	Z_7	*not resolved*	*not resolved*
	Z_6	235.0 cm^{-1}	249.4 cm^{-1}
	Z_5	199.1 cm^{-1}	214.0 cm^{-1}
	Z_4	154.6 cm^{-1}	179.8 cm^{-1}
	Z_3	91.1 cm^{-1}	103.3 cm^{-1}
	Z_2	72.9 cm^{-1}	87.9 cm^{-1}
	Z_1	0 cm^{-1}	0 cm^{-1}

TABLE 6.1: **Crystal field energy levels sites *A* and *B*.** The energy levels are given in units of inverse centimeters. The levels Z_7 and Z_8 could not be resolved.

6.4 Inhomogeneous broadening

The three measured sites display narrow inhomogeneous lines. For a better frequency resolution, a frequency-stabilized laser is used for scanning the inhomogeneous linewidth of the three main sites addressed above.

These fine scans are shown in Fig. 6.5. All three sites show a double-peak structure

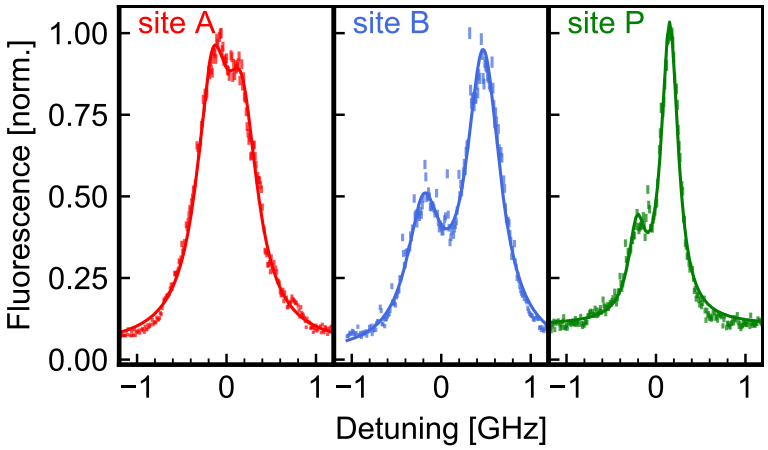

FIGURE 6.5: **Inhomogeneous linewidths.** The resonant fluorescence is recorded after the excitation laser is switched off. The observed lines are well fit by two Lorentzian functions with equal FWHM (solid lines), tentatively ascribed to the two implanted erbium isotopes.

with a separation of 0.36(1) GHz (site *A*), 0.65(1) GHz (site *B*) and 0.32(1) GHz (site *P*). Both ^{167}Er and ^{170}Er have been implanted with equal doses, which can be held responsible for the double-peak structure. This assumption is supported by a recent experiment in our group where no double-peak inhomogeneous lineshape was found in purely ^{170}Er implanted silicon. Another possible explanation for the double-peak structure is strain present in the silicon layer. After cladding the waveguide in silicon dioxide, a splitting of site *B* on the order of several gigahertz can be observed. Still, a final explanation of the origin of the observed double-peaks must be left open here. Each site is fit with a double Lorentzian function, yielding a full-width-at-half-maximum inhomogeneous linewidths of 0.44(1) GHz (site *A*), 0.40(1) GHz (site *B*), and 0.23(1) GHz(site *P*). Thus Γ_{inh} is reduced by over a factor of two compared to the previous sample generation. Again, the observation of such narrow resonances indicates dopant integration at well-defined lattice sites due to optimized substrates and the improved implantation technique. The remaining inhomogeneous broadening is attributed to random strain fields, which can be caused by the different thermal expansion coefficients of Si and SiO_2, by small residual amounts of oxygen and other impurities, and finally by the mixed isotopic composition of the crystal and the erbium implant itself.

6.5 Optical lifetime

In addition to the large crystal field splitting and the narrow inhomogeneous broadening, the sites discovered in this work have another advantage: They exhibit comparably fast optical transitions which will be discussed in this section.

Fluorescence decay

Fig. 6.6 shows the fluorescence decay after the excitation laser is switched off. In addition to the three main sites, also the lifetime of the slowly decaying background, colored in gray, is shown. A single-exponential fit yields a lifetime of around 2.47(6) ms. Similar values have been found in erbium-doped silicon before using off-resonant excitation [127]. This is detrimental for the purposes here as it imposes a long-lived background signal which reduced the signal-to-noise ratio in the experiment. Additional measurements reveal that the excitation of this background is largely independent of the excitation wavelength, but the emission can be both broad- and narrowband. A more detailed analysis of the background and the associated site *O* is given later in this chapter. I can effectively reduce the background contribution by using a narrowband filter for extracting the lifetimes of sites A, *B* and *P*. Site *P* features

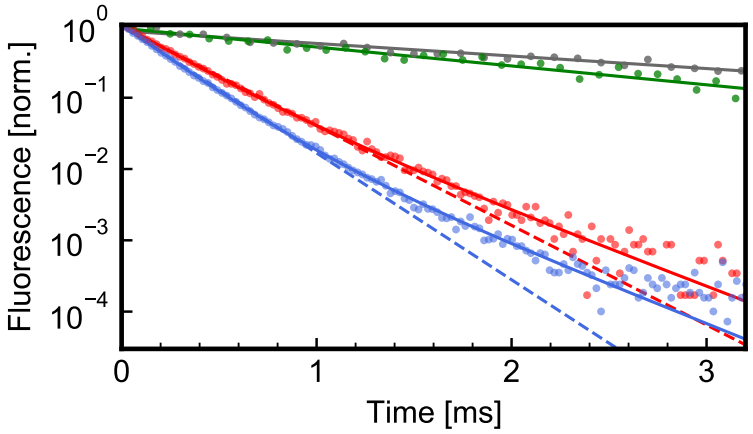

FIGURE 6.6: **Optical lifetimes.** The fluorescence decay is recorded after the excitation laser is switched off. The lifetimes of the three main sites are shown in addition to the long-lived (2.47(6) ms) optical background (grey). For sites *A* (red) and *B* (blue) a bi-exponential decay (solid lines) is in good agreement with the data whereas a single exponential curve (dashed line) deviates for times larger ~ 1 ms. Site *P* decays with a lifetime of 1.64(1) ms. Sites *A* and *B* decay with lifetimes of 0.311(1) ms and 0.244(1) ms, respectively.

a comparably long optical lifetime of 1.64(1) ms while sites *A* and *B* feature lifetimes of 0.311(1) ms and 0.244(1) ms, respectively. The measured decay for *A* and *B* is much faster compared to other erbium-doped systems like Er:YSO (11.44 ms) [54], Er:YVO (3.34 ms) [134] and Er:TiO_2 (5.52 ms) [125]. This large discrepancy might indicate that the erbium ions are located at interstitial sites, where the local-field correction factor in high refractive index materials, such as silicon, can facilitate an increased spontaneous emission rate [126].

In Fig. 6.6 a single-exponential curve (dashed lines) only captures the decay of sites *A* and *B* up to approximately one millisecond. The data deviates for longer times and is better described by a second exponential function. Thus an overall bi-exponential fit correctly describes the fluorescence decay which is also used for extracting the

above optical lifetimes. I attribute the bi-exponential decay to Purcell enhancement of the erbium ions inside the waveguide which I will explain in the following.

Lifetime modification by LDOS

To investigate the effect of the Purcell enhancement due to the waveguide geometry on the ion emission rate, FDTD simulations are performed to calculate the local density of states (LDOS) as described in chapter 3.3. The LDOS provides information on the spatial distribution of the Purcell factor F_p in the waveguide for different dipole emitter orientations, i.e. erbium ions [90]. A simulation of F_p for the ridge waveguide is shown in Fig. 6.7 a). The xy cross-section of a ridge waveguide (width $w = 700\,\text{nm}$

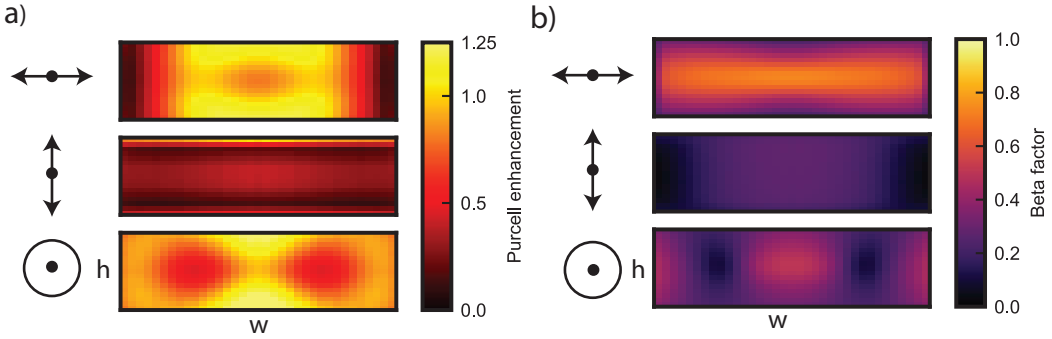

FIGURE 6.7: **Purcell and beta factors in ridge waveguide.** In a) the Purcell factor distribution inside the ridge waveguide cross-section ($h = 190\,\text{nm}$ and $w = 700\,\text{nm}$) is shown for three dipole emitter orientations. For the same waveguide geometry and dipole orientations the β-factor is shown in b). Both simulations were done by Stephan Rinner.

and height $h = 190\,\text{nm}$) with an infinite extend along the (propagation) z-axis for three different dipole emitter configurations is shown. The emitting direction is indicated by the arrows on the left-hand side of each panel. First, the LDOS for the waveguide geometry is calculated and normalized to a homogeneous silicon volume yielding F_p. The simulation is done three times for three different dipole emitter configurations as shown in the three, stacked panels. Each pixel corresponds to the calculated value of F_P of a dipole placed at that position. There are regions where $F_p > 1$, e.g., for the case of a horizontal dipole in the waveguide center. In the same panel, a Purcell factor $F_p \sim 1.2$ is indicating an enhanced emission surrounding the waveguide center. But for the case of vertically oriented dipoles, $F_p \sim 0.3$, which indicates suppression of emission. For a dipole oriented along the propagation direction in the bottom panel, the Purcell factor varies between 0.5 and 1.25.
In addition to the Purcell enhancement, also the β-factor is calculated, corresponding to the probability that a photon is emitted into a waveguide mode rather than into free space. This allows for weighting of the emission relative to the respective dipole orientation. Again an FDTD simulation is employed, where a dipole is placed in the waveguide and each pixel corresponds to β calculated for an emitter at that location within the waveguide. The fraction of power emitted into the waveguide is

normalized to the total emitted radiated power which then yields β. As can be seen in Fig. 6.7 b) also the β-factor depends on the dipole orientation of the emitter. For a horizontal dipole, the emission into the waveguide approaches unity but for a vertical dipole, less than 50% of the overall radiated power is emitted into a waveguide mode.

To model how the spatial distribution of the implanted erbium emitters affects the optical lifetime, a Monte Carlo simulation is carried out. A dopant position in the waveguide is randomly picked in line with the simulated implantation profile, and assigned a random, optical dipole orientation along one of the three directions, as indicated in Fig. 6.7. An initial decay time of 300 µs is attributed to each doping atom, which is subsequently weighted by the calculated LDOS and the β-factor. This procedure is repeated for 1000 arbitrary dopant positions. Finally, all these lifetime contributions are summed up and normalized with respect to the three dipole orientations. Fig. 6.8 shows the three curves for the three different dipole orientations, which are well fit by bi-exponential decay curves (solid lines). This qualitatively matches the measurements in Fig. 6.6 showing that for longer lifetimes a bi-exponential curve models the lifetime data more accurately than a single-exponential function (dashed lines). To obtain quantitative agreement, however, better control of the dopant profile, as well as information on the orientation and relative strength of the magnetic and electric dipoles is crucial. Still, I emphasize that for all dipole orientations, the decay obtained is slower than the radiative decay in a bulk sample (red dotted line). Thus, the obtained lifetime of the sites may be considered as an upper bound and should be reduced when using e.g. larger waveguide dimensions which will be discussed in chapter 7. I restrict the analysis here to electric-dipole transitions, assuming that they govern the emission in the fast-decaying erbium sites A and B [49]. However, I note that magnetic dipoles may also contribute to the measured signal as they exhibit a similar Purcell enhancement as electrical dipoles and thus give qualitatively similar results.

6.6 Homogeneous linewidth

I now turn to the investigation of the homogeneous linewidth. Here, a similar method as presented in section 5.4 but with a somewhat improved measurement scheme is used. The large fluorescence signal in the CVD samples in combination with the improved measurement scheme allows for a better understanding and a more thorough analysis of the homogeneous linewidth here.

Improved measurement scheme

As discussed in chapter 5 the technique for extracting the homogeneous linewidth is based on the observation that the fluorescence signal S increases non-linearly with laser intensity I applied at a single frequency. Because of saturation, an upper

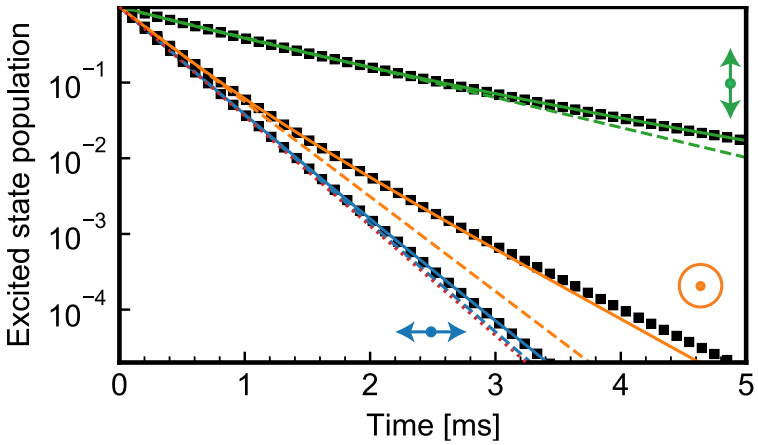

FIGURE 6.8: **Monte Carlo lifetime simulation.** The simulated decay of dipole emitters hosted along different orientations in the waveguide is shown here. A single-exponential function only describes the data within the first millisecond well. A bi-exponential fit is required to accurately describe the lifetime decay at longer times similar to what is observed in the measurements. Black squares are simulated data fitted by a single exponential function (dashed line) and a bi-exponential curve (solid line). This simulation has been performed by Stephan Rinner and Andreas Gritsch.

bound of the power broadened, homogeneous line can be extracted by scanning the separation of the three laser lines. The major advancement here is to perform this measurement simultaneously at several frequencies within the inhomogeneously broadened line, as sketched in Fig. 6.9. It is important to keep in mind that the inhomogeneous broadening Γ_{inh} is of the order of $\sim 500\,\text{MHz}$. This is considerably larger than the lifetime limited homogeneous linewidth Γ_{h} being of the order of $\sim 0.5\,\text{kHz}$. However, when using the presented measurement scheme the homogeneous linewidth is power broadened, a notorious disadvantage of this technique. Thus, the measured homogeneous linewidth will be larger compared to the theoretical value below 1 kHz and is describing an upper limit to Γ_{h}. Instead of performing the experiment at a single frequency within the inhomogeneously broadened ensemble (red dashed line), the experiment can be conducted at many frequencies, exciting several sub-ensembles within the inhomogeneous line as shown in Fig. 6.9 a). This increases the fluorescence signal by a factor of $3^3 = 27$, corresponding to the number of laser fields present when using three concatenated electro-optical modulators where each modulator generates two first-order sidebands in addition to the carrier. Thus, by using this many additional laser fields the signal-to-noise ratio is improved in contrast to experiments on the homogeneous linewidth in chapter 5. In Fig. 6.9 b) and c) the power-broadened homogeneous line can be estimated by scanning the laser line separation Δ. Note that in Fig. 6.9 only nine instead of 27 lines are shown for better visibility. If the detuning Δ of the laser fields is larger than the ensemble homogeneous linewidth, their simultaneous irradiation will lead to a 27-fold increase of the fluorescence compared to that of a single laser field. If, however, the detuning Δ is small, or zero, the fluorescence will only increase by a

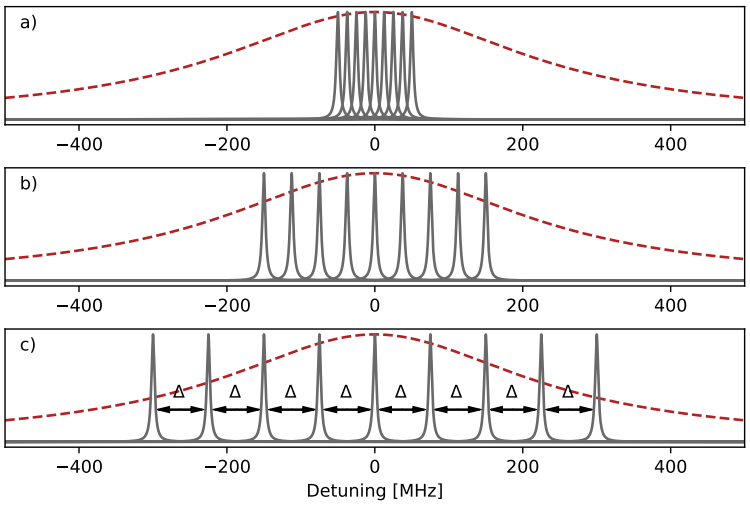

FIGURE 6.9: **Improved homogeneous linewidth measurement scheme.** a) The homogeneous linewidth is probed at several frequencies (grey lines) within the inhomogeneously broadened ensemble (red dashed line). b) - c) The peak separation Δ is increased yielding equidistant laser lines. For better visibility only nine lines are shown here.

factor of $\sqrt{27}$ owing to saturation. Here, excitation pulses of 0.15 ms duration are used and the laser line separation is scanned by variation of the rf signal driving the electro-optical modulators. The fluorescence is monitored in a 0.2 ms window after the laser is switched off. In addition, the laser frequency is shifted in between repetitions to mitigate the effects of persistent spectral hole burning. While this was done in the previous experiments using the built-in grating of the laser, here an additional acousto-optic modulator is used for that purpose.

Γ_h approaching the lifetime limit

Fig. 6.10 shows the homogeneous linewidth of sites A and B as a function of the light intensity in the waveguide. Again, the measured upper bound to the homogeneous linewidth is given by half the width of the transient holes [122]. The inset shows a typical measurement trace which is fit with an inverted Lorentzian curve corresponding to the lowest observed homogeneous linewidth of 9(3) kHz. This data corresponds to the red circled data point in the main panel.
When the modulation frequency is smaller than the linewidth of the sub-ensembles, saturation leads to a signal decrease (inset), which is well fit by Lorentzian curves (red solid) with FWHM down to 9(3) kHz for site B (blue), and 10(2) kHz for site A (red). This value is limited by the signal-to-noise ratio preventing measurements at even lower pulse powers. Instead, this measurement is repeated for larger pulse intensities I. This results in an increase of the linewidth with excitation pulse power (main panel), which follows a square-root dependence $\sqrt{I}$ (solid lines). The ensemble average value of the homogeneous linewidth is limited by power broadening and constituting an upper bound on Γ_h. By reducing the power even more, I expect that

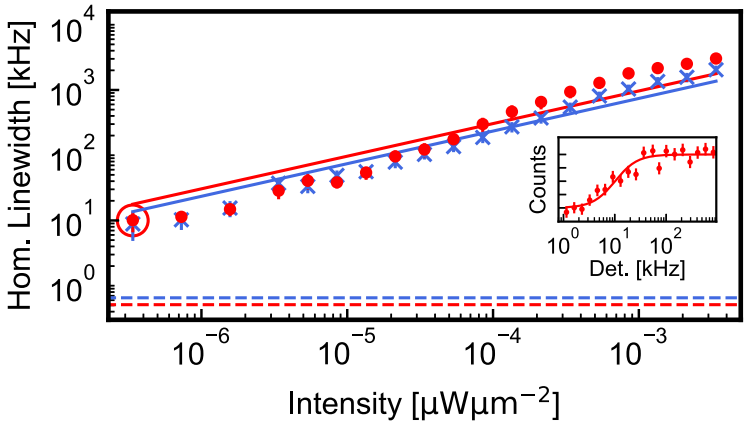

FIGURE 6.10: **Homogeneous linewidth.** The main panel shows the homogeneous linewidth as a function of the power in the waveguide for sites A and B. The solid lines indicate a power scaling $\sim \sqrt{I}$ and the dashed lines show the sites' respective lifetime limit. The inset shows the corresponding measurement trace of the circled data point in the main panel. An inverted Lorentzian fit (red solid) is used to extract the transient hole width.

the actual homogeneous linewidth is approaching the lifetime limit of ~ 0.5 kHz as indicated by the horizontal dashed lines for the main sites A and B. I point out here that the measured homogeneous linewidth is among the narrowest spectral features measured in nanostructured material so far [135].

6.7 Spin-lattice relaxation

When working with erbium emitters in silicon the interaction between the electron spin and the surrounding lattice is important to understand as these interaction limit the spin lifetime or spin relaxation time T_1. Typically, three phonon-involving processes contribute to the spin–lattice relaxation. The direct process, the Raman process and the Orbach process. A Raman-type relaxation mechanism is dominant when the Debye energy $k_B\Theta_D < \Delta$ leading to a $\sim T^9$ dependence of the relaxation time. Here k_B is the Boltzmann constant, Δ the crystal field splitting and Θ_D the Debye temperature. In contrast, the direct process linewidth scales linearly with temperature T [136]. In silicon the Debye temperature is 645 K [137] and thus larger compared to ionic rare-earth doped crystals. In addition, the ground and excited state crystal field splitting is on the order of ~ 1 THz. Therefore, the Orbach process is expected being the dominating spin-lattice mechanism in the material system here. In this type of relaxation mechanism, the relaxation time scales as $\sim \exp(\Delta/k_B\Theta_D)$ [138]. Fig. 6.11 shows the temperature dependence of the homogeneous linewidth as a function of the sample temperature for site B.

Same symbol data points correspond to same pulse powers resulting in a power-broadened homogeneous line for temperatures at 2 K. When increasing the temperature, the linewidth remains constant up to ~ 10 K before increasing at larger

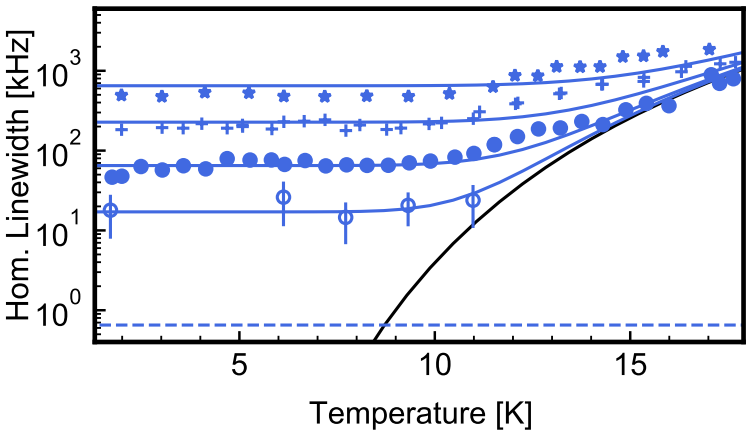

FIGURE 6.11: **Homogeneous linewidth dependence on temperature of site *B*.** The individual symbols corresponds to different pulse powers and the dashed blue line indicates the lifetime-limited linewidth. The increase in linewidth is well fit using Eq. (6.2) (blue solid lines) where the black line corresponds to an Orbach relaxation in the absence of power broadening.

temperatures. The data are fit using Eq. (6.2), a slightly adapted formula from [139] where I assume that the Orbach coefficient $A_{\text{Orb.}}$ is similar for all crystal fields.

$$\Gamma_{\text{Orb.}} = A_{\text{Orb.}} \sum_{\Delta_{ES},\Delta_{GS}} \frac{\Delta^3}{\exp\left(\frac{\Delta}{T}\right) - 1} \tag{6.2}$$

For several settings of the optical intensity, the temperature dependence is well fit by this formula (solid blue lines). The exponent is determined by the independently measured crystal field splittings Δ and the power-broadened linewidth remains a free fit parameter. Thus, an Orbach coefficient $A_{\text{Orb.}}$ of 0.17(6) $s^{-1}K^{-3}$ can be extracted. Fig. 6.12 shows the measurement data of sites *A* and *P* for a single power setpoint each. Similar to site *B*, also site *A* features a large average crystal splitting on the order of tens of nanometers in both ground and excited state as discussed in section 6.3. As the extracted Orbach coefficient $A_{\text{Orb.}} = 0.15(6)\ s^{-1}K^{-3}$ is quite similar for sites *A* and *B*, the coupling rate to phonons seems to be same for both main sites.
For site *P*, however, the crystal field splitting is much smaller, on average on the order of one nanometer or less. This leads to a significantly larger linewidth at low temperatures which increases further with rising temperature. Nevertheless, also for this site, the Orbach relaxation is still describing the behavior well as indicated by the solid green line. The temperature range up to 8 K is conveniently accessible with dry ^{4}He cryostats reducing the experimental overhead dramatically.

6.8 Optically active sites

The fluorescence of "optically active" sites can be excited by electrons in the conduction band. These sites were mentioned in section 6.5 when comparing the optical

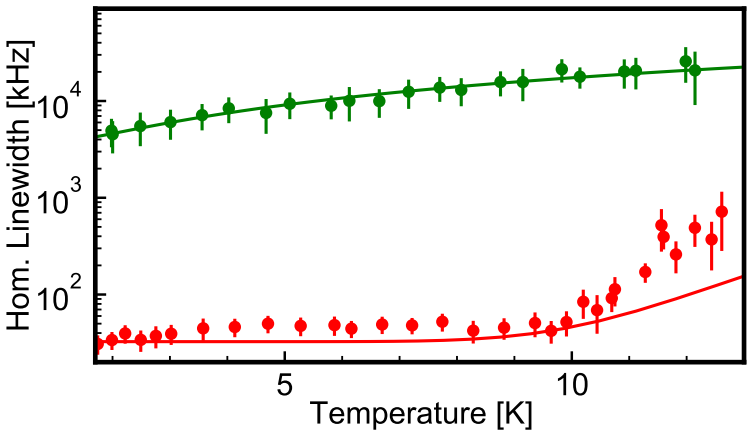

FIGURE 6.12: **Homogeneous linewidth dependence on temperature sites *A* and *P*.** The temperature dependence of the homogeneous linewidth of site *A* (red) and site *P* (green) is shown here. Both data sets are again fit with the Orbach relaxation function (solid lines) giving good agreement.

lifetimes of the different sites in Fig. 6.6 to the slowly decaying background. This

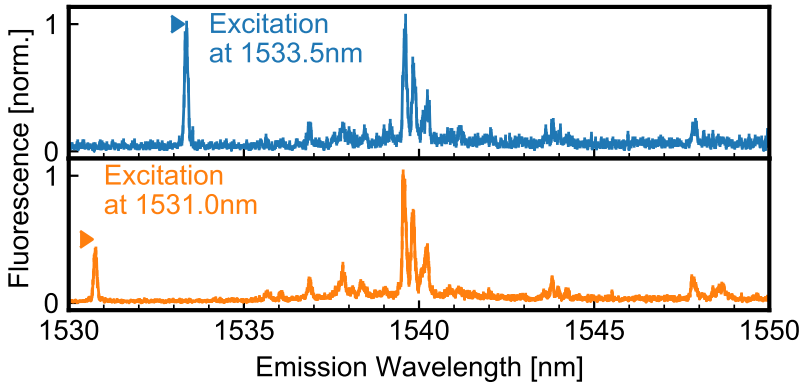

FIGURE 6.13: **Optically active site.** Measurement of the ground state splitting of one optically active site by scanning the filter revealing the ground state CF splitting. For two different excitation wavelengths, the same major fluorescence lines at around 1540 nm appear, revealing the sites' narrowband emission.

background exhibits a lifetime of 2.47(6) ms which is consistent with the expected lifetime of a purely magnetic dipole decay in a non-magnetic medium [118] and which has been already encountered in erbium-doped silicon [140, 80]. This background signal is present independently of the excitation wavelength between 1520 - 1540 nm.

However, during the measurements of the ground-state crystal field splitting it became clear that this background consists of multiple sources, i.e. different optically active sites. These sites can be excited independently of the main sites and can cause emission in a large frequency window. One of these sites is discussed in the following. The corresponding measurement is shown in Fig. 6.13. Here I perform two experiments where I excite at two different wavelengths, 1531.0 nm and 1533.5 nm,

which are far off-resonant to the sites A, B and P. I then scan the tunable filter, similar to the experiments shown in Fig. 6.4, and monitor the emitted fluorescence. There the same emission peaks appear for both excitation wavelengths showing the narrowband emission of this optically active site. In addition, when placing the filter on the highest peaks' position, an optical lifetime of ~ 0.7 ms is measured which is by a factor of three faster compared to the broadband background signal observed in Fig. 6.6. I note here, that the found optically active sites do not match the ones found in [50]. Judging from the two different decay lifetimes, 0.7 ms and 2.47 ms, I thus find at least two different optically active sites, which are both contributing to the overall background fluorescence signal being detrimental to the experiments. However, a narrowband filter can be used to largely eliminate the resulting background contribution.

6.9 Zeeman splitting

I now turn to the magnetic field dependence of the CVD Er^{3+}:Si samples. The improved signal-to-noise ratio allows for investigating the magnetic field-induced splitting on the main sites.

Magnetic field maps

Fig. 6.14 shows the Zeeman splitting of the sites A and B when applying a magnetic field perpendicular to the sample surface, i.e. along the [100] axis. The field is generated by a superconducting magnet mounted inside the cryostat. The measurement is performed by scanning the laser wavelength and monitoring the fluorescence at each wavelength setpoint after the laser is switched off. The fluorescence amplitude is indicated by the colorbar, normalized, and plotted on a logarithmic scale for better visibility. The magnetic field is gradually increased from 0 to 170 mT as displayed on the y-axis. The sample is kept at a temperature of 14 K to avoid effects of spin polarization. The latter would be detrimental to this measurement as the fluorescence signal would be dramatically reduced. At $B = 0$ mT the already known fluorescence lines are visible. In Fig. 6.14 a), site A is centered at 1536.069 nm. When increasing the magnetic field the site starts to fan out as a function of the magnetic field strength. Two different classes of lines can be identified: Bright lines, centered around site A which split by ~ 100 pm (orange markers) and darker lines with larger splitting (black markers). The bright lines correspond to spin-preserving transitions whereas the lighter ones correspond to spin-flip transitions. This is similar to the finding in the previous sample generation discussed in chapter 5.6. The different splitting suggests that the ground and excited states have different, anisotropic g-tensors. Assuming four different positions of the Er-site in the crystal lattice with two spin-preserving and spin-flip transitions each would yield a total of eight lines which are, however, not observed in Fig. 6.14. At 180 mT in total, six spin-preserving lines can be identified. The same holds for the spin-flip transitions where four lines are

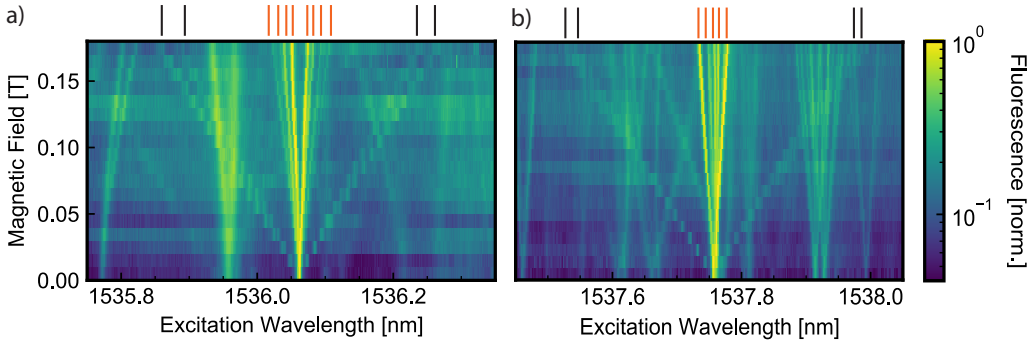

FIGURE 6.14: **Magnetic field maps of site *A* and *B*.** In a) the magnetic field dependence of site *A* is shown where the orange and black markers correspond to the spin-preserving and spin-flip transition, respectively. In b) a similar experiment is shown for site *B*.

observed. This numbers of lines can be understood by considering the orientation of the magnetic field relative to the crytal axis. Here the field points along [100] which is a high-symmetry axis in silicon. Thus three of the four lines should have the same effective g-factor and might not be resolved here. One would thus expect more lines to appear when the magnetic field orientation deviates from the high-symmetry axis, i.e. by tilting the sample as shown in the next section. A larger magnetic field would help to clearly identify all fluorescence lines, but that was not possible at that time due to the interference of large magnetic fields with a neighboring experiment. This is also the reason why I cannot assign each spin-flip transition to its corresponding spin-preserving transition. In principle, one could use a narrowband filter with a bandwidth of ~ 0.11 nm which, however, would require a larger Zeeman splitting to fully resolve the lines within the filter.

In addition, many more lines appear, corresponding to excited state crystal field levels of neighboring sites. The broad line at 1535.96 nm crossing the spin-flip transition of site *A* at around 90 mT, e.g., or the thin line at 1535.75 nm are overlapping with the lines of site *A* making an accurate analysis difficult. This can be improved when using a filter which would be placed on a higher-lying crystal field transition of the main sites. Thus, other sites with different crystal field splitting would be suppressed.

Such measurements are repeated for site *B* centered at 1537.76 nm as shown in Fig. 6.14 b). Here, again several spin-flip and spin-preserving lines become visible as indicated by the black and orange markers on top. Here I count in total eight lines which lacks half of the number of expected lines, from the previous assumption for an erbium site having four orientations in the crystal lattice. I also find several crystal field levels in the vicinity. Especially the two crystal field levels at 1537.61 nm and 1537.66 nm are interesting. When increasing the magnetic field an avoided crossing indicates that these two levels are excited-state crystal field levels belonging to the same site [141]. Such an avoided crossing inside the $^4I_{13/2}$manifold has been observed in Er^{3+}:Si at high magnetic fields in the past [142]. Due to the very small separation of these two levels on the order of ~ 50 pm I speculate they are either related to site

P or to an optical site. As shown in the previous crystal field measurements in Figs. 6.3 and 6.13, both of these sites show a narrowband fluorescence emission around 1537.6 nm making it difficult to definitely assign the crystal field levels to one of these sites. In addition, I also encounter close crystal field levels with no signs of avoided crossing, e.g., at 1537.91 nm and 1537.93 nm. This suggests that they both correspond to crystal field levels of two different sites.
Further measurements and discussion of the magnetic field measurements on site P are provided in the appendix B.4.

Tilted magnetic fields

As discussed in the previous section, the Zeeman splitting of the main sites A, B and P is complex due to the many neighboring crystal field levels and many possible site orientations of the sites in the crystal. To further investigate the symmetry and the g-tensor the sample is mounted on a rotating piezo stage inside the cryo as sketched in Fig. 6.15 a). The rotation stage (Attocube ANRv51) is mounted on top of the x,y, and z-piezo positioners and allows for rotating the sample in the horizontal plane as indicated by the direction of the rotating arrow. The rotating range, however, is limited in the experiment due to the tapered-fiber coupling. One needs to rely on an optical image from inside the cryostat to align the waveguide and tapered fiber relative to each other. For increasing tilt angles the image becomes blurry as the focal point on the chip is shifted out of the aspheric lenses' focus. This makes it impossible to reliably couple to the waveguide and limits the maximum rotation angle φ to $\sim 25°$. The discussion below focuses on the measurements of site B only. The tilted magnetic field measurements on sites A and P can be found in the appendix B.4. The panels Fig. 6.15 b) - f) show the magnetic field maps for different rotating angles where φ is indicated in each panel in the lower-left corner. Upon increasing the angle a further splitting of both spin-flip and spin-preserving lines appears, indicating that the applied field doesn't point along a high-symmetry crystal direction anymore. Depending on the orientation of the site relative to the external magnetic field the levels are split stronger or weaker which is typical for an anisotropic g-tensor. The overall number of transitions varies depending on the respective angle as the magnetic field direction doesn't point along a high-symmetry axis of the silicon crystal anymore. There is also some asymmetry in the line shapes visible, e.g., the line at 1537.70 nm which can be either attributed to a crystal field level very close to site B or to ^{167}Er induced hyperfine splitting. The latter significantly complicates the analysis as ^{167}Er has a nuclear spin of $I = 7/2$ resulting in up to 16 hyperfine levels per Kramers' doublet [143].
I conclude that in the current sample, containing the same amount of ^{170}Er and ^{167}Er, a thorough analysis of the g-tensor is hardly possible. In addition, the magnetic field strength which can be applied is limited and the finite bandwidth of the filter prevents the assignment of related spin-flip and spin-preserving transitions. The limited rotating capabilities make it difficult to gain more insight into the symmetry

of the sites. I therefore leave these measurements here and turn to the investigation of the spin-dependent properties as described in the next section.

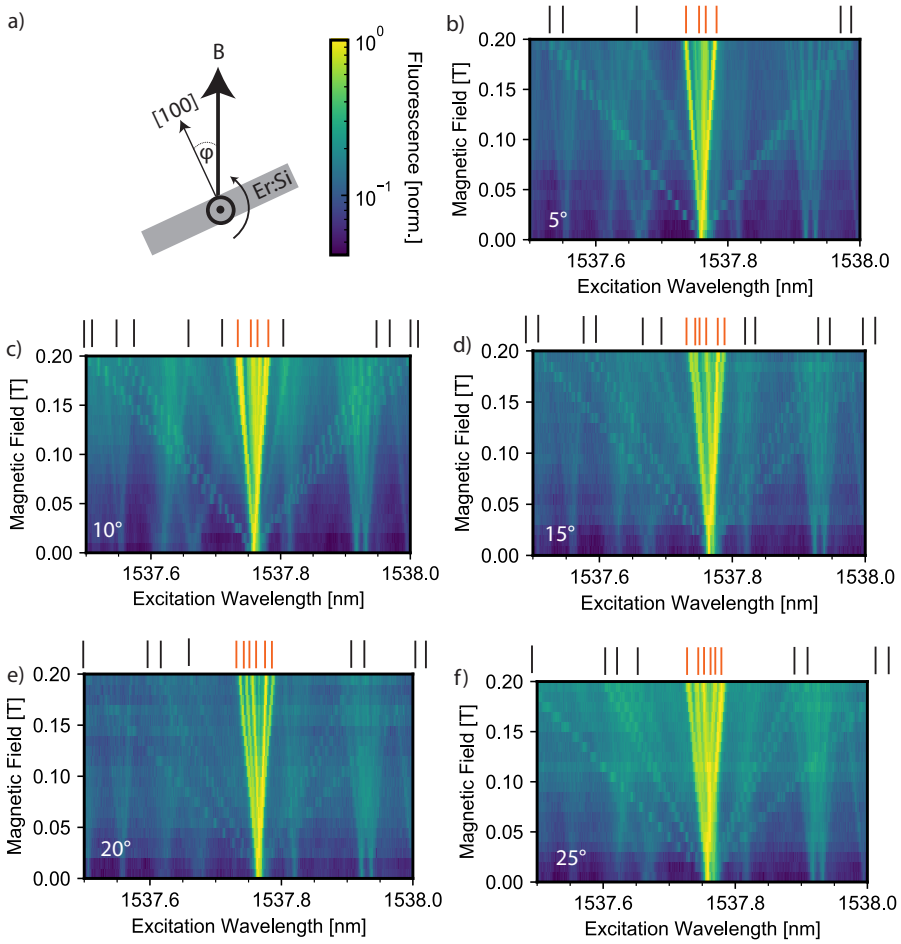

FIGURE 6.15: **Tilted magnetic field on site *B*.** In a) the rotation axis [110] of the sample relative to the external magnetic field direction is shown. Panels b)-f) show magnetic field maps for different angles φ while the markers again indicate associated spin transitions. The fluorescence signal is normalized to one. The associated colorbar for all panels in shown in a).

6.10 Towards an Er^{3+}:Si spin-photon interface

An important figure of merit is the electron spin-relaxation or electron spin lifetime T_1 which defines the time until the population of a two-level system has returned to its equilibrium state after being excited. In general $T_2 \leq 2T_1$ holds, limiting the coherence time T_2 as the phase is lost, when the system relaxes to the ground state. One can generate an effective spin-1/2 manifold by applying a magnetic field and making use of the Zeeman splitting discussed in the previous sections. One then can distinguish spin-selective transitions similar to the one presented in the chapter 2 by monitoring the fluorescence amplitude. I expect spin lifetimes exceeding several milliseconds estimated from the optical lifetime of the increased optical decay when

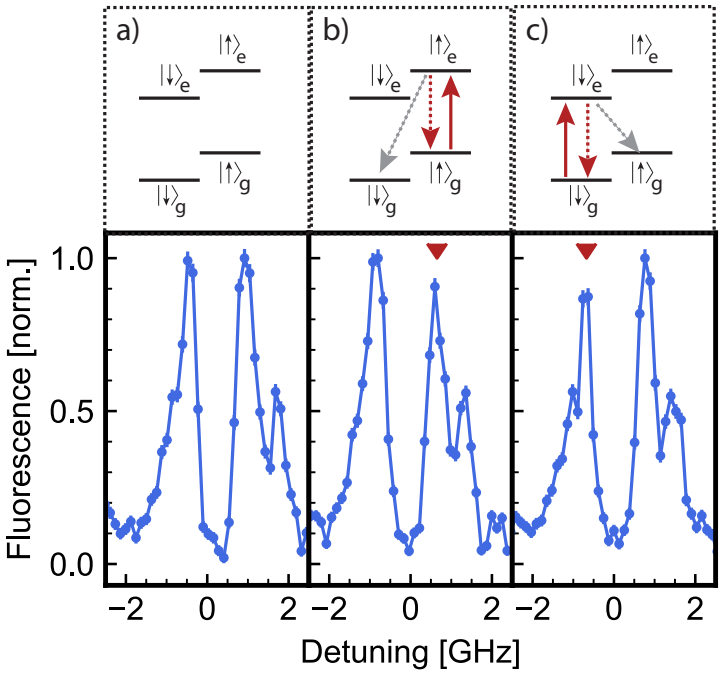

FIGURE 6.16: **Spin population transfer.** For a far-detuned burn laser the Zeeman split peaks have the same amplitude as the levels are in thermal equilibrium as shown in a). When tuning the burn laser on resonance with one of the spin-preserving transitions in b) and c) a decrease in fluorescence is visible on the respective transition. Solid lines are a guide for the eye.

investigating the Zeeman splitting at very low temperatures.

Optical spin pumping

By applying a magnetic field of 200 mT at $\varphi = 0°$ the ground and excited spin levels of site B split by ~ 2 GHz. The sample temperature is set to ~ 7 K ensuring a finite spin lifetime. Also, the fluorescence signal is filtered to exclude background from optically active sites. In addition, another laser, denoted as the "burn" laser in the following, is added to the optical setup. This laser field is used for driving the spin-preserving transition as indicated in the top part of Fig. 6.16. The bottom panel in Fig. 6.16 a) displays the two peaks corresponding to the two spin-preserving lines when the burn laser wavelength is set far away. As expected the two peaks have an equal amplitude as both ground state levels are in thermal equilibrium and thus equally populated at this temperature and magnetic field. Tuning the burn laser in resonance with one of the two spin-preserving transitions induces a population imbalance as shown in Fig. 6.16 b) and c). The burn laser excites electrons from $|\uparrow\rangle_g \rightarrow |\uparrow\rangle_e$ ($|\downarrow\rangle_g \rightarrow |\downarrow\rangle_e$), depopulating $|\uparrow\rangle_g$ ($|\downarrow\rangle_g$). A subsequent weak probe pulse thus can only excite the remaining population in the depopulated level wheres the other ground state level is still fully populated. This imbalance is reflected in the

different fluorescence amplitudes shown in Fig. 6.16. In principle, exciting the spin-flip transition would yield a larger fraction decaying into the opposite spin ground state resulting in larger pumping efficiency. However, this was not observed in these experiments most probably due to a too-small laser power to saturate this transition.

Spin lifetime

After proving that some level of spin-pumping exists in the system, I investigate the spin lifetime T_1. The spin lifetime is obtained by scanning the delay between burn and probe laser pulses and monitoring the fluorescence. For increasing delays one expects more ions to relax to a 50:50 statistical mixture of the two ground states which in turn yields a larger fluorescence amplitude for larger delays. The corresponding measurement is shown in Fig. 6.17 where the inset shows the pulse sequence. The experiment is performed at 7 K where T_1 is expected to be limited to around 19 ms judging from the measurements of the Orbach coefficient discussed in section 6.7. The burn laser ("B") excites the spin-preserving transition which is then probed

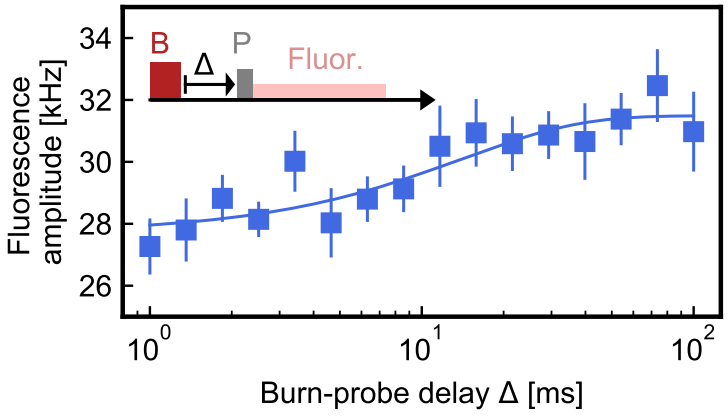

FIGURE 6.17: **Spin lifetime T_1.** By scanning the time Δ between burn ("B") and probe ("P") pulse the spin lifetime T_1 can be measured. A single exponential fit (solid line) yields T_1 = 14(7) ms.

by a second, weaker pulse ("P") after some delay Δ, measuring the amplitude of the fluorescence signal ("Fluor."). For increasing Δ also the fluorescence signal is increasing. An exponential fit is used for extracting a value of T_1 of around 14(7) ms. The large uncertainty is due to the little contrast and the required long integration times, giving large error bars on the data. The reason for the low count rate is the need of filtering the fluorescence signal due to the optical background. I also note that T_1 is indeed much larger compared to the optical lifetime but smaller compared to observed T_1 times in Er:YSO which can be on the order of tens of seconds [124, 61]. The shorter lifetime can be ascribed to the Orbach process taking place at 7 K limiting T_1 to around 19 ms. I expect to measure much larger T_1 when decreasing the temperature. However, this comes at the price of a lower emission rate resulting in larger error bars. Also, there is much space for improvement by carefully optimizing

the pulse sequence parameters like pulse intensity, pulse duration, inter-pulse delay, and temperature. In addition, by applying microwave pulse the spin states might be reset and allow for a larger signal. Nevertheless, this optical measurement of the spin dynamics in Er^{3+}:Si highlights the potential of Er^{3+}:Si as a material platform for quantum memories.

6.11 Summary

To conclude this chapter I summarize the most important findings with a focus on the achieved improvements of the Er^{3+}:Si platform. By using pure, CVD grown silicon in combination with optimized implantation parameters deterministic Er-sites can be generated with narrow inhomogeneously broadened lines and short optical lifetimes. Furthermore, a better understanding of how the waveguide geometries influence the Er^{3+} emission has been obtained by calculating the local density of states and performing a Monte Carlo simulation. By improving the sample nanofabrication the waveguide sidewall-roughness-induced losses could be reduced, enabling measurements on millimeter long ridge waveguides yielding an improved signal-to-noise ratio. This in turn allowed for measuring the crystal field splitting in both ground and excited state for the three main sites in Er^{3+}:Si. Further progress was made in enhancing the sensitivity of the measurement setups allowing to extract homogeneous linewidths close to the lifetime limit of the erbium ions. This measurement technique and the knowledge of the crystal field splitting enabled the identification of the Orbach process as the major contribution of the spin-lattice relaxation. Among the major sites, I identified several optically active sites which are independently excited and can emit both broad- and narrowband fluorescence. For a better understanding of the site symmetry and the spin levels I measured the Zeeman splitting of the main erbium sites where several spin transitions were identified for various magnetic field orientations. This information was finally used to perform the first measurements of spin-pumping and probing a millisecond long spin lifetime, highlighting the potential of Er^{3+}:Si in future quantum applications.
Still, the erbium site symmetries are unknown which calls for a more thorough investigation. In addition, a complete description of the g-tensor is still missing as for that the Zeeman splitting needs to be recorded for several magnetic field orientations. Also, so far the observation of coherent processes like photon echos or Rabi oscillations is lacking while both are typically required in quantum memory protocols.

Chapter 7

Erbium dopants in pure silicon

In this chapter, I discuss the latest generation of erbium-doped silicon: Er^{3+}:Si rib waveguides made of high-purity float-zone silicon. I find the same sites as in the CVD grown samples with similar properties proving the capability of deterministic generation of Er-defects in different silicon substrates.

7.1 Sample specifications

Sample preparation

As a substrate material, a SOI wafer with a float-zone (FZ) grown silicon device layer is used. The FZ technique is a crucible-free crystal growth method where the molten zone is kept between two vertical solid rods by its own surface tension. The main advantage of the FZ growth is the absence of a (quartz) container, which precludes contamination by the crucible material and the generation of crystal defects caused by the interaction between the growing crystal and the hosting vessel [144]. Float-zone silicon contains up to two orders of magnitude less carbon and oxygen [75], two elements which are known for forming precipitates with erbium [74]. The undoped device layer has a thickness of $2 \pm 0.5\,\mu m$ and is residing on a $1\,\mu m \pm 5\%$ buried SiO_2 layer. The wafer is diced in <110> direction into $10 \times 10\,mm$ chips and implanted with a mixture of erbium isotopes of natural abundance at room temperature under a tilt angle of 7°. Several chips with two different sequences of erbium fluences were implanted. One high and one low dose sequence, yielding two different erbium concentrations. The detailed implantation parameters are listed in appendix B.5. For achieving a homogeneous implantation profile on the order of the device layer thickness, three individual implantation runs at high energies are required. The implantation was done using a Tandetron accelerator providing implantation energies on the order of several MeV. Secondary ion mass spectrometer (SIMS) measurements confirm the targeted implantation profile as shown in appendix B.5. Unfortunately, a SIMS analysis of the impurity concentration in the float-zone silicon was not possible due to electric charging effects of the silicon surface.
After implantation the chips are annealed at 500 °C for 60 s according to the annealing recipe given in appendix A.2. The annealing time was reduced here since previous studies showed an enhanced photoluminescence intensity for shorter times

[145] and simultaneously minimize erbium diffusion to avoid clustering [146]. Then, rib waveguides are fabricated, using the geometric parameters introduced in chapter 3.4 with a rib width of $w = 2\,\mu m$ and a rib height of $h = 0.45\,\mu m$. The straight waveguides are $\sim 9\,mm$ long and thus span the complete chip. The end facets are mechanically polished allowing for optical side coupling using single-mode glass fibers as sketched in Fig. 3.2 a).

Glued fibers

The mode size of the rib waveguides' fundamental mode is in the range of micrometers and smaller than the mode of a standard single-mode fiber as already discussed in chapters 3.4 and 3.6. Still, the mode overlap should be sufficiently large which makes the fiber butt coupling a promising approach as it is simple. Fig. 7.1 shows a photograph of the gluing setup. The FZ chip with the waveguides is glued onto a custom PCB board using silver adhesive that ensures mechanical stability and thermal anchoring. Two microscope objectives, mounted from the top and the side are used to align the fiber relative to the waveguide and monitor the laser transmission through the waveguide. After optimizing the position of the fiber by maximizing the transmission monitored on an infrared camera placed behind the side objective the cleaved fiber end facet is glued (Norland NOA 88) to the chip and the adhesive is cured using UV light. A few millimeters away from the chip another, larger, portion of glue is dispensed working as strain relief after curing. This procedure is repeated for ~ 4 additional fibers being glued to one side of the chip. This number is limited by the amount of dispensed glue which prevents the glueing of more fibers. In order to gain the capability of transmission measurements, this procedure is repeated from the other side where the transmission signal is now monitored on a photodiode or powermeter maximizing the signal in the fiber connected to the waveguides' end facet on the other end of the chip.
The coupling efficiency is susceptible to the mode mismatch of fiber and waveguide as well as the relative alignment between both. Here a standard SMF-28 fiber proved more reliable compared to high-NA fibers despite the mode mismatch being large. The reason is that the effect of misalignment during cooldown is less relevant when using SMF-28 fibers due to their large mode diameters. On average, coupling efficiencies of $2 - 4\,\%$ one-way are achieved which typically changes by a factor of ~ 2 when cooling the sample below $2\,K$. This holds when using SMF-28 fibers but can be larger when using fibers with smaller mode diameters. Still, this approach reduces the experimental overhead significantly as there is no need for positioning of a sample inside the cryostat. Also, several chips can be simultaneously cooled down and used for experiments.

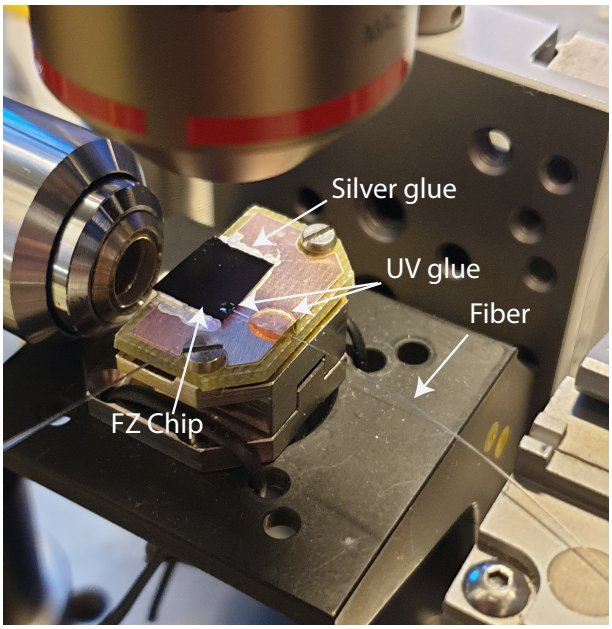

FIGURE 7.1: **FZ glueing setup.** Two microscope objectives allow the alignment of the fiber to the waveguides on the FZ chip while in situ monitoring the transmission using an infrared camera. The fibers are glued to the chip using UV curing adhesive.

Waveguide losses

For estimating the waveguide losses I followed the approach given in [147]. The idea is based on the assumption that the waveguide with both its end facets is essentially a Fabry-Pérot resonator with finesse $\mathcal{F} = \Delta_{\mathrm{FSR}}/\Delta_{\mathrm{FWHM}}$, where Δ_{FSR} is the free spectral range and Δ_{FWHM} the resonance linewidth. The finesse is measured by monitoring the reflected Airy distribution intensity which is then used for estimating the waveguide loss. Even for a very large round-trip loss of 97 %, a finesse of approximately 1.08 is expected which should be sufficient as this method requires $\mathcal{F} > 1$ to work. It turns out that, this is not the case for the rib waveguides here, as $\mathcal{F} < 1$. Possible reasons are the mechanically polished waveguide end facets reducing the reflectivity and the end facets not being perfectly perpendicular to the waveguide which leads to scattering and a dramatically reduced finesse. Therefore, for $\mathcal{F} < 1$, the Lorentzian lines underlying the Airy distribution cannot be resolved and the above method will produce no reliable results. In future samples, the mechanical polishing might be replaced by a deep reactive-ion etching process, which would yield higher reflectivities ensuring $\mathcal{F} > 1$.
An indication that the waveguide losses are low is given in section 7.5, where the homogeneous linewidth is simultaneously measured in transmission and reflection. The power-broadened homogeneous linewidths are matching for both configurations, indicating low losses compared to the previous sample generations discussed in this thesis.

7.2 Resonant spectroscopy

This chapter describes the spectroscopy data obtained from experiments on low-dose erbium-doped float-zone Er^{3+}:Si samples.
In order to utilize Er-complexes in silicon it is a central task to develop a process which creates deterministic erbium sites for different silicon substrates with the same physical properties. In this work the two Er^{3+}:Si samples discussed in chapters 5 and 6 show sites differing in wavelength, numbers and linewidths. Here, I show that by annealing at 500 °C the same erbium sites can be reproducibly generated in different silicon substrates.
For the resonant spectroscopy experiment I set the excitation pulse length to 5 µs with 700 µW power in the fiber. With a coupling efficiency of ~ 2 % this corresponds to around 14 µW in the waveguide. These parameters yield the best signal-to-noise ratio for this measurement configuration. The emitted fluorescence is measured in a 400 µs interval after the laser pulse has excited the ions embedded in the waveguide. The sample is again kept at a base temperature below 2 K. Fig. 7.2 shows the resonant fluorescence spectrum measured in transmission of a low-dose FZ Er^{3+}:Si waveguide, normalized to the maximum peak height to allow for better comparison. Again, fluorescence peaks similar to the Er^{3+}:Si samples investigated in the previous chapters are found. However, the overall number of peaks is reduced. Instead, erbium is now predominantly integrated into the previously found Er^{3+}:Si CVD sites. The matching lines correspond to sites *A* (~ 1536.06 nm) and *B* (~ 1537.77 nm) as indicated by the colored markers in Fig. 7.2. Again, a significant amount of dopants is located in the "erbium-pair" site *P* (~ 1538.2 nm) and few others. Remarkably, the broad background present in the CVD samples that stems from off-resonantly exciting site *O* disappears in the FZ material, giving better signal-to-noise ratio to resolve the peaks. As discussed in the previous chapter, these optical sites are likely to be located

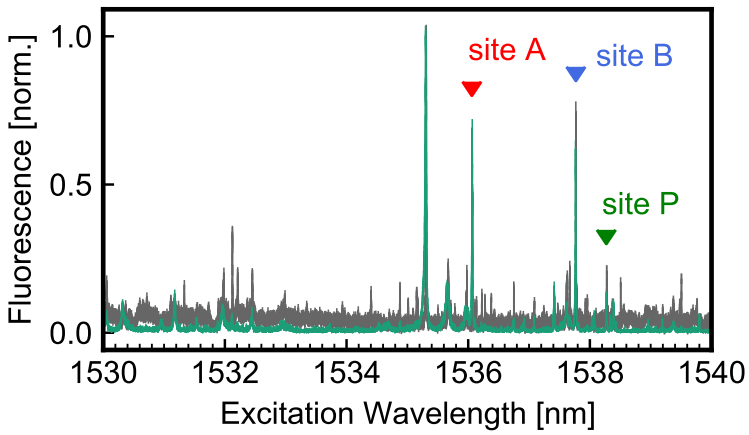

FIGURE 7.2: **Resonant spectrum FZ Er^{3+}:Si .** Transmission fluorescence spectrum of a FZ Er^{3+}:Si sample (green). The background is reduced compared to the one obtained in the CVD samples (grey) but the major sites *A* (red marker), *B* (blue marker) and *P* (dark green marker) coincide.

close to the conduction band which makes them prone to carrier-mediated excitation processes [47]. There is the possibility that due to the float-zone silicon, which is known for its very low defect concentration [148], the formation of trap states is reduced, and thus the formation of optically active sites in the FZ silicon is less likely. Another explanation is related to the rib waveguide geometry. There, the waveguides are patterned onto a continuous silicon device layer where quasiparticles like excitons or free carriers, prone to decaying via an optically active site, can freely move in the $\sim$ 100 mm^2 silicon device layer. Thus the possibility of recombination in the waveguide is reduced as these carrier-mediated processes can occur at many different positions in the silicon layer. This stands in contrast to the ridge waveguides which are electronically isolated on silicon dioxide. Here, the possibility of electron-induced excitation in the waveguide is enhanced due to the surrounding insulating SiO_2 which prevents the mobile carriers from moving elsewhere but the ridge waveguide. There they can then recombine via optically active sites inducing the optical background as shown in Fig. 7.2. The impact of the free charge carriers on the background, for example, can be tested by placing electrodes close to the waveguides and apply an electric field, which can sweep the carriers out of the waveguide [149], possibly reducing the optical background. This, however, is left for future work.

7.3 Inhomogeneous broadening

Fig. 7.3 shows a high-resolution scan of the three main sites *A*, *B* and *P*. Compared to the sites in the CVD samples (see Fig. 7.2), the inhomogeneous linewidths measured here are larger. For site *A*, a Lorentzian fit extracts $\Gamma_{\text{inh}} = 1.05(1)$ GHz. Site *B* shows an inhomogeneous linewidth of 0.94(1) GHz and for site *P* a value of 0.86(6) GHz is extracted. The lineshape asymmetry observed in the CVD samples in chapter 6.4 is not visible here, the lines are fitted well by a single Lorentzian functions. When discussing the double-peak structure of Γ_{inh} in the CVD samples, this shape was attributed to strain in the device layer or two different erbium isotopes. Here, the strain present in the device layer is expected to be reduced due to the 2 µm thick silicon layer and the only 1 µm thickness of the buried oxide layer. However, in the first sample generation, discussed in chapter 5, and in the float-zone samples, erbium was implanted in natural abundance. Also, both CZ and FZ samples, show an almost perfect Lorentzian shaped inhomogeneous linewidth, while the double peak structure was only observed in samples with only two implanted erbium isotopes. A silicon sample containing a single erbium isotope only and comparing the frequencies of the fluorescence signal should help to give a final answer.

7.4 Optical lifetime

In this section, again the optical lifetime of the three main sites is investigated. Similar to the measurements before, the crystal field level Y_2 is excited and the fluorescence

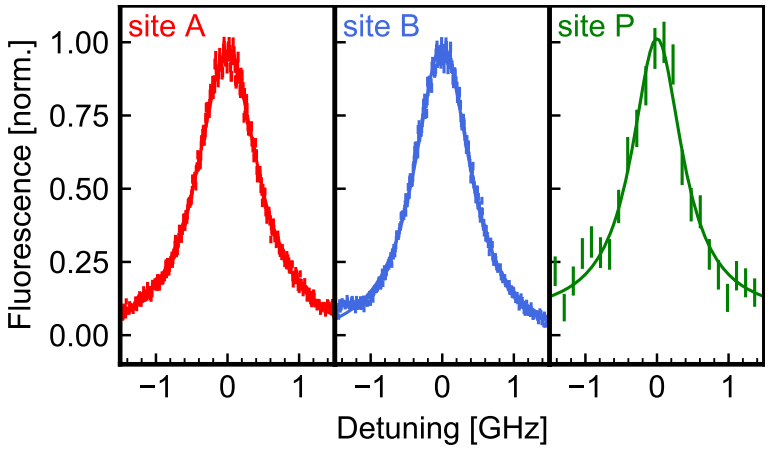

FIGURE 7.3: **Inhomogeneous linewidths.** The three panels show the inhomogeneous linewidth of the three main sites. The data is fit using a single Lorentzian line (solid line). For site A, $\Gamma_{\text{inh}} = 1.05(1)$ GHz, for site B, $\Gamma_{\text{inh}} = 0.94(1)$ GHz and for site P a value of 0.86(6) GHz is measured.

into the first ground state crystal field level Z_1 is measured by placing a tunable filter into the detection path. This ensures the suppression of the non-resonant background and comparability to the previous lifetime measurements in the CVD silicon samples.

Fluorescence decay

Fig. 7.4 shows the fluorescence decay of the three main sites after the laser pulse is switched off. The color coding for sites A (red), B (blue) and P (green) is the same as in chapter 6 as they share the same properties. Each trace is fit using a single exponential function. I extract a lifetime of 0.186(1) ms for site A, 0.142(1) ms for site B and 1.018(1) ms is measured for site P. All lifetimes are $\sim$ 50% faster compared to the optical lifetimes of these sites measured in the CVD silicon. I also note that the data is very well fit by using single exponential decay curves. This is in contrast to the bi-exponential function employed in chapter 6.5 to fit the lifetime data, which resulted from the geometric confinement of the erbium emitters in the ridge waveguide. Again, site B decays the fastest, followed by site A and P, similar to the measurements in erbium-doped CVD silicon. To further investigate this, the local density of states (LDOS) for different emitter configurations in a rib waveguide is calculated.

Lifetime modification by DOS

The spatial extent of the fabricated rib waveguide geometry leads to a bulk-like environment for the ions inside the waveguide. To verify this assumption the Purcell factor F_P and the β-factor of the rib waveguide are calculated for different emitter directions. In Fig. 7.5 a) the Purcell factor is approximately 1 almost everywhere in the waveguide's cross-section for all three emitter directions. Therefore, the lifetime of

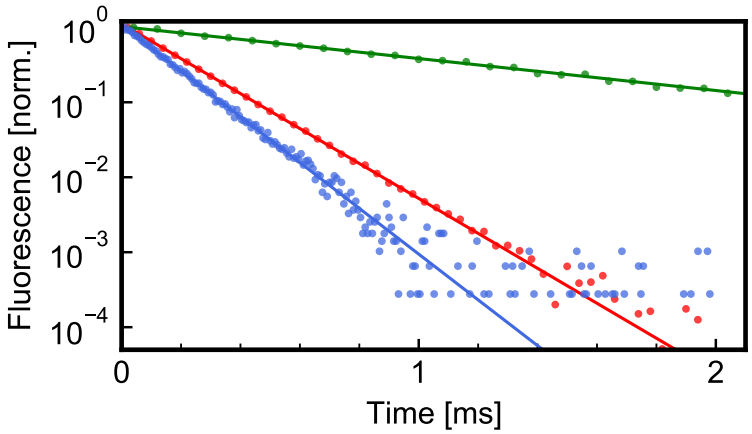

FIGURE 7.4: **Optical lifetimes.** Fluorescence decay and fit using a single exponential function. A lifetime of 0.186(1) ms for site A (red) and a lifetime of 0.142(1) ms for site B (blue) is measured. Again, the pair site P (green) exhibits a longer optical lifetime of 1.018(1) ms.

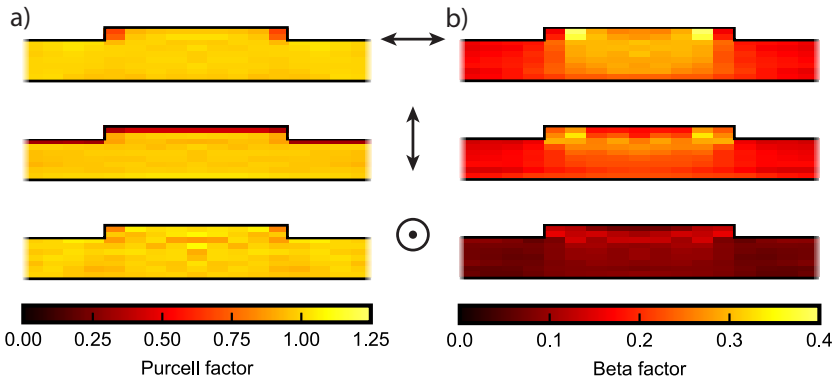

FIGURE 7.5: **Rib waveguide Purcell and β-factor simulation.** In a) the simulated Purcell factor F_P is shown in the rib waveguides cross-section for three different dipole emitter directions indicated by the black arrows. In b) the β-factor is shown for the same three emitter directions.

the ions is not affected by the rib waveguide geometry and thus the single exponential decay, observed in Fig. 7.5, is in accordance with the simulation here. The simulation of the β-factor is shown in Fig. 7.5 b). Here, the β-factor is ranging between 0.1 and 0.4 in the center of the rib waveguide and decreasing for larger distances from the waveguide core. This further strengthens the developed theory of the local density of states affecting the emitters in the different waveguide geometries investigated in this thesis.

7.5 Homogeneous linewidth

In this chapter, measurements of the homogeneous linewidth in the FZ Er^{3+}:Si sample are presented. First, the already discussed EOM measurement scheme is used to extract an upper bound on Γ_h. In addition, another, equivalent measurement technique is presented, which can also be used to determine the power-broadened homogeneous linewidth.

EOM technique

Similar to the measurements in chapter 6.6, three concatenated electro-optic modulators are used to generate 27 laser fields in the rib waveguide. By scanning the separation of the modulated peaks an upper bound of the power-broadened homogeneous linewidth can be estimated by measuring the transient spectral hole width. The measurement was conducted at a temperature of 7 K to avoid effects of persistent spectral hole burning. In the previous measurements of the homogeneous linewidth in chapter 6.10 this effect was mitigated by randomly sweeping the lasers lines within the inhomogeneously broadened line. The homogeneous linewidth Γ_h as a function of intensity I is shown in Fig. 7.6. Due to the new measurement setup, where two fibers are coupled to the chip, this measurement can be performed both in reflection and in transmission at the same time. In Fig. 7.6, filled symbols represent data taken in transmission and open symbols correspond to measurements in reflection. The data points are overlapping very well indicating low losses of the rib waveguide. If a lot of power would be lost along the waveguide, the signal would originate predominantly from the end of the waveguide at which the fiber is attached. And, at the transmission side the intensity would be much lower. So, the transmission side

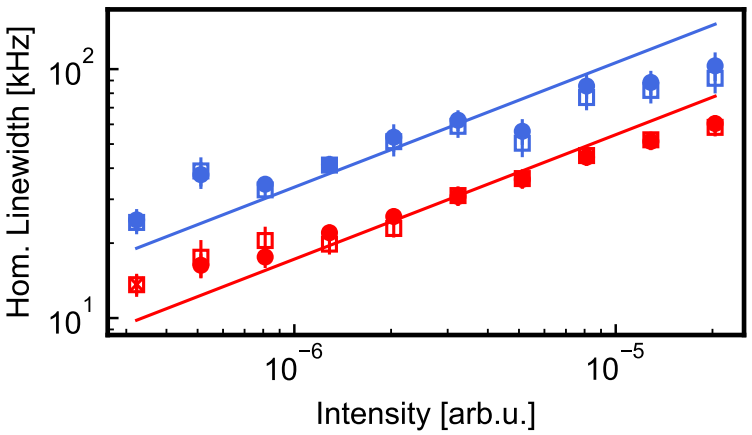

FIGURE 7.6: **Homogeneous linewidth.** The dependence of the homogeneous linewidth on the intensity present in the rib waveguide is shown for sites A (red) and B (blue). For increasing power, Γ_h follows a $\sqrt{I}$ dependence indicated by the solid lines. Open (filled) symbols correspond to data measured in reflection (transmission).

should have significantly narrower linewidth as it scales with the intensity I present in the waveguide. But since the measured homogeneous linewidths in reflection and transmission are identical for both configurations the waveguide losses seem to be negligible. For site A a homogeneous linewidth of 13(2) kHz and a value of 24(3) kHz for site B is extracted. These values are still much larger than the lifetime limit of $\sim$ 0.5 kHz. Again, this deviation is attributed to power broadening, the inherent limitation of the measurement scheme. The offset between the data of site A and B can be attributed to the misalignment of the modulated lines on the inhomogeneous line of site B.

Comparison to another technique to measure $\Gamma_\mathbf{h}$

In addition to the so far used method of choice, the EOM technique, I use an additional measurement scheme successfully introduced in Er^{3+}:Si [117] to give an upper bound to the homogeneous linewidth. Similar to the EOM technique it is based on transient spectral hole burning, i.e. the lifetime of the spectral holes being on the order of the optically excited state lifetime. By measuring the change in absorption at the position of the spectral hole, conclusions on the homogeneous linewidth of the medium can be drawn. First, a narrowband laser line is centered on the inhomogeneous peak

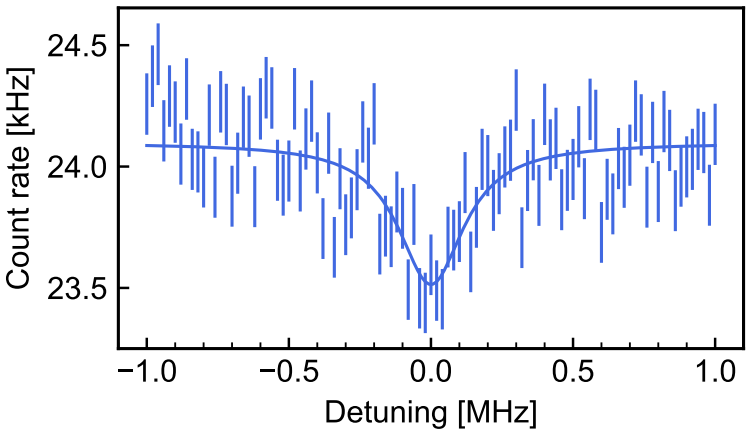

FIGURE 7.7: **Alternative technique for measuring $\Gamma_\mathbf{h}$.** A burn laser pulse at $\nu = 0$ MHz is saturating the optical transition of site B, removing parts of the population from the inhomogeneous linewidth. The resulting spectral hole is measured by scanning a probe laser around the burn lasers' frequency and monitoring the emitted fluorescence signal. The hole width is extracted using an inverted Lorentzian function.

of site B. By applying a laser pulse, which saturates the optical transition, a spectral hole at the relative detuning $\nu = 0$ MHz is generated. The hole width is measured by monitoring the fluorescence after a second pulse, the probe pulse, whose frequency can be scanned from $\nu = \pm 10$ MHz using an acousto-optic modulator. Thus by tuning the probe pulse frequency while keeping the frequency of the burn pulse fixed, an optical hole at zero detuning ($\nu = 0$ MHz) is expected. In order to increase the signal-to-noise ratio several laser lines are applied, simultaneously probing multiple holes

within the inhomogeneously broadened line. Previously three concatenated electro-optical modulators were used to generate $3^3 = 27$ laser lines separated by a few tens of megahertz. To further increase the number of lines, two electro-optic modulators are modulated with two rf frequencies each at the same time. This generates a total number of $3^4 = 81$ modulated laser lines further improving the signal-to-noise ratio. In addition, to avoid artifacts from persistent spectral hole burning, the position of the burn-probe sequence is shifted randomly within the inhomogenoeus line by a few megahertz after each measurement. The sample is kept at a temperature below 2 K during these measurements. A typical measurement trace is shown in Fig. 7.7. As expected the dip in the fluorescence signal is visible at zero detuning, indicating a decrease in absorption leaving a spectral hole. In this measurement, the pulse length was fixed to 10 µs for both, burn and probe pulse. This pulse length was chosen to be sufficiently short compared to the optical lifetime. The hole width (FWHM) is extracted using an inverted Lorentzian fit, indicated by the solid line in Fig. 7.7 and yields in this particular measurement a hole width $\gamma = 0.28(6)$ MHz. Thus γ is by a factor of five narrower than the hole widths presented in [117]. This discrepancy might originate from a different site investigated or power broadening. In general, $\gamma/2 = \Gamma_h$ [150] which gives a measured homogeneous linewidth of $\Gamma_h \sim 160$ kHz being of the same order as the results obtained using the EOM technique.
Similar to the EOM measurements presented in the previous sections and chapters, the experimentally determined hole width is limited by power broadening. So I additionally investigate the homogeneous linewidth as a function of the laser intensity. The corresponding measurement is shown in Fig. 7.8 displaying the homogeneous linewidth obtained by extracting the hole widths at various pulse intensities.
For increasing intensity I, I find an increase in the homogeneous linewidth. This

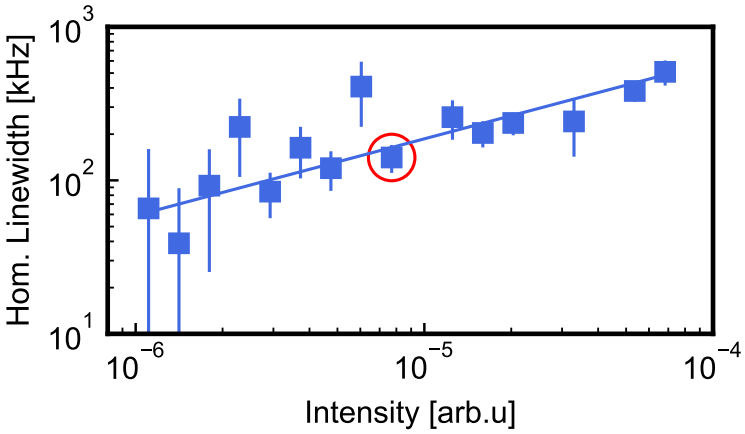

FIGURE 7.8: **Homogeneous linewidth power dependence.** Blue data points correspond to the homogeneous linewidth extracted by measuring the hole width on site *B*. The data is very well described by a power-law (solid blue line). The red circle indicates the data extracted from the measurement trace shown in Fig. 7.7. The intensity is given in arbitrary units here due to a faulty power calibration.

increase is well fit using a power-law $\propto \sqrt{I}$ (solid blue line). The red circled data point corresponds to the measurement trace shown in Fig. 7.7. The smallest value for Γ_h is 40(50) kHz, however, with a very large error bar. This is due to the little power present in the waveguide and the resulting long integration times. Adapting the integration times accordingly would have increased the measurement time to unpractical values. The hole burning method recovers narrow homogeneous linewidths compared to the values measured before using the EOM scheme showing the equivalency of both measurement techniques. However, I point put here that the EOM measurement technique yields a better signal-to-noise ratio compared to the scheme used by [117].

7.6 Dose and annealing study

In this section, I investigate the influence of the erbium concentration and the post-implantation annealing temperature on the optical properties of the erbium-doped FZ silicon.

Erbium concentration

The measurements shown in this chapter so far, are performed on low-dose erbium implanted float-zone silicon. This dose corresponds to measured erbium fluences of $4 \times 10^{11} - 1 \times 10^{12}\,\mathrm{cm}^{-2}$ during implantation. In addition, another float-zone wafer was implanted using fluences of $4 \times 10^{12} - 1 \times 10^{13}\,\mathrm{cm}^{-2}$, yielding high-dose erbium implanted float-zone samples. The detailed implantation parameters are provided in appendix B.5. Both samples are post-annealed at 500 °C using the standard rapid-thermal-annealing procedure described in appendix A.2. Again, resonant flu-

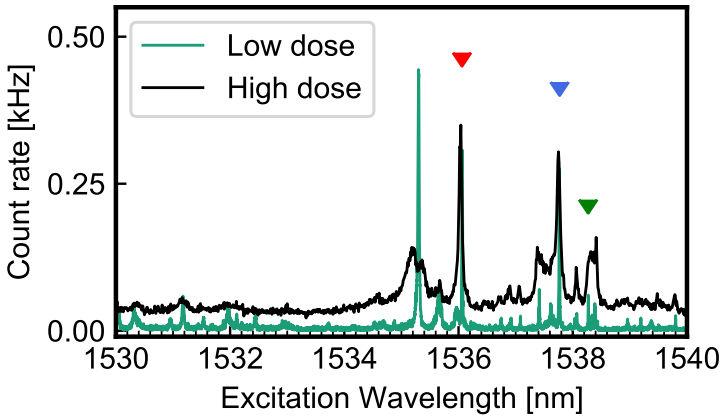

FIGURE 7.9: **Low-and high-dose implanted FZ Er^{3+}:Si .** Resonant fluorescence spectrum of a low- (cyan) and high-dose (black) erbium doped float-zone silicon. The same main sites are found in the high-dose samples but with an increased inhomogeneous broadening. A Lorentzian fit (not shown) is used to extract linewidths of 7.8(1) GHz for site *A*, 13.9(4) GHz for site *B*, and 9.7(2) GHz for site *P*. The y-axis shows the single-shot count rate.

orescence spectroscopy experiments on high-dose erbium samples, similar to the measurements described in section 7.2 were performed. The corresponding data is shown in Fig. 7.9. Here, I compare the spectrum obtained from the low-dose erbium implanted silicon (cyan) to the high-dose implanted one (black). Similar to before, the same main sites A, B, and P appear again as highlighted by the red, blue, and green markers in the figure. However, the inhomogeneous line is dramatically broadened. Site A, for example, shows an inhomogeneous linewidth of 7.8(1) GHz in the high-dose sample, which is almost a factor of eight larger compared to the same sites' broadening in the low-dose sample. The same holds for sites B and P which are also significantly broadened. This suggests that still a significant number of erbium ions is located at the main sites, but owing to the increased implantation dose, a larger broadening is observed. The higher dose leads to higher strain variations, since the erbium is not size-matched to the silicon and thus creates strain in the surrounding crystalline environment. The crystal strain and the associated large inhomogeneous broadening can be reduced by optimizing the post-implantation anneal as shown in the next section. In addition, an enhanced optical background signal is observed in the high-dose silicon sample. This indicates a large number of optically active sites due to trap states generated by the implantation process.

Annealing temperature

The rapid thermal processing used in this work for repairing the crystal damage during and after ion implantation is a standard process in semiconductor technology [151]. So far, the annealing temperatures used in this work were 700 °C and 500 °C. Similar temperatures have been used in previous studies [80] but also experiments involving larger annealing temperatures have been reported [50]. However, a detailed investigation involving sites A, B and P is lacking. In general, the annealing conditions play an important role in the lineshape and implantation yield [125]. Here, I compare the inhomogeneous linewidth of the main sites A, B and P of the high-dose chip for post-implantation annealing at 500 °C and 600 °C. The measured data is shown in Fig. 7.10. Each of the three panels shows both, the inhomogeneous line measured on a sample annealed at 500 °C (vertical lines) and the same site after a 600 °C anneal (points). For all three sites, a dramatic reduction in linewidth is observed, suggesting that the increased temperature is capable of improving the silicon crystal matrix after implantation. For site A a reduction of the initial linewidth of 7.8 GHz down to 1.8 GHz is extracted using an Lorentzian fit, an improvement of a factor of four. The same behavior is observed for sites B and P where a similar decrease in linewidth is measured. I note here, that the optical lineshapes also change with implantation and annealing conditions and resemble more a Lorentzian curve after the 600 °C anneal. The inhomogeneous linewidths are comparable to the low-dose sample linewidths presented in section 7.3. This finding indicates that annealing at 600 °C reduces the inhomogeneous broadening of the main sites in the high-dose float-zone silicon sample. This sample then contains a larger erbium concentration yielding a

possibly larger optical depth, assuming an unchanged conversion efficiency, while maintaining the 1 GHz to 2 GHz inhomogeneous linewidth. In addition, an anneal of the low-dose sample at 600 °C might further reduce the measured linewidth of ~ 1 GHz, yielding values for the inhomogenoeus broadening of a few hundred megahertz, comparable to the values measured in the CVD samples in chapter 6. This, however, is left for future work. When increasing the annealing temperature to 700 °C, sites *A*, *B* and *P* vanish due to a dramatically enhanced optical background resulting in a poor signal-to-noise ratio. Also several more sharp peaks on the enhanced background appear indicating the formation of different erbium sites at around 700 °C, leading to broadband emitting complexes [47] and destroying the well-defined erbium sites. Temperatures larger 700 °C are currently not accessible due to technical limitations of the used rapid-thermal annealing oven.

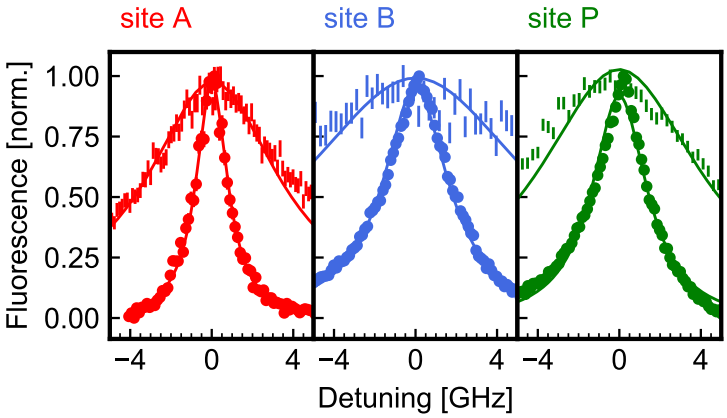

FIGURE 7.10: **Annealing study of sites *A*, *B* and *P*.** The three panels show the inhomogeneous broadening of sites *A*, *B* and *P* after 500 °C (vertical dashes) and 600 °C anneal (points). At site A, Γ_{inh} is reduced from 7.8(1) GHz to 1.8(1) GHz. For site *B* the inhomogeneous broadening is 3.8(1) GHz after the 600 °C anneal compared to 13.9(4) GHz before. Γ_{inh} at site *P* is reduced from 9.7(2) GHz to 3.2(1) GHz.

7.7 Summary

I conclude this chapter by summarizing the major results obtained here. Using a rib waveguide geometry, a set of erbium-doped waveguides in float-zone silicon was fabricated. Since in a rib waveguide the fundamental mode is in most parts confined below the rib, transmission losses due to sidewall roughness are negligible and facilitate the use of millimeter-long waveguides. Due to the waveguides' large mode diameter a fiber butt coupling technique was used, where two cleaved fiber facets are attached on each side of the chip. By using UV curing adhesive, this setup is low temperature compatible and allows for a transmission setup geometry. By performing resonant fluorescence spectroscopy, the erbium sites *A*, *B* and *P* from the CVD samples presented in chapter 6 were recovered. This is a major step towards

the generation of reproducible erbium sites in silicon with well-defined optical properties. This is ascribed to the high purity of the silicon substrate and the rather low annealing temperature of 500 °C. I measured inhomogenoeus linewidths on the order of 1 GHz and optical excited-state lifetimes of the two main sites *A* and *B* being 0.186 ms and 0.142 ms, respectively. By calculating the local density of states of the rib waveguide geometry, I showed that the obtained lifetime corresponds essentially to a dipole emitter in bulk silicon, where the waveguide geometry plays a minor role. By using the EOM measurement technique, homogeneous linewidths of a few ten kilohertz were obtained, proving again the capability of generating erbium sites with good optical properties. As the EOM technique is non-standard, another measurement scheme based on transient spectral hole burning was sued to verify the small homogenoeus linewidths. The extracted values for Γ_h were on the same order of magnitude as the second technique employed in this work, proving that it is suitable to get an upper bound of the power-broadened homogeneous linewidth. Finally, I investigated the influence of erbium concentration and post-annealing temperature on the erbium sites' properties. An annealing temperature of 600 °C is capable of reducing the several gigahertz large inhomogeneous linewidth of high-dose erbium doped silicon by a factor of four. This finding underlines the importance of a thorough implantation and annealing procedure for generating deterministic erbium sites.

Still, there is room left for additional measurements and improvements. So far, the loss coefficient of the doped rib waveguides is unknown. This is important when investigating the implantation yield, i.e. how many of the implanted ions are emitting a fluorescence signal. This would also help to determine the optical depth, which is expected to be significant in the millimeter-long waveguides. Also, the annealing temperature seems to play a major role when generating the erbium sites. Here a more detailed investigation in the temperature range from 600 °C to 700 °C is needed to better understand the transition of well-defined erbium sites towards broadband-emitting erbium precipitates. Regarding the fiber coupling, one can think of using optical fibers with smaller mode diameters, i.e. Nufern UHNA7 fibers, for better mode matching and resulting larger fiber-to chip coupling efficiencies [152]. Also, a hybrid coupling scheme is feasible where one fiber is glued to the waveguides' end facet and the other fiber is positioned on a motorized piezo stage. This would allow for optimization of the coupling at low temperatures, improving the fluorescence detection efficiency.

Chapter 8

Conclusion and outlook

In this work, a novel experimental platform based on erbium dopants in silicon was investigated. The coherent emission of erbium at telecom wavelengths in combination with the mature silicon photonic technology makes this approach interesting for future applications in quantum information processing. In particular, I have built an optical setup capable of detecting narrowband erbium fluorescence upon resonant excitation of silicon waveguide embedded erbium emitters. In total, three generations of different Er^{3+}:Si samples were investigated, all of which led to a better understanding of the previously poor knowledge of silicon containing small erbium concentrations.

The first generation of Er^{3+}:Si samples consists of a Czochralski-grown silicon-on-insulator chip where erbium at room temperature in natural abundance was implanted. Afterwards, 0.4 mm long waveguides were fabricated using electron-beam lithography and reactive-ion etching. The waveguides enabled resonant spectroscopy of the dilute erbium ensembles in silicon which otherwise has been not accessible so far. The reason is the increased optical depth due to the long waveguides which allows to excite many ions at the same frequency within the waveguide. After excitation, the ions emit a fluorescence signal which is guided within the waveguide and can be collected with high efficiency enabling a sufficiently large signal-to-noise ratio. A single-sided tapered fiber was used for efficient coupling yielding coupling efficiencies of up to 20 %. Experiments revealed several, distinct erbium sites located between 1530 nm and 1540 nm with inhomogeneous linewidths ranging from 1 GHz to 4 GHz. Some of the sites have meanwhile been found in differently processed samples of another group [117]. The measured optical lifetime was around 1 ms for all sites which is a factor 10 smaller compared to typical optical lifetimes in Er:YSO. For investigating the homogeneous linewidth Γ_h I set up a novel measurement scheme based on transient spectral hole burning. This technique allows to measure, transient spectral hole linewidths of 44 MHz up to 110 MHz depending on the respective site. Finally, I did investigate the Zeeman-splitting of each site and found strong evidence for low site symmetries as well as potentially long spin lifetimes.

For the second generation of erbium-doped silicon, the substrate material was improved by growing a layer of CVD silicon on top a commercially available SOI

wafer. The resulting device layer was implanted with ^{167}Er and ^{170}Er, only. During the implantation process the silicon substrate was annealed at 500 °C with the goal of immediately repairing the implantation-induced crystal damage. This led to reduced inhomogeneous linewidths of 0.23 GHz to 0.44 GHz in combination with optical lifetime ranging from 0.244 ms up to several milliseconds. I could show that the observed bi-exponential decay of the optical lifetime can be attributed to the Purcell suppression F_P the ions experience in the ridge waveguide geometry. Improvements to the measurement technique to extract Γ_h allowed for the measurement of a (power-broadened) homogeneous linewidth below 10 kHz, approaching the lifetime limit of $\sim$ 0.5 kHz. Measuring the homogeneous linewidth as a function of the crystal temperature allowed for identifying the Orbach process as the dominant spin-lattice relaxation mechanism. For a better understanding of the erbium site symmetry the Zeeman-splitting of the main sites was investigated. I was able to identify spin-selective optical transitions which are essential when building a spin-photon interface. Subsequent investigation of the Zeeman-splitting for different magnetic field directions reveals highly anisotropic g-tensors and different g-values for the main erbium sites. Finally, this information was used to measure a preliminary spin-lifetime of several milliseconds.

In the third sample generation, I used a high-purity float-zone silicon-on-insulator wafer and fabricated low-loss rib waveguides. These waveguides contained erbium in natural abundance and were post-implantation annealed at 500 °C. Resonant spectroscopy experiments revealed the same main sites with similar physical properties as in the second-generation samples. This shows that the developed fabrication technique is capable of generating deterministic erbium sites with well-defined properties for different silicon substrates, a capability which has not been demonstrated in Er^{3+}:Si so far. Optical excited-state lifetimes of 0.186 ms and 0.142 ms for sites *A* and *B* were found. This lifetime corresponds to the emitter lifetime in bulk silicon, as due to the waveguide geometry no significant change of the emitters' lifetime is expected. The latter was shown by calculating the Purcell factor distribution in the rib waveguide geometry where $F_P \approx 1$ everywhere in the waveguide. In addition, I implemented another technique of measuring the homogeneous linewidth which recovers the narrow homogeneous linewidths establishing the developed technique as a standard tool for upper bounding Γ_h. Values smaller than $\Gamma_h = 160$ kHz were observed in the third sample generation, limited by power broadening of the homogeneous line. This result is in agreement with data obtained using the EOM measurement scheme developed in this work. Finally, I did investigate the effect of erbium concentration and annealing temperature on the inhomogeneous linewidth. The annealing temperature is found to be a key parameter in generating deterministic sites. At high erbium concentrations, an annealing temperature of 600 °C leads to a four-fold reduction of the inhomogeneous linewidth suggesting improved erbium integration into the silicon matrix yielding potentially large optical depths.

Outlook

This section provides an outlook for future experiments and potential improvements to the work presented in this thesis.
As a first step, the overall length of the waveguides might be further increased which opens prospects for better signal-to-noise ratios. Additionally, selecting a single erbium isotope for implantation only, as well as optimized annealing procedures should facilitate a better understanding of the effect of the isotopic shift on the inhomogeneous linewidth. First experiments on ^{170}Er in CZ silicon suggest an isotopic shift of a few hundred megahertz which would match my observation of the double-peak shaped, inhomogeneously broadened line in chapter 6. Another approach is the incorporation of erbium ions into an optical resonator. Record-high Q-factors of 11 million have been reported in silicon nanophotonic cavities [153] making the implantation of erbium into such cavities highly promising. The latest data obtained in our group suggests that this approach is capable of isolating the emission of single erbium ions which opens prospects for future single-ion spin-photon interfaces.
Another direction for improvement is the fiber-to-chip coupling. For the tapered fiber approach, capped tapered fiber tips [154] and underetched waveguides should facilitate coupling efficiencies larger than 50% making the light-matter interface more deterministic. For upscaling the use of fiber arrays is promising [155] as this allows simultaneous coupling to many waveguides at the same time which is especially interesting for silicon photonic circuitry [156, 157].
In addition, the application of microwave fields should give control over the electronic population of ground and excited ensemble spin levels which might be used later on to apply dynamical decoupling sequences. These techniques were already successfully employed in ensembles of Er:YSO [158, 159] and the additional control is important for many quantum memory protocols where megahertz separated transitions are essential. Following the application of microwaves to Er^{3+}:Si , another possible working direction is the use of rare-earth ions for microwave-to-optical (M2O) conversion [160], where especially erbium is a promising candidate due to its emitting frequency at telecom wavelengths [92, 134, 161]. Taking one step further, a future M2O-device based on Er^{3+}:Si might be used to interface superconducting qubits and telecom photons on the same chip, as silicon is the standard substrate material for superconducting circuits [162].
Another direction to pursue is the reduction of magnetic noise due to nuclear spins present in silicon. This can be achieved using optimized silicon substrates composed of ^{28}Si only, improving the coherence of an incorporated qubit [163, 164].
There are several figures of merit when characterizing a quantum memory, i.e., storage time, multiplexing capabilities, and bandwidth and there exists a plethora of quantum memory protocols involving rare-earth doped crystals [165, 166, 167]. Demonstration of such protocols using the Er^{3+}:Si platform is a task left for future work.

Appendix A

Process documentation

A.1 Fabrication of tapered fibers

I follow the method of [104] for fabricating single-sided, conical fiber tips. The idea is to use concentrated hydrofluoric acid (HF) to dissolve the SiO_2 of the glass fiber while slowly decreasing the HF fluid level in the etching vessel. This dynamical etching process leads to the formation of sharp fibers tips which I then used to couple to the waveguides. For this process I use SMF-28 fibers which are cleaved, stripped, cleaned with isopropanol and dipped into a suited etching vessel.
The fibers' tip angle α can be calculated using

$$\alpha = 2 \times \arctan\left(\frac{c}{v}\right)$$

where c is the HF (50%) etching rate and v the speed of the fluid level decreasing in the vessel. The etching rate is 2.77 µm/min measured beforehand. I target a tip angle of 3° which yields a fluid level change speed of 106 µm/min. The change in HF per time depends in the vessel size. I use a PMMA beaker with a radius $r = 36.5\,\text{mm}$ and height $h = 44\,\text{mm}$. The flow rate $\mathrm{d}Vol/\mathrm{d}t$ can then be calculated using

$$\frac{\mathrm{d}Vol}{\mathrm{d}t} = v \times r^2 \times \pi.$$

In addition to the HF, I use a layer of silicone oil on top as a protective layer in a roughly 3:1 ratio of HF to oil. 80 mL of HF and 25 mL of oil on top is used. The flow rate used is $\mathrm{d}Vol/\mathrm{d}t = 0.264\,\text{mL/min}$ which is pumped from the bottom of the etching vessel using a syringe pump (LA-100, RS232). Assuming a fiber diameter of 125 µm the total etching time is 23 min. However, I observed significantly better results for an etching time of 37 min. This can be due to HF slowly diffusing into the oil film, creating an etching gradient with a significantly lower etching rate than the pure acid. In addition, the process is highly susceptible to temperature and age of the acid. The latter two parameters are also the reason for the variation in the achieved fiber tip angles α typically ranging from 3°-5°. After etching the fibers are dipped in isopropyl alcohol for rinsing as it exhibits a low surface tension thus avoiding damage to the fragile fiber tips.

A.2 Nanofabrication

Wafers

- 200 mm CZ silicon on insulator wafers are purchased from Silicon Valley Microelectronic Inc. and University Wafer Inc.
- 75 mm FZ silicon on insulator wafers are purchased from Ultrasil corp.
- Dicing performed at Fraunhofer EMFT along the <110> wafer direction in 10x10 mm chips.
- Secondary ion mass spectrometer (SIMS) analysis from RTG Mikroanalyse GmbH, Berlin

Implantation

- CZ implantation performed at Fraunhofer IISB in Erlangen, Germany.
- CVD implantation performed at Ion Beam Services in Peynier, France.
- FZ implantation performed at Helmholtz-Zentrum in Dresden-Rossendorf, Germany.

Post-implantation annealing

- If the erbium implantation was performed at room temperature, subsequent rapid-thermal annealing at temperature T_{anneal} is necessary.
- The implanted samples are placed on a silicon wafer in an rapid thermal annealing oven under N_2 atmosphere at 1.33 mbar.
- Ramp rate from 20 °C to T_{anneal} is 2.8 °C/s.
- The sample is kept at T_{anneal} for 600 s for CZ samples and 60 s for FZ samples. The temperature is controlled by a PID using a thermocouple close to the sample.
- T_{anneal} is 700 °C for CZ samples and 500 °C for FZ samples unless stated otherwise.
- The cooldown rate cannot be controlled precisely in this oven due to limited cooling power. Typically, the sample reaches 40 °C after 60 min with an intial cooldown rate of $\sim$ 7 °C/s.

Sample preparation

- Sonicate single SOI chip first in acetone and then isopropanol at high power for 3 min each at 30 °C. Blow dry using a N_2 gun.
- Transfer sample into plasma asher and clean the surface using oxygen plasma, RF power = 400 W, O_2 flow= 75 sccm, pressure = 75 Pa for 4 min.

- Spin coat (~ 5°C) ZEP-520A (ZEON Corp.) onto the chip with 4000 rpm for 120 s using an acceleration ramp of 2000 rpm/s. Subsequent softbacking at 180 °C for 180 s to evaporate solvent residues.
- Check target resist thickness of ~ 420 nm using laser ellipsometer or microscope reflectometer. Final check of the surface using optical microscope for dust particles.

Electron beam lithography

- NB5 machine at Walter-Meissner-Institute
- Pattern files are optimized using BEAMER (GenISys GmbH)
- Fixed acceleration voltage of 80 kV using a current of 2.0 - 3.0 nA yielding a dose of 2.0 - 3.0 C/m^2 (200 - 300 $\mu C/cm^2$)

Development

- Immerse the chip in ZED-N50 (n-Amyl acetate) (~ 5 °C). The developer is located on a cold plate keeping the liquid at ~ 5 °C. Gently immerse and stir the chip.
- Transfer the chip into (~ 5 °C) rinser/stopper(ZMD-B (methyl isobutyl ketone (MIBK) 89%, isopropyl alcohol 11%)) for 10 s and stir.
- Blow dry using N_2 and subsequent hardbake at 140 °C for 180 s.

Reactive ion etching

- Plasma Oxford RIE 80 at ZNN, TU München
- Use Fomblin for thermal contact to Si backwafer
- Set temperature to −100 °C and use the following gases: SF_6 with flow = 6.6 sccm; O_2 with flow = 1 sccm; Ar with flow = 29 sccm; pressure = 4 mTorr, CCP ("forward") power = 10 W and ICP power = 0 W (RIE mode)
- Total etching time is 430 s for an etch depth of ~ 220 nm

Resist stripping

- Boil chip in ~ 100 °C ZDMAC (N,N-dimethylacetamide) for 12 min.
- Sonicate chip in ZDMAC at 50 °C and medium power for 10 min.
- Subsequent sonicating of the chip in Acetone at 50 °C and low power for 5 min.
- Subsequent sonicating of the chip in Isopropanol at 50 °C and low power for 2 min.
- Blow dry using N_2 gun and perform plasma ashing using oxygen plasma, RF power = 400 W, O_2 flow= 75 sccm, pressure = 75 Pa for 4 min.

Appendix B

Additional data

B.1 Design of a broadband photonic crystal mirror

Here I provide additional data on the mirror design used in the ridge waveguide geometry. The mirror is designed as a broadband device reflecting light in the wavelength regime from 1.5 µm to 1.6 µm. The initial design consists of a set of 20 identical, elliptical holes described by the major axis $h_y = 0.3$ µm and the minor axis $h_x = 0.1$ µm. The hole distance i.e. the lattice constant is fixed to 0.33 µm and the waveguide width is 0.7 µm. In Fig. B.1 the reflectivity (denoted as normalized flux on the y-axis) of a photonic crystal (PhC) mirror with the above parameters is shown for a silicon waveguide in vacuum. The high-reflectivity window ranges from 1.4-1.6 µm and is thus centered around 1.53 µm where the Er^{3+} fluorescence occurs. The nanofabrication of the waveguides containing PhCs with such hole dimensions is very challenging. For estimating the acceptable error margin of the hole sizes the mirror reflectivity is simulated for different hole diameters. A large parameter sweep is performed where both the hole size and the waveguide width are scanned in the mirror reflectivity simulation. Additionally, the buried oxide layer below the waveguide structure is included in the simulation. The results are shown in Fig. B.2 where in a) the waveguide width and b) the PhC mirror hole diameter is scanned as a function of the wavelength.

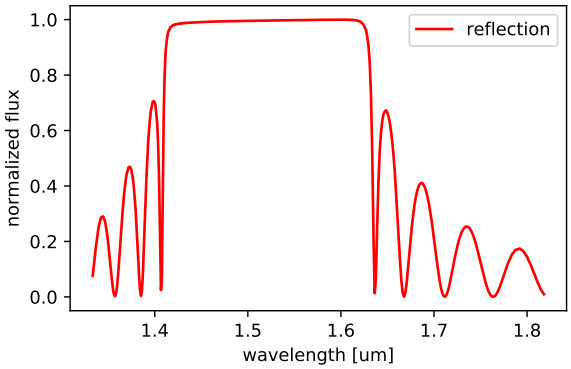

FIGURE B.1: Reflectivity of final PhC mirror design

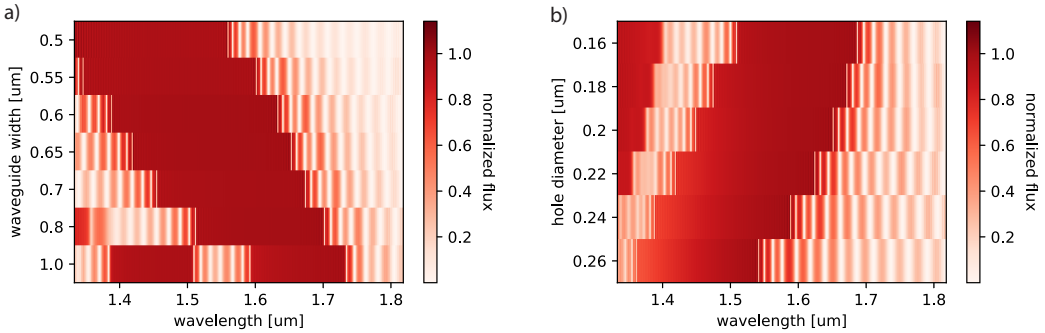

FIGURE B.2: FDTD simulations of PhC mirrors

I see from both plots that the error margin is comparably high since the large reflectivity band is maintained for hole size deviations of $\sim 100\,\text{nm}$. Also the waveguide widths effect on the mirrors' properties are negligible for widths smaller than 700 nm as the large reflectivity is maintained in the relevant wavelength region for our application. These simulations were done by Andreas Gritsch.

B.2 Summarizing measured values of peaks 1-9 in the CZ sample

Here, the measured values of the inhomogeneous linewidth, the optical lifetime and the homogeneous linewidth of peaks 1-9 in the CZ samples are documented.

Inhomogeneous broadening

Peak number	Inhom. linewidth (FWHM)
1	3.6(2) GHz
2	1.2(1) GHz
3	1.3(2) GHz
4	1.72(3) GHz
5	3.9(6) GHz
6	2.39(4) GHz
7	3.2(3) GHz
8	2.2(1) GHz
9	2.1(2) GHz

TABLE B.1: The inhomogeneous linewidths Γ_{inh} (FWHM) of all fluorescence lines found are documented in this table.

Optical lifetime

Peak number	Optical lifetime
1	0.85(1) ms
2	1.03(1) ms
3	0.89(1) ms
4	0.936(2) ms
5	0.87(2) ms
6	0.978(3) ms
7	0.897(7) ms
8	0.988(6) ms
9	0.92(1) ms

TABLE B.2: The optical lifetimes of the found fluorescence lines are documented here.

Homogeneous linewidth

Peak number	Homogeneous linewidth (FWHM)
1	44(10) MHz
2	65(12) MHz
3	78(18) MHz
4	88(2) MHz
5	110(19) MHz
6	109(4) MHz
7	103(9) MHz
8	108(15) MHz
9	45(19) MHz

TABLE B.3: All extracted homogeneous linewidth values of the sites found are summarized here.

B.3 Erbium implantation and SIMS analysis of Czochralski-(Cz) grown Er^{3+}:Si

Implantation parameter

The implantation was done at Fraunhofer IISB in Erlangen, where erbium in natural abundance was implanted. Two runs with different dose were used yielding low and high dose implanted chips. Each implantation step consisted of a single implantation run as summarized in table B.4 at room temperature. The implantated concentration is 100 fold lower than expected due to sparking in the ion source during implantation.

	Energy	Dose
Low dose	198keV	1E12 cm^{-2}
High dose	198keV	1E14 cm^{-2}

TABLE B.4: CZ silicon implantation parameters

Erbium implantation profile

Note that the trace for ^{166}Er and ^{170}Er was superimposed by a background signal of unknown origin in the SIMS apparatus thus the seemingly homogeneous depth profile. The other erbium traces show an approximate Gaussian profile which is expected when using a single implantation run. The calibration of the concentration was done with the erbium implanted float-zone (FZ) samples as a reference. The data for all erbium isotopes are shown in Fig. B.3.

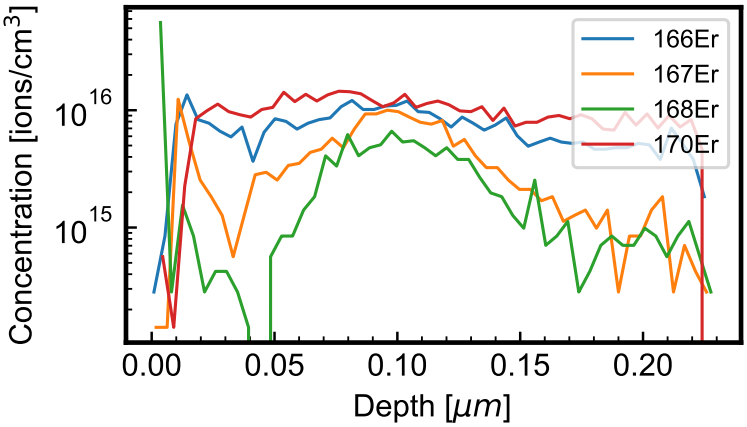

FIGURE B.3: **Erbium implantation profile.** The SIMS measurement shows a Gaussian and homogeneous distribution of the different implanted erbium isotopes in the silicon device layer.

Impurity analysis

To estimate the impurity concentrations another SIMS analysis is employed, where the concentration of oxygen, hydrogen and carbon is measured. The data is shown in Fig. B.4. The impurity concentration gradually decreases for increasing depths and rises sharply when reaching the buried SiO_2 layer. The drop at the beginning can either be caused by impurities in the crystal, or on its surface. Therefore it is not possible to distinguish the two without a clean reference sample. Thus, only the concentration in a depth larger than $\sim$ 100 nm may be meaningful. This issue applies also for the CVD samples. Still, the impurity concentrations are typical for Czochralski-grown silicon.

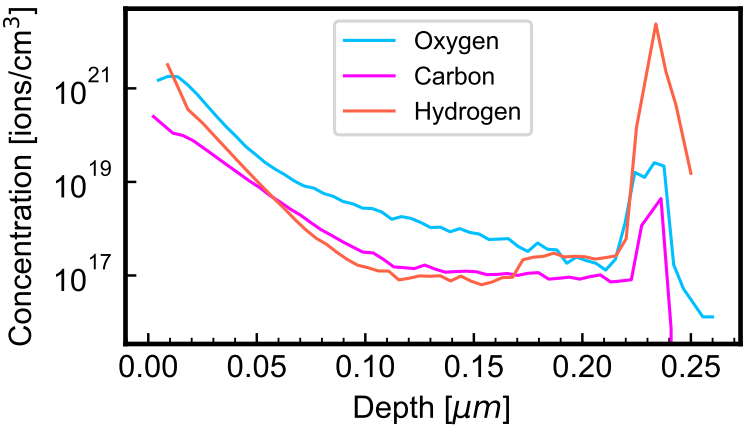

FIGURE B.4: **Impurity profiles CZ silicon.** SIMS measurement of oxygen, carbon and hydrogen in the CZ silicon sample.

B.4 Erbium implantation and SIMS analysis of chemical-vapor deposition-(CVD) grown Er^{3+}:Si

Implantation parameter

The implantation was done at Ion Beam Services in Peynier, where isotope selective ^{167}Er and ^{170}Er were implanted. Two runs with different doses were used yielding low and high-dose implanted chips. Only the low dose samples were used in this work. Each implantation step consisted of four implantation runs as summarized in table B.5. The implantation was carried out with the silicon substrate heated to 500 °C during implantation and tilted by an angle of 7°.

	Isotope	Energy	Dose
Low dose	^{167}Er	350keV	1,00E12 cm^{-2}
	^{167}Er	100keV	0,45E12 cm^{-2}
	^{170}Er	350keV	1,00E12 cm^{-2}
	^{170}Er	100keV	0,45E11 cm^{-2}
High dose	^{167}Er	350keV	1,00E13 cm^{-2}
	^{167}Er	100keV	4,5E12 cm^{-2}
	^{170}Er	350keV	1,00E13 cm^{-2}
	^{170}Er	100keV	4,5E11 cm^{-2}

TABLE B.5: CVD silicon implantation parameters

Erbium implantation profile

The erbium implantation profiles of the CVD chips with all erbium isotopes are shown in Fig. B.5. The spike at the sample surface is a measurement artifact either due to impurities on the surface or ion beam-induced diffusion processes. The erbium ions are distributed homogeneously in the silicon device layer. The traces of

^{170}Er ^{166}Er and ^{168}Er are again superimposed by a background signal of unknown origin. The calibration of the concentration was done with the erbium implanted float-zone (FZ) samples as a reference.

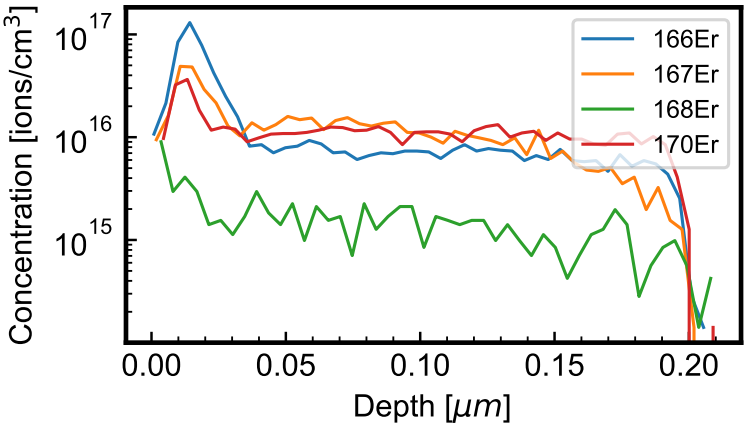

FIGURE B.5: **Erbium implantation profile.** The SIMS measurement shows a homogeneous distribution of the different implanted erbium isotopes in the silicon device layer due to the two-step implantation with different energies.

Impurity analysis

To measure the concentration of oxygen, hydrogen, and carbon present in the CVD sample another SIMS measurement was performed. The measurement data is shown in Fig. B.6. As expected the impurity concentration gradually decreases for increasing depths. The concentration of oxygen is slightly higher in the CVD-grown sample. Again the concentrations rise sharply when reaching the buried oxide layer. The impurity concentrations are comparable to the Czochralski-grown silicon but the oxygen concentration is slightly larger here.

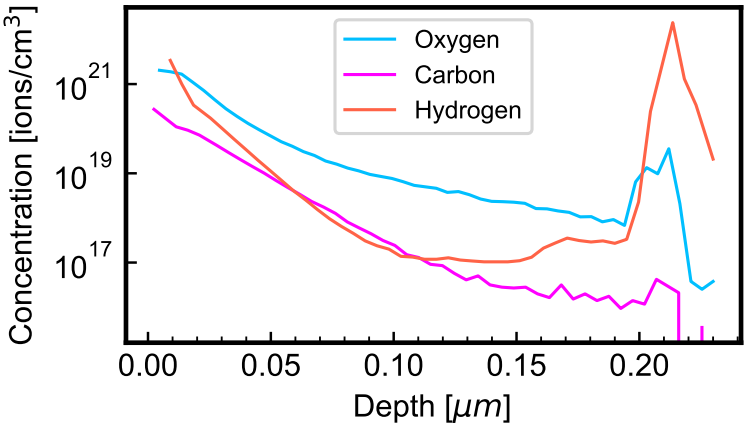

FIGURE B.6: **Impurity profiles of CVD silicon.** SIMS measurement of oxygen, carbon, and hydrogen in the CVD silicon sample.

B.5 Erbium implantation and SIMS analysis of float-zone (FZ) grown Er^{3+}:Si

Implantation parameter

The implantation was carried out at Helmholtz-Zentrum Dresden-Rossendorf, where erbium in natural abundance was implanted using a Tandetron accelerator. Two runs with different doses were used yielding low- and high-dose implanted chips. Each implantation step consisted of three implantation runs as summarized in table B.6. The implantation was carried out with the silicon substrate temperature kept at 20 °C and tilted by an angle of 7° to avoid channeling.

	Energy	Fluence
Low dose	1500keV	4,00E11 cm^{-2}
	2500keV	6,00E11 cm^{-2}
	4000keV	1,00E12 cm^{-2}
High dose	4000keV	4,00E12 cm^{-2}
	2500keV	6,00E12 cm^{-2}
	2500keV	1,00E13 cm^{-2}

TABLE B.6: FZ silicon implantation parameters

Erbium implantation profile

The erbium implantation profile of the FZ chips with all erbium isotopes is shown in Fig. B.7. The erbium ions are distributed homogeneously between 0.5 µm and 1.5 µm in the silicon device layer. The ^{170}Er trace is superimposed by a background of unknown origin preventing a successful measurement.

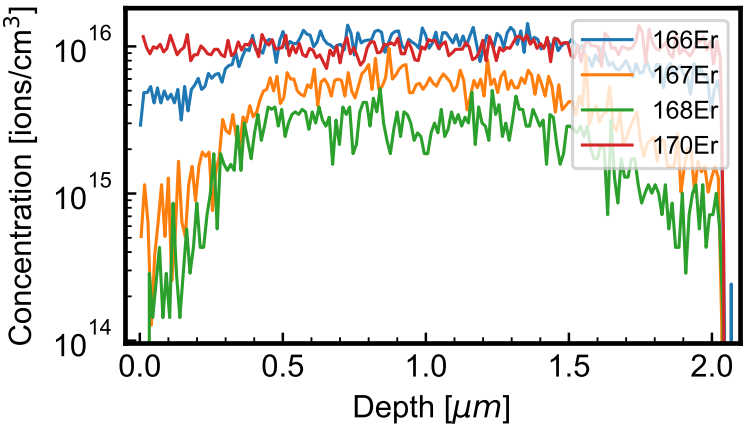

FIGURE B.7: **Erbium implantation profile.** The three-step implantation run did yield a deep and homogeneous distribution of the different implanted erbium isotopes in the silicon device layer.

B.6 Tilted magnetic field measurements of site *A* and *P*

The tilted magnetic field measurements presented in chapter 6.15 are extended to sites A and P. In Fig. B.8 the maps for site A are shown for rotation angles $0 - 25°$. At 1535.96 nm an excited state crystal field of site P is superimposing the spin-flip transitions at ~ 100 mT} making analysis difficult on that part of the scan. However, a Zeeman-splitting, comparable to site B, is visible. Also, the spin-flip and spin-preserving lines are clearly distinguishable. The number of lines increases for increasing tilt angles and is maximal for $\varphi = 15°$. A large amount of narrow fluorescence lines indicates again the g-tensors anisotropy in both ground and excited states. To fully resolve the spin-preserving lines in the center a larger magnetic field would be necessary.

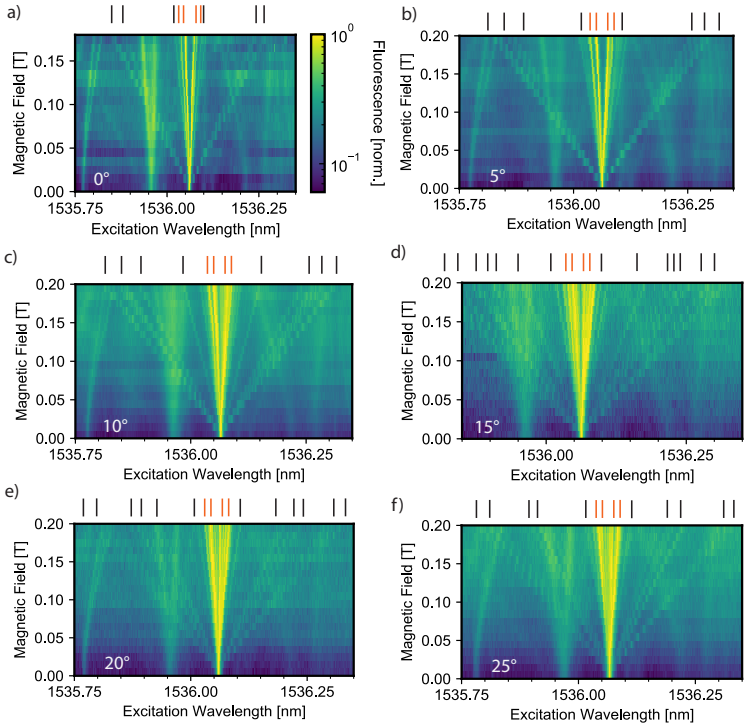

FIGURE B.8: **Tilted magnetic field site *A*.** Zeeman-splitting of site A for varying tilt angles a)-f). The fluorescence amplitudes are normalized to one and the color scale in a) applies to all scans in this figure. The sample temperature was 14 K in these measurements.

A different picture emerges when investigating the Zeeman-splitting of site P. As discussed in the main text, site P is a site containing more than one erbium ion and thus features different physical properties compared to the main sites A and B. In Fig. B.9 a) the Zeeman-splitting for $\varphi = 0°$ is shown. At 1538.17 nm and zero magnetic field a ground-state CF level of the optical site is visible which splits into four lines i.e. two spin-flip and two spin-preserving lines when increasing $|\mathbf{B}|$. At 1538.27 nm and zero magnetic field, site P is located. When increasing the magnetic field, only the centered lines start to fan out and their splitting is much less compared to sites A and B. This indicates a smaller effective g-factor compared to the other two

sites. Note that in the measurement for $\varphi = 0°$ the sample was accidentally kept at a temperature of 8 K instead of 14 K which might have affected the visibility of the spin-flip transitions. However, the expected spin-lifetime is expected to much shorter compared to the ones of sites A and B due to the smaller crystal field splitting. Thus this discrepancy in temperature should only have a negligible effect here. For the remaining measurements in panels b) to f) the sample temperature was 14 K. Upon increasing the rotation angle a splitting of the lines can be identified and also the differences in the fluorescence amplitudes for spin-preserving and spin-flip lines are now visible. But again a larger magnetic field would be required to assign each spin-dependent transition. When investigating the measurement for $\varphi = 25°$ in panel Fig. B.9 b) closer the levels are bending towards longer wavelengths which might be due to the special nature of the pair site P.

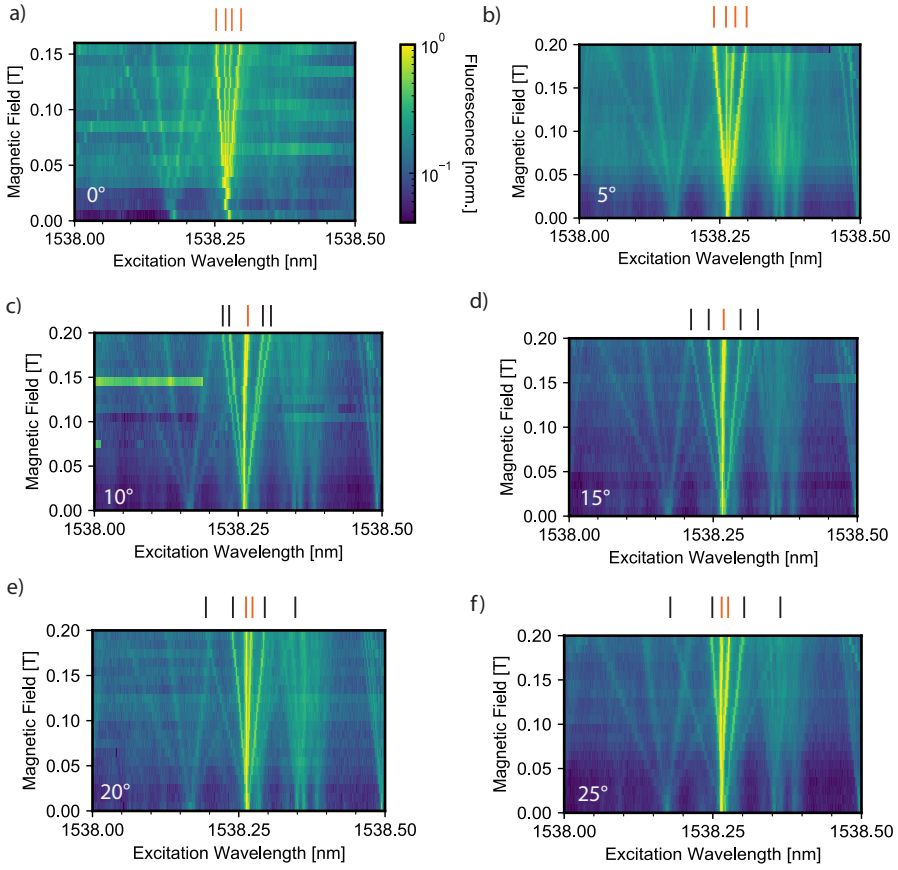

FIGURE B.9: **Tilted magnetic field site *P*.** Zeeman-splitting of site P for varying rotation angles a)-f). The fluorescence amplitudes are normalized to one and the color scale in a) applies to all scans in this figure. The sample temperature in a) was 8 K and 14 K in measurements b)-f).

List of Figures

List of Tables

Bibliography

[1] Frank Arute et al. "Quantum Supremacy Using a Programmable Superconducting Processor". *Nature* **574** (2019), pp. 505–510.

[2] Zhong Han-Sen et al. "Quantum Computational Advantage Using Photons". *Science* **370** (2020), pp. 1460–1463.

[3] H. J. Kimble. "The Quantum Internet". *Nature* **453** (2008), pp. 1023–1030.

[4] Wehner Stephanie, Elkouss David, and Hanson Ronald. "Quantum Internet: A Vision for the Road Ahead". *Science* **362** (2018), eaam9288.

[5] Nicolas Gisin et al. "Quantum Cryptography". *Rev. Mod. Phys.* **74** (2002), pp. 145–195.

[6] C. Monroe et al. "Large-Scale Modular Quantum-Computer Architecture with Atomic Memory and Photonic Interconnects". *Phys. Rev. A* **89** (2014), p. 022317.

[7] Daniel Gottesman, Thomas Jennewein, and Sarah Croke. "Longer-Baseline Telescopes Using Quantum Repeaters". *Phys. Rev. Lett.* **109** (2012), p. 070503.

[8] E. T. Khabiboulline et al. "Optical Interferometry with Quantum Networks". *Phys. Rev. Lett.* **123** (2019), p. 070504.

[9] Timothy J. Proctor, Paul A. Knott, and Jacob A. Dunningham. "Multiparameter Estimation in Networked Quantum Sensors". *Phys. Rev. Lett.* **120** (2018), p. 080501.

[10] Tobias Schmitt-Manderbach et al. "Experimental Demonstration of Free-Space Decoy-State Quantum Key Distribution over 144 Km". *Phys. Rev. Lett.* **98** (2007), p. 010504.

[11] Sebastian Nauerth et al. "Air-to-Ground Quantum Communication". *Nature Photonics* **7** (2013), pp. 382–386.

[12] Sheng-Kai Liao et al. "Satellite-to-Ground Quantum Key Distribution". *Nature* **549** (2017), pp. 43–47.

[13] B. Hensen et al. "Loophole-Free Bell Inequality Violation Using Electron Spins Separated by 1.3 Kilometres". *Nature* **526** (2015), pp. 682–686.

[14] Andreas Reiserer and Gerhard Rempe. "Cavity-Based Quantum Networks with Single Atoms and Optical Photons". *Rev. Mod. Phys.* **87** (2015), pp. 1379–1418.

[15] Rüdiger Paschotta. *Article on 'optical Fiber Communications' in the Encyclopedia of Laser Physics and Technology*. 1st ed. Wiley-VCH, 2008.

[16] Lines M. E. “The Search for Very Low Loss Fiber-Optic Materials”. *Science* **226** (1984), pp. 663–668.

[17] W. K. Wootters and W. H. Zurek. “A Single Quantum Cannot Be Cloned”. *Nature* **299** (1982), pp. 802–803.

[18] W. Tittel et al. “Photon-Echo Quantum Memory in Solid State Systems”. *Laser & Photonics Reviews* **4** (2010), pp. 244–267.

[19] H.-J. Briegel et al. “Quantum Repeaters: The Role of Imperfect Local Operations in Quantum Communication”. *Phys. Rev. Lett.* **81** (1998), pp. 5932–5935.

[20] M. ŻŻukowski et al. ““Event-ready-detectors” Bell Experiment via Entanglement Swapping”. *Phys. Rev. Lett.* **71** (1993), pp. 4287–4290.

[21] C. Simon et al. “Quantum Memories”. *The European Physical Journal D* **58** (2010), pp. 1–22.

[22] Klemens Hammerer, Anders S. Sørensen, and Eugene S. Polzik. “Quantum Interface between Light and Atomic Ensembles”. *Rev. Mod. Phys.* **82** (2010), pp. 1041–1093.

[23] M. D. Lukin. “Colloquium: Trapping and Manipulating Photon States in Atomic Ensembles”. *Rev. Mod. Phys.* **75** (2003), pp. 457–472.

[24] Nicolas Sangouard et al. “Quantum Repeaters Based on Atomic Ensembles and Linear Optics”. *Rev. Mod. Phys.* **83** (2011), pp. 33–80.

[25] C. H. van der Wal et al. “Atomic Memory for Correlated Photon States”. *Science* **301** (2003), pp. 196–200.

[26] A. Kuzmich et al. “Generation of Nonclassical Photon Pairs for Scalable Quantum Communication with Atomic Ensembles”. *Nature* **423** (2003), pp. 731–734.

[27] Kutlu Kutluer, Margherita Mazzera, and Hugues de Riedmatten. “Solid-State Source of Nonclassical Photon Pairs with Embedded Multimode Quantum Memory”. *Phys. Rev. Lett.* **118** (2017), p. 210502.

[28] Cyril Laplane et al. “Multimode and Long-Lived Quantum Correlations between Photons and Spins in a Crystal”. *Phys. Rev. Lett.* **118** (2017), p. 210501.

[29] Benjamin Merkel, Alexander Ulanowski, and Andreas Reiserer. “Coherent and Purcell-Enhanced Emission from Erbium Dopants in a Cryogenic High-Q Resonator”. *Phys. Rev. X* **10** (2020), p. 041025.

[30] G. D. Fuchs et al. “A Quantum Memory Intrinsic to Single Nitrogen–Vacancy Centres in Diamond”. *Nature Physics* **7** (2011), pp. 789–793.

[31] Lachlan J. Rogers et al. “All-Optical Initialization, Readout, and Coherent Preparation of Single Silicon-Vacancy Spins in Diamond”. *Phys. Rev. Lett.* **113** (2014), p. 263602.

[32] Shuo Sun et al. “A Single-Photon Switch and Transistor Enabled by a Solid-State Quantum Memory”. *Science* **361** (2018), pp. 57–60.

[33] Andreas Reiserer. “Cavity-Enhanced Quantum Network Nodes”. Habilitation. Technical University of Munich, 2021.

[34] Rose Brendon C. et al. “Observation of an Environmentally Insensitive Solid-State Spin Defect in Diamond”. *Science* **361** (2018), pp. 60–63.

[35] Sebastian Zaske et al. “Visible-to-Telecom Quantum Frequency Conversion of Light from a Single Quantum Emitter”. *Phys. Rev. Lett.* **109** (2012), p. 147404.

[36] Anaïs Dréau et al. “Quantum Frequency Conversion of Single Photons from a Nitrogen-Vacancy Center in Diamond to Telecommunication Wavelengths”. *Phys. Rev. Applied* **9** (2018), p. 064031.

[37] M. Lipson. “Guiding, Modulating, and Emitting Light on Silicon-challenges and Opportunities”. *Journal of Lightwave Technology* **23** (2005), pp. 4222–4238.

[38] Wim Bogaerts et al. “Programmable photonic circuits”. *Nature* **586** (2020), pp. 207–216.

[39] Sacha Welinski et al. “Coherence Time Extension by Large-Scale Optical Spin Polarization in a Rare-Earth Doped Crystal”. *Phys. Rev. X* **10** (2020), p. 031060.

[40] Manjin Zhong et al. “Optically Addressable Nuclear Spins in a Solid with a Six-Hour Coherence Time”. *Nature* **517** (2015), pp. 177–180.

[41] Miloš Rančić et al. “Coherence Time of over a Second in a Telecom-Compatible Quantum Memory Storage Material”. *Nature Physics* **14** (2018), pp. 50–54.

[42] Le Dantec Marianne et al. “Twenty-Three–Millisecond Electron Spin Coherence of Erbium Ions in a Natural-Abundance Crystal”. *Science Advances* **7** (2021), eabj9786.

[43] Lorenz Weiss et al. “Erbium Dopants in Nanophotonic Silicon Waveguides”. *Optica* **8** (2021), pp. 40–41.

[44] Andreas Gritsch et al. “Narrow Optical Transitions in Erbium-Implanted Silicon Waveguides”. *arXiv e-prints* (2021), arXiv:2108.05120.

[45] A. J. Freeman and R. E. Watson. “Theoretical Investigation of Some Magnetic and Spectroscopic Properties of Rare-Earth Ions”. *Phys. Rev.* **127** (1962), pp. 2058–2075.

[46] G. H. Dieke and H. M. Crosswhite. “The Spectra of the Doubly and Triply Ionized Rare Earths”. *Appl. Opt.* **2** (1963), pp. 675–686.

[47] A. J. Kenyon. “Erbium in Silicon”. *Semiconductor Science and Technology* **20** (2005), R65–R84.

[48] C. W. Thiel, Thomas Böttger, and R. L. Cone. “Rare-Earth-Doped Materials for Applications in Quantum Information Storage and Signal Processing”. *Journal of Luminescence* **131** (2011), pp. 353–361.

[49] Guokui Liu and Bernard Jacquier. *Spectroscopic Properties of Rare Earths in Optical Materials*. Springer Series in Materials Science. Springer, 2005.

[50] H. Przybylinska et al. “Optically Active Erbium Centers in Silicon”. *Phys. Rev. B* **54** (1996), pp. 2532–2547.

[51] A. Messiah and J. Streubel. *Albert Messiah: Quantenmechanik. Band 2*. Albert Messiah: Quantenmechanik. De Gruyter, 1985.

[52] Benjamin Merkel. “Enhancing the Emission and Coherence of Erbium Dopants”. PhD thesis. München: Technische Universität München, 2021.

[53] Tao Li et al. “Quantum Memory and Gates Using a Lambda-type Quantum Emitter Coupled to a Chiral Waveguide”. *Phys. Rev. A* **97** (2018), p. 062318.

[54] Thomas Böttger et al. “Spectroscopy and Dynamics of Er^{3+}:Y_2SiO_5 at 1.5 µm”. *Phys. Rev. B* **74** (2006), p. 075107.

[55] Thomas Böttger et al. “Effects of Magnetic Field Orientation on Optical Decoherence in Er^{3+}:Y_2SiO_5”. *Phys. Rev. B* **79** (2009), p. 115104.

[56] R. W. Equall et al. “Ultraslow Optical Dephasing in Eu^{3+}:Y_2SiO_5”. *Phys. Rev. Lett.* **72** (1994), pp. 2179–2182.

[57] R. L. Cone et al. “Rare-Earth-Doped Materials with Application to Optical Signal Processing, Quantum Information Science, and Medical Imaging Technology”. Proc.SPIE. Vol. 8272. 2012.

[58] S. J. van Enk and H. J. Kimble. “Single Atom in Free Space as a Quantum Aperture”. *Phys. Rev. A* **61** (2000), p. 051802.

[59] Evan Miyazono et al. “Coupling of Erbium Dopants to Yttrium Orthosilicate Photonic Crystal Cavities for On-Chip Optical Quantum Memories”. *Appl. Phys. Lett.* **108** (2016), p. 011111.

[60] A. M. Dibos et al. “Atomic Source of Single Photons in the Telecom Band”. *Phys. Rev. Lett.* **120** (2018), p. 243601.

[61] Mouktik Raha et al. “Optical Quantum Nondemolition Measurement of a Single Rare Earth Ion Qubit”. *Nature Communications* **11** (2020), p. 1605.

[62] Songtao Chen et al. “Parallel Single-Shot Measurement and Coherent Control of Solid-State Spins below the Diffraction Limit”. *Science* **370** (2020), pp. 592–595.

[63] Bernardo Casabone et al. “Cavity-Enhanced Spectroscopy of a Few-Ion Ensemble in Eu^{3+}:Y_2SiO_5”. *New Journal of Physics* **20** (2018), p. 095006.

[64] Tian Zhong et al. “Nanophotonic Rare-Earth Quantum Memory with Optically Controlled Retrieval”. *Science* **357** (2017), pp. 1392–1395.

[65] Jonathan M. Kindem et al. “Control and Single-Shot Readout of an Ion Embedded in a Nanophotonic Cavity”. *Nature* **580** (2020), pp. 201–204.

[66] Werner Martienssen. “Semiconductors”. *Springer Handbook of Condensed Matter and Materials Data*. Ed. by Werner Martienssen and Hans Warlimont. Berlin, Heidelberg: Springer Berlin Heidelberg, 2005, pp. 575–694.

[67] Martin Rahm, Roald Hoffmann, and N. W. Ashcroft. "Atomic and Ionic Radii of Elements 1–96". *Chemistry – A European Journal* **22** (2016), pp. 14625–14632.

[68] J. L. Rogers et al. "Erbium-doped Silicon Films Grown by Plasma-enhanced Chemical-vapor Deposition". *Journal of Applied Physics* **78** (1995), pp. 6241–6248.

[69] S. Scalese et al. "Effect of O:Er Concentration Ratio on the Structural, Electrical, and Optical Properties of Si:Er:O Layers Grown by Molecular Beam Epitaxy". *Journal of Applied Physics* **88** (2000), pp. 4091–4096.

[70] N. N. Ha et al. "Optical Gain of the 1.54 µm Emission in MBE-grown Si:Er Nanolayers". *Phys. Rev. B* **81** (2010), p. 195206.

[71] Flurin Könz et al. "Temperature and Concentration Dependence of Optical Dephasing, Spectral-Hole Lifetime, and Anisotropic Absorption in Eu^{3+}:Y_2SiO_5". *Phys. Rev. B* **68** (2003), p. 085109.

[72] A. Polman. "Erbium Implanted Thin Film Photonic Materials". *Journal of Applied Physics* **82** (1997), pp. 1–39.

[73] Jung H. Shin et al. "Luminescence Quenching in Erbium-doped Hydrogenated Amorphous Silicon". *Appl. Phys. Lett.* **68** (1996), pp. 997–999.

[74] J. Michel et al. "Impurity Enhancement of the 1.54 µm Er^{3+} Luminescence in Silicon". *Journal of Applied Physics* **70** (1991), pp. 2672–2678.

[75] R.K. Willardson et al. *Oxygen in Silicon*. ISSN. Elsevier Science, 1994.

[76] George D. Watkins. "Intrinsic Point Defects in Semiconductors 1999". *Materials Science and Technology*. John Wiley & Sons, Ltd, 2013.

[77] R.C. Newman. "Light Impurities and Their Interactions in Silicon". *C,H,N and o in Si and Characterization and Simulation of Materials and Processes*. Ed. by A. BORGHESI et al. European Materials Research Society Symposia Proceedings. Oxford: Elsevier, 1996, pp. 1–12.

[78] H. Ennen et al. "1.54 µm Luminescence of Erbium-implanted III-V Semiconductors and Silicon". *Appl. Phys. Lett.* **43** (1983), pp. 943–945.

[79] N. Q. Vinh et al. "Microscopic Structure of Er-Related Optically Active Centers in Crystalline Silicon". *Phys. Rev. Lett.* **90** (2003), p. 066401.

[80] Chunming Yin et al. "Optical Addressing of an Individual Erbium Ion in Silicon". *Nature* **497** (2013), pp. 91–94.

[81] John D. Joannopoulos et al. "Photonic Crystals: Molding the Flow of Light - Second Edition". 2008.

[82] John David Jackson. *Classical Electrodynamics*. 3rd ed. New York, NY: Wiley, 1999.

[83] M. M. Sigalas et al. "Effect of the Magnetic Permeability on Photonic Band Gaps". *Phys. Rev. B* **56** (1997), pp. 959–962.

[84] J.P. Boyd. *Chebyshev and Fourier Spectral Methods: Second Revised Edition*. Dover Books on Mathematics. Dover Publications, 2001.

[85] Z. Bai et al. *Templates for the Solution of Algebraic Eigenvalue Problems: A Practical Guide*. Software, Environments and Tools. Society for Industrial and Applied Mathematics, 2000.

[86] A. Taflove and S.C. Hagness. *Computational Electrodynamics: The Finite-Difference Time-Domain Method*. Artech House Antennas and Propagation Library. Artech House, 2005.

[87] Steven G. Johnson and J. D. Joannopoulos. "Block-Iterative Frequency-Domain Methods for Maxwell's Equations in a Planewave Basis". *Opt. Express* **8** (2001), pp. 173–190.

[88] Lumerical Inc. *FDTD: 3D Electromagnetic Simulator*.

[89] Ardavan F. Oskooi et al. "Meep: A Flexible Free-Software Package for Electromagnetic Simulations by the FDTD Method". *Computer Physics Communications* **181** (2010), pp. 687–702.

[90] Peter Lodahl, Sahand Mahmoodian, and Søren Stobbe. "Interfacing Single Photons and Single Quantum Dots with Photonic Nanostructures". *Rev. Mod. Phys.* **87** (2015), pp. 347–400.

[91] J. P. Hadden et al. "Integrated Waveguides and Deterministically Positioned Nitrogen Vacancy Centers in Diamond Created by Femtosecond Laser Writing". *Opt. Lett.* **43** (2018), pp. 3586–3589.

[92] John G. Bartholomew et al. "On-Chip Coherent Microwave-to-Optical Transduction Mediated by Ytterbium in YVO_4". *Nature Communications* **11** (2020), p. 3266.

[93] R Sprik, B. A. van Tiggelen, and A Lagendijk. "Optical Emission in Periodic Dielectrics". *Europhysics Letters (EPL)* **35** (1996), pp. 265–270.

[94] E.N. Economou. *Green's Functions in Quantum Physics*. Springer Series in Solid-State Sciences. Springer, 2006.

[95] Steven Johnson, Ardavan Oskooi, and Allen Taflove. *Advances in FDTD Computational Electrodynamics: Photonics and Nanotechnology*. 2013.

[96] A. J. Ward and J. B. Pendry. "Calculating Photonic Green's Functions Using a Nonorthogonal Finite-Difference Time-Domain Method". *Phys. Rev. B* **58** (1998), pp. 7252–7259.

[97] V. S. C. Manga Rao and S. Hughes. "Single Quantum-Dot Purcell Factor and beta Factor in a Photonic Crystal Waveguide". *Phys. Rev. B* **75** (2007), p. 205437.

[98] T. G. Tiecke et al. "Efficient Fiber-Optical Interface for Nanophotonic Devices". *Optica* **2** (2015), pp. 70–75.

[99] R.A. Soref, J. Schmidtchen, and K. Petermann. "Large Single-Mode Rib Waveguides in GeSi-Si and Si-on-SiO_2". *IEEE Journal of Quantum Electronics* **27** (1991), pp. 1971–1974.

[100] Florian Burger. "Silicon Photonic-Crystal Waveguides for Broadband Purcell Enhancement of Erbium Emission". M.Sc.Thesis. Technical University of Munich, 2020.

[101] Michael J. Burek et al. "Fiber-Coupled Diamond Quantum Nanophotonic Interface". *Phys. Rev. Applied* **8** (2017), p. 024026.

[102] A Sayah et al. "Fiber Tips for Scanning Near-Field Optical Microscopy Fabricated by Normal and Reverse Etching". *Ultramicroscopy* **71** (1998), pp. 59–63.

[103] Hani J. Kbashi. "Fabrication of Submicron-Diameter and Taper Fibers Using Chemical Etching". *Journal of Materials Science & Technology* **28** (2012), pp. 308–312.

[104] H. Nikbakht et al. "Fabrication of Tapered Tip Fibers With a Controllable Cone Angle Using Dynamical Etching". *Journal of Lightwave Technology* **33** (2015), pp. 4707–4711.

[105] J.D. Love et al. "Tapered Single-Mode Fibres and Devices. Part 1: Adiabaticity Criteria". *IEE Proceedings J (Optoelectronics)* **138** (1991), 343–354(11).

[106] Rüdiger Paschotta. *Article on 'Passive Fiber Optics' in the Encyclopedia of Laser Physics and Technology*. 1st ed. Wiley-VCH, 2008.

[107] Timothy P. McKenna et al. "Cryogenic Packaging of an Optomechanical Crystal". *Opt. Express* **27** (2019), pp. 28782–28791.

[108] Duan-Cheng Liu et al. *On-Demand Storage of Photonic Qubits at Telecom Wavelengths*. 2022.

[109] Lorenz Weiss et al. "Erbium Dopants in Silicon Nanophotonic Waveguides". *arXiv e-prints* (2020).

[110] B. Car et al. "Selective Optical Addressing of Nuclear Spins through Superhyperfine Interaction in Rare-Earth Doped Solids". *Phys. Rev. Lett.* **120** (2018), p. 197401.

[111] Mohsen Falamarzi Askarani et al. "Persistent Atomic Frequency Comb Based on Zeeman Sub-Levels of an Erbium-Doped Crystal Waveguide". *J. Opt. Soc. Am. B* **37** (2020), pp. 352–358.

[112] C W Thiel et al. "Rare-Earth-Doped $LiNbO_3$ and $KTiOPO_4$(KTP) for Waveguide Quantum Memories". *Journal of Physics B: Atomic, Molecular and Optical Physics* **45** (2012), p. 124013.

[113] Alan D. Bristow, Nir Rotenberg, and Henry M. van Driel. "Two-Photon Absorption and Kerr Coefficients of Silicon for 850–2200nm". *Applied Physics Letters* **90** (2007), p. 191104.

[114] H. K. Tsang et al. "Optical Dispersion, Two-Photon Absorption and Self-Phase Modulation in Silicon Waveguides at 1.5 µm Wavelength". *Applied Physics Letters* **80** (2002), pp. 416–418.

[115] Allan R. Cowan, Georg W. Rieger, and Jeff F. Young. "Nonlinear Transmission of 1.5 Um Pulses through Single-Mode Silicon-on-Insulator Waveguide Structures". *Opt. Express* **12** (2004), pp. 1611–1621.

[116] Jung H. Shin, G. N. van den Hoven, and A. Polman. "Direct Experimental Evidence for Trap-state Mediated Excitation of Er^{3+} in Silicon". *Applied Physics Letters* **67** (1995), pp. 377–379.

[117] Ian R. Berkman et al. *Sub-Megahertz Homogeneous Linewidth for Er in Si via in Situ Single Photon Detection*. 2021.

[118] Christopher M. Dodson and Rashid Zia. "Magnetic Dipole and Electric Quadrupole Transitions in the Trivalent Lanthanide Series: Calculated Emission Rates and Oscillator Strengths". *Phys. Rev. B* **86** (2012), p. 125102.

[119] Sara Marzban et al. "Observation of Photon Echoes from Evanescently Coupled Rare-Earth Ions in a Planar Waveguide". *Phys. Rev. Lett.* **115** (2015), p. 013601.

[120] M. Cho. *Two-Dimensional Optical Spectroscopy*. CRC Press, 2009.

[121] A. Szabo. "Observation of hole burning and cross relaxation effects in ruby". *Phys. Rev. B* **11** (11 1975), pp. 4512–4517.

[122] Silvia Völker. "Hole-Burning Spectroscopy". *Annual Review of Physical Chemistry* **40** (1989), pp. 499–530.

[123] L. Vivien and L. Pavesi. *Handbook of Silicon Photonics*. Series in Optics and Optoelectronics. Taylor & Francis, 2013.

[124] S. R. Hastings-Simon et al. "Zeeman-Level Lifetimes in Er^{3+}:Y_2SiO_5". *Phys. Rev. B* **78** (2008), p. 085410.

[125] Christopher M. Phenicie et al. "Narrow Optical Line Widths in Erbium Implanted in TiO_2". *Nano Lett.* **19** (2019), pp. 8928–8933.

[126] Pedro de Vries and Ad Lagendijk. "Resonant Scattering and Spontaneous Emission in Dielectrics: Microscopic Derivation of Local-Field Effects". *Phys. Rev. Lett.* **81** (1998), pp. 1381–1384.

[127] N. Q. Vinh, N. N. Ha, and T. Gregorkiewicz. "Photonic Properties of Er-Doped Crystalline Silicon". *Proceedings of the IEEE* **97** (2009), pp. 1269–1283.

[128] M. David Henry, Colin Welch, and Axel Scherer. "Techniques of Cryogenic Reactive Ion Etching in Silicon for Fabrication of Sensors". *Journal of Vacuum Science & Technology A* **27** (2009), pp. 1211–1216.

[129] W. Bogaerts et al. "Silicon Microring Resonators". *Laser & Photonics Reviews* **6** (2012), pp. 47–73.

[130] Koji Yamada. "Silicon Photonic Wire Waveguides: Fundamentals and Applications". *Silicon Photonics II: Components and Integration*. Ed. by David J. Lockwood and Lorenzo Pavesi. Berlin, Heidelberg: Springer Berlin Heidelberg, 2011, pp. 1–29.

[131] Qi Zhang et al. "Single Rare-Earth Ions as Atomic-Scale Probes in Ultrascaled Transistors". *Nano Lett.* **19** (2019), pp. 5025–5030.

[132] Gary Wolfowicz et al. "Quantum Guidelines for Solid-State Spin Defects". *Nature Reviews Materials* **6** (2021), pp. 906–925.

[133] Rikuto Fukumori et al. "Subkilohertz Optical Homogeneous Linewidth and Dephasing Mechanisms in Er^{3+}:Y_2O_3 Ceramics". *Phys. Rev. B* **101** (2020), p. 214202.

[134] Tian Xie et al. "Characterization of Er^{3+}:YVO_4 for Microwave to Optical Transduction". *Phys. Rev. B* **104** (2021), p. 054111.

[135] Tian Zhong and Philippe Goldner. "Emerging Rare-Earth Doped Material Platforms for Quantum Nanophotonics". *Nanophotonics* **8** (2019), pp. 2003–2015.

[136] Stephen T. Liddle and Joris van Slageren. "Improving F-Element Single Molecule Magnets". *Chem. Soc. Rev.* **44** (2015), pp. 6655–6669.

[137] O. Madelung, U. Rössler, and M. Schulz, eds. *Silicon (Si), Debye Temperature, Heat Capacity, Density, Hardness, Melting Point: Datasheet from Landolt-Börnstein - Group III Condensed Matter* ˙.

[138] W. Hübner and K. H. Bennemann. "Simple Theory for Spin-Lattice Relaxation in Metallic Rare-Earth Ferromagnets". *Phys. Rev. B* **53** (1996), pp. 3422–3427.

[139] M. B. Schulz and C. D. Jeffries. "Spin-Lattice Relaxation of Rare-Earth Ions in LaF_3". *Phys. Rev.* **149** (1966), pp. 270–288.

[140] Francesco Priolo et al. "Excitation and Nonradiative Deexcitation Processes of Er^{3+} in Crystalline Si". *Phys. Rev. B* **57** (1998), pp. 4443–4455.

[141] H. M. Crosswhite and G. H. Dieke. "Spectrum and Magnetic Properties of Hexagonal $DyCl_3$". *J. Chem. Phys.* **35** (1961), pp. 1535–1548.

[142] Gabriele G. de Boo et al. "High-Resolution Spectroscopy of Individual Erbium Ions in Strong Magnetic Fields". *Phys. Rev. B* **102** (2020), p. 155309.

[143] E. Baldit et al. "Identification of Λ-like Systems in Er^{3+}:Y_2SiO_5 and Observation of Electromagnetically Induced Transparency". *Phys. Rev. B* **81** (2010), p. 144303.

[144] G. Müller and J. Friedrich. "Crystal Growth, Bulk: Methods". *Encyclopedia of Condensed Matter Physics*. Ed. by Franco Bassani, Gerald L. Liedl, and Peter Wyder. Oxford: Elsevier, 2005, pp. 262–274.

[145] A. Polman et al. "Erbium in Crystal Silicon: Optical Activation, Excitation, and Concentration Limits". *Journal of Applied Physics* **77** (1995), pp. 1256–1262.

[146] Mikhail N. Drozdov et al. “Oxygen and Erbium Distribution in Diffusion Doped Silicon”. *Modern Electronic Materials* **2** (2016), pp. 7–12.

[147] Yiming He, Dan Lu, and Lingjuan Zhao. “Reflection Airy Distribution of a Fabry-Perot Resonator and Its Application in Waveguide Loss Measurement”. *Opt. Express* **27** (2019), pp. 17876–17886.

[148] T.F. Ciszek and T.H. Wang. “Silicon Defect and Impurity Studies Using Float-Zone Crystal Growth as a Tool”. *Journal of Crystal Growth* **237–239** (2002), pp. 1685–1691.

[149] Andrzej Gajda et al. “Design Rules for P-i-n Diode Carriers Sweeping in Nano-Rib Waveguides on SOI”. *Opt. Express* **19** (2011), pp. 9915–9922.

[150] W.E. Moerner et al. *Persistent Spectral Hole-Burning: Science and Applications*. Topics in Current Physics. Springer Berlin Heidelberg, 2012.

[151] V.E. Borisenko and P.J. Hesketh. *Rapid Thermal Processing of Semiconductors*. Microdevices. Springer US, 2013.

[152] Jeffrey A. Steidle et al. “High Spectral Purity Silicon Ring Resonator Photon-Pair Source”. Proc.SPIE. Vol. 9500. 2015.

[153] Takashi Asano et al. “Photonic Crystal Nanocavity with a Q Factor Exceeding Eleven Million”. *Opt. Express* **25** (2017), pp. 1769–1777.

[154] Saeed Khan et al. “Low-Loss, High-Bandwidth Fiber-to-Chip Coupling Using Capped Adiabatic Tapered Fibers”. *APL Photonics* **5** (2020), p. 056101.

[155] Je-Hyung Kim et al. “Hybrid Integration Methods for On-Chip Quantum Photonics”. *Optica* **7** (2020), pp. 291–308.

[156] Noel H. Wan et al. “Large-Scale Integration of Artificial Atoms in Hybrid Photonic Circuits”. *Nature* **583** (2020), pp. 226–231.

[157] Wim Bogaerts et al. “Programmable Photonic Circuits”. *Nature* **586** (2020), pp. 207–216.

[158] Pablo Cova Fariña et al. “Coherent Control in the Ground and Optically Excited States of an Ensemble of Erbium Dopants”. *Phys. Rev. Applied* **15** (2021), p. 064028.

[159] Benjamin Merkel, Pablo Cova Fariña, and Andreas Reiserer. “Dynamical Decoupling of Spin Ensembles with Strong Anisotropic Interactions”. *Phys. Rev. Lett.* **127** (2021), p. 030501.

[160] Peter S. Barnett and Jevon J. Longdell. “Theory of Microwave-Optical Conversion Using Rare-Earth-Ion Dopants”. *Phys. Rev. A* **102** (2020), p. 063718.

[161] Sacha Welinski et al. “Electron Spin Coherence in Optically Excited States of Rare-Earth Ions for Microwave to Optical Quantum Transducers”. *Phys. Rev. Lett.* **122** (2019), p. 247401.

[162] Alexandre Blais et al. “Circuit Quantum Electrodynamics”. *Rev. Mod. Phys.* **93** (2021), p. 025005.

[163] C. Chartrand et al. “Highly Enriched ^{28}Si Reveals Remarkable Optical Linewidths and Fine Structure for Well-Known Damage Centers”. *Phys. Rev. B* **98** (2018), p. 195201.

[164] Saeedi Kamyar et al. “Room-Temperature Quantum Bit Storage Exceeding 39 Minutes Using Ionized Donors in Silicon-28”. *Science* **342** (2013), pp. 830–833.

[165] Christoph Simon et al. “Quantum Repeaters with Photon Pair Sources and Multimode Memories”. *Phys. Rev. Lett.* **98** (2007), p. 190503.

[166] J. J. Longdell et al. “Analytic Treatment of Controlled Reversible Inhomogeneous Broadening Quantum Memories for Light Using Two-Level Atoms”. *Phys. Rev. A* **78** (2008), p. 032337.

[167] Mikael Afzelius et al. “Multimode Quantum Memory Based on Atomic Frequency Combs”. *Phys. Rev. A* **79** (2009), p. 052329.

Acknowledgements

During my time at MPQ, I was part of an excellent team with highly motivated students and scientists. Without them, performing the experiments presented in this thesis would not have been possible and I am very grateful for that.
First of all, I would like to thank Andreas Reiserer. He gave me the opportunity to work on my dissertation in his group and entrusted me with starting the silicon project. The discussions with him, his wealth of ideas, and his confidence have contributed significantly to the success of this work.
I would like to thank Gerhard Rempe for hosting the group retreats at Ringberg Castle, for providing an excellent infrastructure and for agreeing to serve as supervisor for this thesis.
My partner in the lab since day one was Andreas Gritsch. His deep understanding of physics, his programming skills, and his nanofabrication experience did speed up the silicon project by a lot. The discussions we had during the countless coffee breaks dramatically improved my understanding of the data and its analysis.
I want to also thank all current and former members of the silicon project for their contributions. In particular, I thank Florian Burger and Johannes Früh for help with the nanofabrication and the etching of countless tapered fibers. Also, I want to thank Stephan Rinner for his efforts on the rib waveguide project. I am looking forward to many exciting results in the upcoming years.
I would like to thank Benjamin Merkel for setting up the measurement electronics and introducing me to the experiment control software. Also, I would like to thank Alexander Ulanowski for his continuous help in the lab and his assistance with various programming issues.
The waveguide experiment would not exist in its current form without the help of the technicians Johannes Siegl, Florian Furchtsam, Tobias Urban, and Thomas Wiesmeier. In particular, I would like to thank Johannes for preparing countless technical drawings and for his help with any major and minor technical issue.
I would like to thank Iris Anneser, the purchasing department, and the travel department for overcoming many issues with bureaucracy.
The nanofabrication would not have been possible without a cleanroom. Therefore, I thank the ZNN, the WSI and the WMI for allowing us to use their facilities. Also, I thank Franz Eberle for helping me out with large amounts of protective resist and AFM measurements in Regensburg.
I want to thank my friends and family for their support. Especially, I thank my parents for generously financing my studies and the encouraging words when the experiment was down once in a while. In particular, I would like to thank my father for his interest in the progress of the work as well as for discussion and support.
Finally, I would like to thank Louise for her understanding, support and encouragement over the last years.